University of Sheffield

Functional-Structural Modelling of the Palisade Mesophyll Air Channel

A thesis submitted to the University of Sheffield for the degree of Doctor of Philosophy

Shiv Jasveer Gangapersad

Department of Automatic Control and Systems Engineering

July 2023

To me, this journey into academia is epitomised by the words of Inugami Korone:

"Have confidence! ...No confidence."

Acknowledgements

I would like to thank my first supervisor, Prof. Visakan Kadirkamanathan, for his unending patience and support, and always finding the right words and sharing wisdom from his own past academic experiences with me. My second supervisor, Prof. Andy Fleming, has been one of the most cheerful people I've had the pleasure to work with, and I appreciate his readiness to provide me with resources I needed, whether it was setting up a meeting with another academic, additional hard drives, or some of his own time to go over my various ponderings of the biological mechanisms of plants. I owe much of the rigour in my modelling work to Dr Bryn Jones, who provided me with valuable supervision during his time here, and taught me to step back and see the bigger picture of my work.

I would like to extend my thanks to Dr Alice Baillie for her incredible patience and for always answering my numerous questions when I was just getting started, and Dr Simon Pope for his encouragement and for the coffee walks we've had over the last year. Further thanks go to my old friend and colleague, David, for being here at all times of day and night for technical support, or just grabbing a cup of coffee.

I need to thank my dear friend Bent, for being my best buddy and always pointing me towards the bright side of things. My friends and fellow ex-PhD students, Drs. Oliver, Zak and Laura, thank you for your support, always being here for rants, proof-reading or midnight sanity checks. Ryan, Naresh and Alex, my long time friends who were always here to help me make light of the situation when things weren't looking so hopeful, or would just join me to lament. James and Louise, who provided me with the comfort of a home and delicious food towards the end of my PhD.

I would also like to thank my family, without who the last four years would have been filled with even more trials and tribulations. Thank you to my cousin Anju for always providing words of reassurance from her own PhD experiences, my parents for their never ending acts and words of support, and lastly, my brother for providing a sense of normalcy during this bizarre adventure.

Abstract

The photosynthetic pathway has been extensively researched at the subcellular level and for the whole leaf, with established biochemical and mechanistic models. While it is known that the balance of intercellular airspace and cellular material depends on patterns of cell division and growth, it is less well understood how different intercellular airspace arrangements impact photosynthesis. What is the relationship between the amount of internal mesophyll surface area exposed to air, photosynthetic capacity and cell size? Is there an optimal airspace-tissue balance, and if so, how will it change under future levels of CO_2?

With recent advances in micro-computer tomography (μ-CT), it is possible to quantify the intercellular mesophyll airspace at a local scale and obtain paired datasets of global gas exchange measurements. In this thesis, we propose a mathematical framework to model air channels in the palisade mesophyll layer as microscopic air channels by applying Fick's first law of diffusion. By validating this mechanistic model with experimental observations of paired μ-CT/gas exchange data in a series of *Arabidopsis thaliana* mutants, we can explore the trade-off between the amount of cellular material and air channels in the palisade layer. More importantly, this structure-function modelling framework allows us to identify which of these structural properties are favoured by mutants with better photosynthetic performance, and quantify whether there is any consistent behaviour leading to an 'optimal' trade-off between cellular material and air channels.

The analysis shows that the intercellular CO_2 uptake rate is a function of the palisade mesophyll air channel depth. This observation implies a trend in which leaves with shorter intercellular diffusion pathways within the palisade mesophyll have a higher CO_2 assimilation rate, which could suggest an optimisation of the inner mesophyll cell structure. Hence, from a physical diffusion-based model supported by data-driven estimation, we are able to predict function from structure.

Contents

List of Figures

List of Tables

Nomenclature

A list of the variables and notation used in this thesis is defined below. The definitions and conventions set here will be observed throughout unless otherwise stated. For a list of acronyms, please consult page xv.

A_{400}	Measured CO_2 assimilation rate at atmospheric CO_2 ($\mu mol\, m^{-2}\, s^{-1}$)
$\boldsymbol{\alpha}$	Deviation factor (unitless)
$\boldsymbol{\eta}$	Correction factor (unitless)
Γ_{H_2O}	Water vapour loss rate ($mol\, s^{-1}$)
$\Gamma^{leaf}_{H_2O}$	Water vapour loss rate per leaf area ($mol\, m^{-2}\, s^{-1}$)
L_z	Air channel depth (m)
$\phi_a(z)$	Concentration of gas a at a depth z ($mol\, m^{-3}$)
ρ	Air channel diameter (m)
U_{CO_2}	CO_2 uptake rate ($mol\, s^{-1}$)
$U^{leaf}_{CO_2}$	CO_2 uptake rate per leaf area ($mol\, m^{-2}\, s^{-1}$)
c_1, c_2	Beer-Lambert law constants (unitless)
d	Cell thickness (m)
D_a	Diffusion coefficient of gas a ($m^2\, s^{-1}$)

G_a	Conductance coefficient of gas a ($m\,s^{-1}$)
g_m	Mesophyll conductance to CO_2 ($\mu mol\,m^{-2}\,s^{-1}\,Pa^{-1}$)
$I(z)$	Absorbed photon irradiance ($mol\,quanta\,m^{-2}\,s^{-1}$)
I_0	Incident irradiance ($mol\,quanta\,m^{-2}\,s^{-1}$)
$J(z)$	Diffusion flux ($mol\,m^{-2}\,s^{-1}$)
K_{leaf}	Leaf hydraulic conductance ($mmol\,m^{-2}\,s^{-1}\,MPa^{-1}$)
L_x	Side length of region of interest (m)
L_{leaf}	Leaf thickness (m)
N	Number of air channels within a specified area
P	Porosity (unitless)
R	Molar gas constant ($8.314\ m^3\,Pa\,K^{-1}\,mol^{-1}$)
T_K	Leaf temperature (K)
$w_1, w_2, \ldots$	Polynomial weights (unitless)
z	depth at a given point z (m)

Acronyms

μ-CT micro-Computed Tomography. iii, vii, 3, 9, 13, 17–22, 24, 25, 29, 32, 39

GA Genetic Algorithms. 71

IRGA Infra-Red Gas Analyser. 25, 26

L-O-O Leave-One-Out. 59

ppm parts per million. vi, 4, 26, 40

ROI Region of Interest. 22

Chapter 1

Introduction

1.1 Motivation

Photosynthesis in plants requires CO_2 to flow first from the atmosphere through microscopic pores on the leaf surface (known as the stomata) into the sub-stomatal cavities. From here the CO_2 diffuses through a series of intricate air channels formed by the separation of mesophyll cells within the leaf. These mesophyll cells are themselves the site of the chloroplasts (the main photosynthetic apparatus of the leaf) which contain the enzymatic machinery required for the fixation of CO_2 into sugar, the product of photosynthesis, which supports life on the planet. The diffusion pathway within the leaf from the sub-stomatal space to the enzymes in the chloroplasts at the heart of photosynthesis represents a series of resistances to the flux of CO_2 and, thus, a limitation to the rate of CO_2 fixation [112]. This pathway is shown in Figure 1.1.

This is particularly relevant when considering the efficiency of photosynthesis as a process, and whether it can be increased. The inability of the primary enzyme involved in CO_2 fixation, RuBisCO, to discriminate between CO_2 and oxygen (leading to energy-wasting process called photorespiration, where RuBisCO enters a catalytic reaction involving oxygen instead, releasing previously fixed CO_2) results in overall photosynthetic efficiencies of less than two thirds of what theoretically could be achieved in many plant species. Even moderate increases in the flux of

CO_2 within leaves to the site of carboxylation could potentially lead to significant gains in photosynthetic yield at essentially no extra cost.

Despite the inherent inefficiency of the photosynthetic process, the biological matrix of cells that forms the leaf has adapted to maximise photosynthetic yield. This intricate packing of cells gives rise to an interwoven arrangement of intercellular air channels that are optimised for resource management by simultaneously increasing gas exchange efficiency and water use efficiency [169]. Despite the arrangement of intercellular mesophyll air channels being well documented [42, 78, 87, 101, 136, 137], the biological basis behind this formation, or rather, the molecular mechanisms that control air space formation are less well understood, and as such, air space formation and patterning is generally accepted as an emergent property of cell growth, division, adhesion and death within the leaf [78, 87, 169]. The morphogenesis of intercellular air spaces in relation to leaf morphogenesis is very much an active field of research. For instance, through extensive research of the cell cycle, knowledge of genetic behaviour modulating cell division or patterning is now known [28, 33, 156, 157]. On the other hand, mechanisms behind the partial separation of cells after cell division (hence leading to the formation of air spaces) still remain to be elucidated [87].

As a result, the bulk of research aimed at photosynthetic improvement has focused on altering plant biochemistry, and this has led to recent significant success [19, 46, 59, 73, 80, 165]. Although altering structural aspects of the leaf inner structure have been identified as potential goals, progress has been slower in achieving targeted improvements. This partly reflects the complexity of the processes by which leaf structure is formed, and the various trade-offs inherent in how structure impacts not only photosynthesis but many other aspects of plant function [55, 148]. Progress may also have been slower due to a reliance on essentially a correlative modelling approach followed by mechanistic interpretation [61]. An alternative approach is to consider the system from first principles and to build an initially simplistic mechanistic model that represent the system. If the outputs of such a model realistically captures measured elements of system performance, then it can be used to both validate the initial basic assumptions underpinning the model , and provide indicators of whether the system can be improved or how it may work under different conditions.

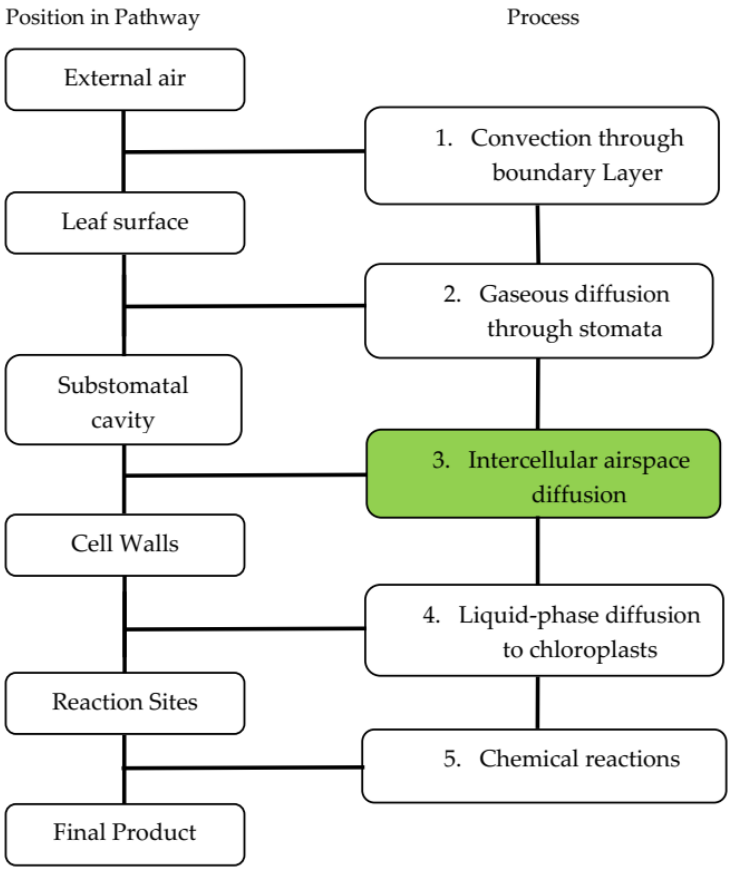

Figure 1.1: CO_2 assimilation pathway, adapted from Parkhurst [112]. The focus of this work is on modelling the highlighted block.

We have taken such an approach and report on the generation and validation of a model for CO_2 diffusion through leaf air channels. The model is first parameterised using available data for wild-type *Arabidopsis thaliana*, then extended to include a number of genetic mutants which vary in leaf air channel network structure. Importantly, these mutants have all been analysed using x-ray micro computed tomography μ-CT, which provides quantitative measurements of air channel dimensions in 3D, in contrast to many previous investigations which lack or indirectly estimate these critical parameters.

Our model captures the range of air channel diameter observed to be within the range of theoretically optimal for observed rates of carbon assimilation. In addition, an analysis of mutants with a range of air channel networks suggests that shorter

air channels are more efficient with respect to CO_2 uptake and assimilation. These results are set in the context of the observed biological response to environmental influences (for instance, atmospheric CO_2 levels, Figure 1.2) and leaf form and, thus, air channel diameter and depth.

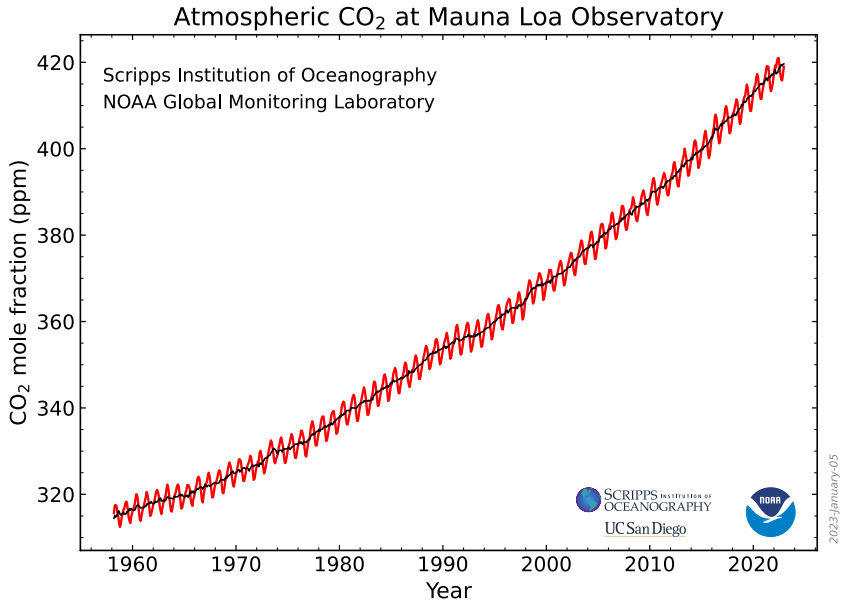

Figure 1.2: Global monthly mean levels of atmospheric CO_2. In this work, we will be working with 400 ppm. Image provided by NOAA Global Monitoring Laboratory, Boulder, Colorado, USA (https://esrl.noaa.gov/).

1.2 Relevant models

Arabidopsis thaliana is a model organism which was the first plant to have its relatively simple genome sequenced [60]. With its fast growth and good response to genetic manipulation [104], Arabidopsis has become a popular model in plant biology. As such, most papers covered in this chapter, and our own study in later sections, will be using Arabidopsis as a model. While this project isn't focused on the biochemical aspects of photosynthesis, we deem it important to give a primer on basic biological premise of this phenomenon. Although there are different types of photosynthesis, we will be focusing on C3 photosynthesis.

In order to reach the chloroplasts inside of the mesophyll cells where photosynthetic reactions can occur, CO_2 has to diffuse through a pathway. As summarised by Figure 1.1, CO_2 diffuses from the outer atmosphere, through the boundary layer (a thin layer of non-turbulent air on the leaf surface), into the stomata located in the epidermis (the top and bottom layers of the leaf), which let the gas into the plant. The gas then proceeds to diffuse through the intercellular mesophyll air spaces, or air channels as we will mostly refer to them as, where it enters the cells through their wet walls, dissolving in the water content of the cells as it does so. Once inside the cells, the CO_2, now in a liquid phase, find their way to the chloroplasts where they will be assimilated [7]. This assimilation process occurs through a set of biochemical catalytic reactions focused on a photosynthetic enzyme, RuBisCO. This process, known as the Calvin Benson cycle, converts carbon into sugars which are then consumed by the plant [6, 119].

The Calvin Benson cycle occurs through what can be broken down into three stages of catalytic reactions through soluble enzymes. In the first stage, carboxylation, CO_2 gets combined with water and a carbon compound, ribulose 1,5-biphosphate (RuBP), to ultimately form 3-carbon molecules (hence why this is known as C_3 photosynthesis. The next stage is known as reduction due to the fact that the 3-carbon molecules are reduced to 3-carbon sugars. Some of these are used to produce glucose, while the rest are recycled to regenerate the RuBP compound used in the first stage, hence why the final stage is aptly named regeneration [96]. While we will not be focusing on the intricate biochemical processes of the Calvin Cycle and C3 photosynthesis in this thesis, this short description should give us an overview of the inner mechanisms of the leaf. In particular, the first 2 stages described here, where photosynthesis is limited by (1), RuBisCO and (2), RuBP regeneration, will be referred to when calculating some photosynthetic traits of interest in Chapter 2. Another important process that occurs in C3 photosynthesis that should be mentioned is photorespiration, which was described earlier in this chapter, and is also one of the key markers of C3 photosynthesis limitations. It is to be noted that photosynthesis as a whole is obviously much more complex than this, but there is no need for us to go into deeper biological detail within the scope of this project, and hopefully this primer will suffice in appreciating the complexity of photosynthesis.

The most seminal model in C3 photosynthesis research, to this date, is the

Farquhar-von Caemmerer-Berry model (FvCB). Farquhar et al. [52] presented a model of the biochemical processes in the chloroplast with respect to the photosynthetic CO_2 uptake of leaves. The model described the rate of CO_2 assimilation [μmol m^{-2} s^{-1}] as the difference between the rate of carboxylation of RuBP via RuBisCO V_c, and loss through photorespiration (through the oxygenation rate V_o) day respiration R_d (describing the release of CO_2 in the light by processes other than photorespiration):

$$A = V_c - 0.5V_0 - R_d = V_c\left(1 - \frac{\Gamma^*}{C_i}\right) - R_d. \tag{1.1}$$

Here C_i is equal to the intercellular CO_2 concentration [μmol mol^{-1}]*, and Γ^* is given as the photosynthetic compensation point (the CO_2 concentration at which CO_2 release via photorespiration equals the rate of photosynthetic uptake, i.e., $V_c = 2V_o$). The term $1 - \frac{\Gamma^*}{C_i}$ therefore corrects for the amount of assimilated CO_2 that is released in photorespiration [92].

While the FvCB model was not a complete model of every possible photosynthetic mechanism, it represented and simplified the major mechanisms into a single framework, and has been of paramount importance in bridging the knowledge gap between leaf biochemistry and gas exchange [53]. The FvCB model has, throughout the years, served as a useful tool to investigate various aspects of leaf physiology, and received several extensions and parameterisations. For instance, when coupled with models of stomatal behaviour, the coordination of hydraulic traits and CO_2 exchange was highlighted (i.e., how the leaf balances water and CO_2) [31]. Extensions of the FvCB model have seen applications in exploring and quantifying constraints and limits to photosynthetic capacity, for example, biochemical and stomatal limitations were quantified by Deans et al. [29, 30]. In another study, a derivative of the FvCB model was designed to evaluate the sensitivity of CO_2 assimilation to changes in CO_2 and O_2 concentrations in the chloroplasts [18].

Perhaps in an application more relevant to this thesis, the FvCB model was also parameterised by Long and Bernacchi [92] to analyse gas exchange measurements in the form of response curves of CO_2 assimilation to intercellular CO_2 concentra-

*In our own research, we use the SI unit mol m^{-3} for C_i instead.

tions, to quantify photosynthetic traits. This work, heavily supported by various derivatives or parameterisations of the FvCB model [9, 10, 66, 67, 93], provided a general form of the model to include three forms of biochemical limitations:

$$A = \min(w_c, w_j, w_p)\left(1 - \frac{\Gamma^*}{C_i}\right) - R_d, \tag{1.2}$$

where w_c, w_j, w_p are carboxylation rates limited by RuBisCO, RuBP-regeneration and TPU (Triose Phosphate Use) respectively, with other terms having been defined earlier. TPU is a special case where the leaf's photosynthetic apparatus struggles to export the products of the Calvin Benson cycle, leading to a limit or even decline in the photosynthetic yield [180] - we will not be dwelling on this limit here. By using the respective expressions from equation (1.2) for CO_2 assimilation under RuBisCO limitation, and under RuBP-regeneration limitation, we can quantify a key photosynthetic trait that will be of interest to us later us: mesophyll conductance to CO_2, g_m. Mesophyll conductance is a key descriptor of photosynthetic performance, and can be described as the *transfer conductance* of CO_2 from the intercellular air channels of the leaf, through the cell walls and into the chloroplasts [9], where the CO_2 is assimilated. From Long and Bernacchi [92] and the aforementioned works supporting it, an expression for the concentration of CO_2 at the sites of photosynthesis is known:

$$C_c = C_i - A/g_{m,CO_2}. \tag{1.3}$$

This equation can be substituted in the specific forms of equation (1.2) for RuBisCO and RuBP-regeneration to estimate a value for the mesophyll conductance to CO_2. In Chapter 2, we will be using a popular solver to estimate g_m for a range of *Arabidopsis thaliana* mutants using by gas exchange measurements.

Despite its apparent simplicity, the FvCB model has proved to be a very powerful tool in exploring and quantifying major photosynthetic mechanisms and their limitations, whether biochemical or environmental in nature. Perhaps one of its disadvantages is that it remains a pure biochemical model and generally outputs a 'leaf-level' description of photosynthesis. It does not contain any parameters directly related to leaf mesophyll structure, and therefore does not describe the relationship photosynthetic performance and said structure. As such, it has seen applications where it was combined with structural or dimensional models of the

leaf, either built from physical principles or geometric assumptions, in order to explore photosynthesis at a localised level.

One such interesting application would be the three-dimensional model of CO_2 transport in air spaces and mesophyll cells of a silver birch leaf by Aalto and Juurola [2]. In one of their previous works [1], Aalto & Juurola presented a parameterisation of the FvCB model, which was fitted to response curves of CO_2 concentration and irradiance, corresponding to a set of different temperatures, all for silver birch leaves. This allowed them to explore the temperature dependence of photosynthetic performance. This was scaled up to a numerical 3D model (shown in Fig. 1.3) to study the CO_2 transport through a birch leaf, assumed from observations made from 2D light microscopy observations. The diffusion of CO_2 inside and

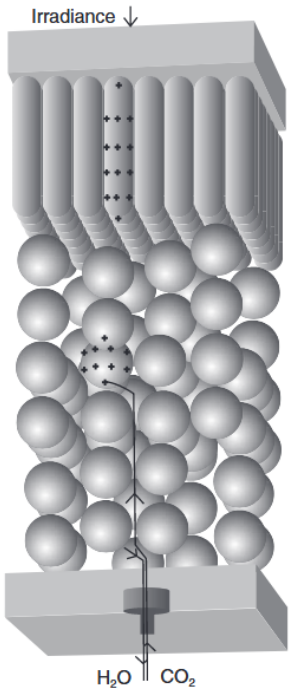

Figure 1.3: The assumed model geometry, reproduced from Aalto and Juurola [2]. Spheres and cylinders represent the spongy and palisade mesophyll cells respectively, with the opening at the bottom representing a stomatal opening. Darker dots as '+' symbols represent the chloroplasts.

outside of the cells was described by $D\nabla^2 c = S$, where D was the binary diffusion coefficient in either the airspace or the cell, c was the concentration of CO_2 in either the airspace or the cell, and S was a source or sink of CO_2 and was set

to zero unless at a chloroplast. The irradiance through the leaf was described by the attenuation of light through the leaf depth using the Beer-Lambert law. By applying their re-parameterised model derived from the original FvCB model, they were able to study CO_2 transport inside the birch leaf model. The model was also subject to a number of variations, such as reduction of stomatal openings, changes in temperature, or doubled ambient CO_2 concentration. The latter was found to introduce severe non-linear effects in the total gas transport output. They observed that conductances in both the gas and liquid phases (i.e., outside and inside the cells) were highly sensitive to changes in temperature and degree stomatal opening, and concluded that the palisade and spongy layers contributed unequally to overall photosynthetic performance.

One of the more modern applications of the the FvCB model can be found in the work done by Xiao et al. [176]. They designed a tool using Bayesian statistics with gas exchange and chlorophyll fluorescence (i.e., light response curves of photosynthesis) to fit photosynthetic parameters, while evaluating the reliability of the estimation, and providing a measure of the estimation accuracy. This tool can serve as a means to reduce human error and subjectivity usually involved in fitting response curves to the FvCB model, limiting the error source to variability in physiology. They also observed that providing measurements of photosynthetic responses to low CO_2 and low light improved the estimations, proposing that this as a standard for measurement protocols.

More recently, we have seen several advances in imaging methods, such as μ-CT(micro-Computer Tomography, which we will cover in more detail in the next chapter) [101, 110, 155] allowing to better visualise and quantify the inner structure of the leaf in finer detail. Pairing this knowledge of the leaf's interior with gas exchange measurements has allowed us to ascertain the link between mesophyll structure and photosynthetic performance [87], i.e., between leaf structure and function. The next few models embrace this concept of linking structure and function in various ways.

Ho et al. [68] developed a three-dimensional microscale model of a tomato leaf by assuming a 3D geometry observed from results of an x-ray laminography [155]. The x-ray results did not provide them with knowledge of the cell composition, and as such, they decided to not model organelles such as the mitochondria

explicitly, assuming uniform distribution. They did however, allow for the chloroplast concentration to be varied in their model. Ho et al. then computed the light absorption within their assumed model structure used a meshed Monte-Carlo photon transport solver (an efficient numerical method to numerically solve for light absorption) [166]. The resulting light absorption was then used as an input to the generalised FvCB model [92] we discussed earlier, over different stages of limitations of photosynthesis. They also described the microscale diffusion of CO_2 and carbonic anhydrase, HCO_3^-, an enzyme facilitating the CO_2 uptake, using a set of diffusion-reaction equations:

$$\begin{aligned} &\nabla.(D_{CO_2}\nabla[CO_2]) - w^* + R_d^* + R_p^* - B = 0, \\ &\nabla.(D_{HCO_3}\nabla[HCO_3^-]) + B = 0. \end{aligned} \tag{1.4}$$

We have already seen what R_d^*, R_p^*, w^* are from the FvCB model. ∇ is the gradient operator and D is the diffusivity for CO_2 and HCO_3^-. B is the net hydration CO_2 to HCO_3^-, where HCO_3^- catalyses the hydration of CO_2 into the cell. The combination of a reaction-diffusion model, a 3D mesophyll structure, ans a numerically solved light environment, coupled with the FvCB model, allowed them to obtain a realistic evaluation of leaf photosynthetic CO_2 uptake under a range of different CO_2 and light conditions. The assumed model structure allowed for the chloroplast concentration to also be varied, but did not allow for the individual evaluation of how other anatomical traits impact photosynthetic performance, as the geometry was kept fixed. A example of their assumed model structure, with numerically computed concentrations of chloroplasts, and assumed location and distribution of other organelles is shown in Fig. 1.4.

They observed that carbonic anhydrase, HCO_3^-, while having little impact on photosynthetic efficiency at high CO_2 levels, had a beneficial impact on the efficiency at low CO_2 concentrations. By adjusting the chloroplast location within the geometry to maximise their surface area exposed to the intercellular air spaces, the proportion of photo-respired CO_2 re-fixed by RuBisCO was also improved. Importantly, they also added that scaling photosynthetic capacity led to an improvement of CO_2 fixation within the cells, especially at lower light levels.

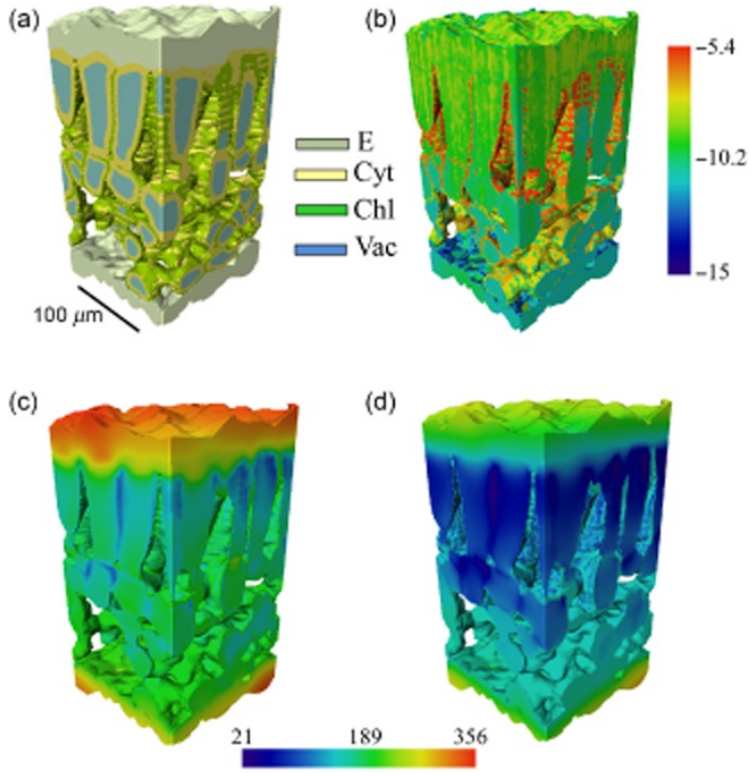

Figure 1.4: Microscale geometry and CO_2 distribution in a tomato leaf, reproduced from Ho et al. [68]. (a) Reconstructed geometry based on synchrotron x-ray laminography, with E being the epidermis, Cyt being the cytosol, Chl the chloroplasts, and Vac the vacuoles, (b) showing the light absorbance of the leaf tissue, (c) showing the distribution of CO_2 at 21% O_2, (d) showing the CO_2 concentration at 2% O_2.

Another recent study by Xiao et al. [177] offers one of the most comprehensive models combining leaf anatomy and photosynthetic performance to date. They present a complex mechanistic model, termed the *eLeaf*, modelled around the anatomy and photosynthetic performance of a rice leaf. The model successfully captures the photosynthetic behaviour of a rice life at a range of varying environmental conditions, such as CO_2 concentration and incident light. The design of the model was done in the form of four distinct, but connected 'modules', which all integrated measurements of the rice leaf anatomy and physiology. The first module was an automatic reconstruction of leaf anatomy into an assumed 3D leaf geometry from a range of different measurements obtained from different microscopy and computer tomography techniques (as highlighted in Fig. 1.5).

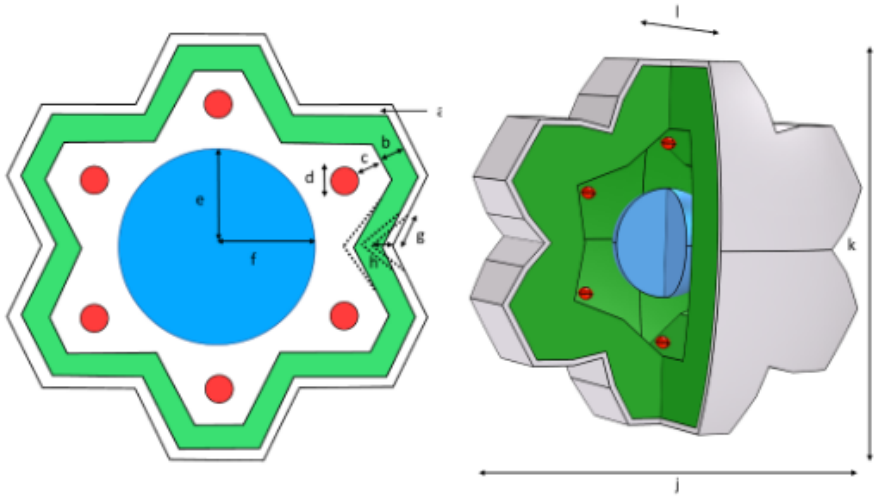

Figure 1.5: 3D leaf geometry module of *eLeaf*, reproduced from Xiao et al. [177], showing the reconstruction of a single mesophyll cell in a rice leaf. Parameters a-f control various structural properties of organelles (cytosol, chloroplast, etc.), g-h control the contact area of the mesophyll cell surface to the intercellular air space, j,k,l control the length, width, thickness of the mesophyll cell. All of these are reconstructed and fitted from structural measurements.

The second module is a 'light' module, making use of a ray-tracing algorithm from Xiao et al. [175] (a computational method that numerically solves for realistic light transport or absorption) to simulate for heterogeneous light environments in rice leaf, as the cells are not neatly arranged uniformly. The third module is a CO_2 module that employs reaction-diffusion equations to predict the CO_2 diffusion from the air spaces all the way into the chloroplasts. The last module focuses on metabolism by using the FvCB model to quantify photosynthetic traits.

The combination of these four modules, when fully parameterised with anatomical and physiological measurements from rice leaves, successfully allowed the model to capture expected rice photosynthetic performance at leaf-level. The model could also be interrogated with a range of different conditions. One of the outcomes, for instance, was that the main driver behind increased CO_2 assimilation under elevated CO_2 concentration, was the metabolism module, with structural parameters making minor contributions. One surprising observation was that the mesophyll porosity (ratio between air space and cellular tissue inside the leaf) could be varied without a drastic change in photosynthetic performance. This highlighted a possi-

ble degree of leaf structural plasticity (i.e., the leaf supporting a range of possible structural changes) with respect to photosynthetic capacity.

In a departure from modelling strategies hinged on the FvCB model, let us briefly mention another recent study from Théroux-Rancourt et al. [150], focusing on making light of the relationship between the leaf mesophyll structure and the rates of CO_2 diffusion. Théroux-Rancourt et al. quantified the inner leaf structure of a large range of C3 species through μ-CT scanning, obtaining structural parameters such as mesophyll porosity, cell size, intercellular surface area exposed to air, amongst others. While no gas exchange measurements were paired with the structural descriptors, Théroux-Rancourt et al. simulated the overall conductance to CO_2 (both in the gaseous and liquid phases) for a range of possible mesophyll structures. With the power of statistical analysis, they concluded that smaller cells, and hence denser cell packing and increased intercellular surface area exposed to air, were linked to maximising CO_2 diffusion in the inner leaf structure. They also concluded that the palisade layer better facilitated CO_2 diffusion in the liquid phase, while the spongy layer did the inverse, by better accommodating for gaseous diffusion.

As established by Lehmeier et al. [87], Mathers et al. [101], Théroux-Rancourt et al. [150], Verboven et al. [155], modern imaging methods allow for the extraction and quantification of the intercellular air channels inside of the leaf mesophyll, which reveals an intricate network of channels showing various levels of interconnected-ness, depending on their position within the leaf (i.e., palisade and spongy). While not directly related to the work in this thesis, we can close off this chapter by appreciating how network or transport modelling could in the future be applied on this network of air channels to assess how different networked structures affect CO_2 uptake and assimilation within the inner leaf mesophyll.

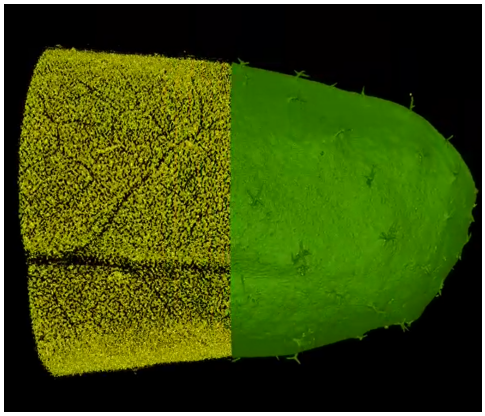

Figure 1.6: 3D rendering of the extraction of the air space network from *Arabidopsis thaliana* (Fleming Lab, University of Sheffield).

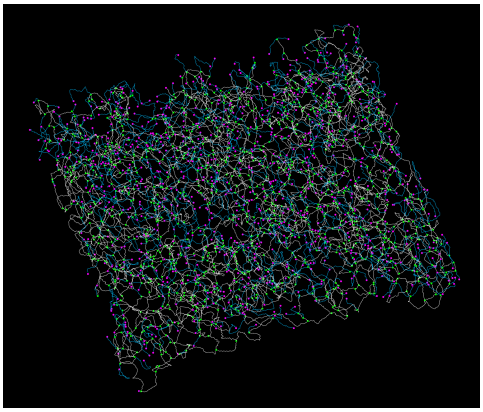

Figure 1.7: Skeleton of the air channel network of *Arabidopsis thaliana*, generated from BoneJ [36].

One of the possible avenues for modelling the complex air channel network found in leaves could be adapted from work done by Zheng et al. [183]. They established that plants and animals, for instance, possess tissues that contain hierarchical networks of pores, with the pore size ratios being adapted to optimise rates of transport and reaction. This type of multi-scale networked system can be described by a generalised version of Murray's law. Murray's law states that if a parent channel of radius r_0 splits into n channels of radii r_i for laminar flow or mass transfer, then the flow rate in channel r_0 is:

$$\begin{aligned} Q_0 &= \sum_{i=1}^{n} Q_i, \\ r_0^{\alpha} &= \sum_{i=1}^{n} r_i^{\alpha}. \end{aligned} \tag{1.5}$$

where Q is the laminar flow rate (given by the Hagen-Poiseuille equation), $\alpha = 2$ for mass diffusion, $\alpha = 3$ for laminar flow transfer. The generalised version accounts for mass variation by introducing a mass loss ratio X during transfer in the parent channel, which allows us to obtain the optimal radius (or diameter) ratios for maximum transport:

$$r_0^{\alpha} = \frac{1}{1-X} \sum_{i=1}^{n} r_i^{\alpha}. \tag{1.6}$$

The generalised Murray's law can be parameterised using quantified parameters of air channels, such as their levels of connectivity, and assess whether plants have adapted their air channel network to maximise CO_2 uptake, or perhaps, to minimise water loss.

We can conclude that there are no models that explicitly describe the function of single channels in terms of gas exchange (including environmental factors) and show their behaviour as a connected structure. We surmise that this type of model would allow us to deduce what an optimal channel network should look like, and find the best structural values to enhance biological performance(i.e., CO_2 assimilation).

1.3 Thesis layout

The main aim of this thesis is to explore the link between intercellular CO_2 gas exchange within the palisade mesophyll and the structure of the palisade mesophyll (i.e., the air channel arrangement within the palisade) by combining physical principles of gas diffusion and state-of-the-art paired measurements of structure and photosynthetic performance. If such a relationship can be pinned down, we aim to quantify how the palisade mesophyll structure constrains photosynthetic performance, and conversely, explore what possible arrangements of air channel structure optimise photosynthesis. Using a range of mutants of *Arabidopsis thaliana*, we can also investigate whether plants have already arranged their structure so as to optimise CO_2 uptake, and hence enhance their photosynthetic output.

This rest of this thesis is structured to investigate this proposal, as follows:

- Chapter 2 covers the data collection and analysis methods use to quantify paired datasets of local structural measurements of the inner leaf structure, and global gas exchange parameters.
- Chapter 3 presents a diffusion-driven framework for the CO_2 uptake rate within the palisade mesophyll layer, derived from Fick's laws of diffusion and arranged in a way to explore the effects on CO_2 uptake when certain structural parameters are constrained or varied.

- Chapter 4 expands on the CO_2 uptake rate framework, providing a cross-validated parameterisation of the model using the paired structural/photosynthetic datasets, leading to a prediction of leaf function from structure. The chapter also challenges some of the assumptions taken when deriving the model and explores the validity of some of the assumptions.
- Chapter 5 describes a conceptual framework for H_2O loss from palisade cells into the palisade air channels, and is is compared to the CO_2 uptake model, resulting in an interesting representation of the leaf's dilemma.
- Chapter 6 provides a summary of the research work and contributions of this thesis, following up with some avenues for future work.

Much of the work in chapters 2, 3 and 4 were disseminated at the following conferences and symposiums:

- 9^{th} International Conference on Functional-Structural Plant Models 2020
  Predicting function from structure – An analysis of the palisade mesophyll (oral presentation)
- Plant, Cell & Environment 40^{th} Anniversary Symposium 2019
  Towards a framework for the structure-function analysis of the palisade mesophyll (poster presentation)
- ACSE PGR Symposium 2019 (University of Sheffield)
  Spatial Modelling & Optimisation of Air Channel Network Function (poster presentation)

Chapter 2

Plant Leaf Data Analysis

2.1 Introduction

This section covers the collection of structural and gas exchange data, and mainly focuses on the analysis of the collected data to extract meaningful structural parameters and photosynthetic traits that are then paired to link leaf intercellular structure to photosynthetic performance. We analysed data from a range of Arabidopsis mutants that reportedly differ from wild type *Arabidopsis thaliana*, Col-0, in their palisade mesophyll structure. These datasets were via published literature in this investigation to provide experimental data to test and validate our model, and the anatomical differences, both structural and photosynthetic, are explored.

Section 2.2 focuses on the collection of structural leaf data through μ-CT. All the samples used in this thesis were obtained pre-scanned, but it is important to highlight the collection process, especially the advantages of μ-CT and the novelty of it within plant science.

Section 2.3 outlines the image analysis workflow applied on collected μ-CT datasets to extract simple but key structural parameters describing intercellular air channels. Here, some samples were obtained pre-analysed, while some were analysed by the author of this thesis. More detail about this is covered in the last section of this chapter.

Section 2.4 covers the collection and analysis of gas exchange data. All samples were obtained pre-collected, but the analysis to extract key photosynthetic traits was performed by the author of this thesis. To finish, section 2.5 brings everything together into an analysis workflow, and allows us to describe and characterise all chosen mutants.

Note that plant growth methods are not listed here as all samples were obtained pre-collected from a range of sources from literature, and growth techniques used may differ slightly. The data sources are specified in section 2.5, and the chosen mutants are characterised in detail.

2.2 μ-CT Data Collection

Knowledge of the internal architecture of the leaf is important to better understand the relationship between structure and photosynthetic performance [139]. However, investigating the microstructure of the leaf mesophyll has historically proved challenging, largely due to the leaf's sensitivity to dessication, fragility, low density and fine structure [101].

A number of stereological techniques (using 2D measurements to infer 3D properties) have been applied in past research to quantify structural leaf parameters (for e.g., the exposed intercellular surface area to air) , such as using 2D tissue cross-sections that are fixed chemically and/or stained to increase contrast [76]. Such techniques, however, are accompanied by a myriad of issues, namely being destructive to the sample, being labour intensive, and having a high degree of inaccuracy if the sample itself was poor prepared, with recorded errors of up to 30% for parameters such as the intercellular surface area [149].

Efforts to improve techniques for investigating the microstructure of biological samples at a high level of detail while minimising sample damage or destruction have lead to the development of μ-CT [41]. μ-CT is a non-destructive technique that uses x-rays to characterise samples in three dimensions [139]. More specifically, μ-CT uses a source of ionising radiation (an x-ray) and an x-ray detector, with the sample in between, and emits a focused beam of x-ray that pass through

the sample. The x-ray interacts differently depending on the material, that is it gets attenuated in various degrees described by the equation:

$$I_x = I_0 e^{-\mu x}, \tag{2.1}$$

where I_x is the intensity of the beam at distance x from the source, I_0 is the intensity of the incident beam, and μ is the attenuation coefficient [12, 144]. This is illustrated in a figure adapted from Boerckel et al. [12]:

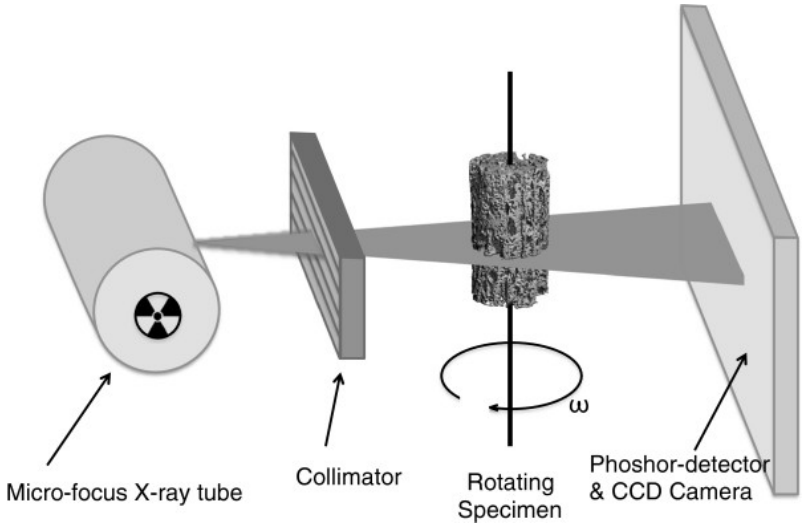

Figure 2.1: Principal components of μ-CT scanning: A micro-focus x-ray tube acting as the source, the collimator focusing the x-ray, which passed through the sample, where the attenuated x-rays are detected by the detector. Image reproduced from Boerckel et al. [12].

As the sample is moved or rotated, the detector collects the attenuated x-ray signals, which are reconstructed to form a 3D representation of the sample. μ-CT allows for the non-invasive investigation of the internal structure of the leaf, without the need for sample fixing or additional staining for contrast Pajor et al. [110]. One of its strengths is that the development and modern use of μ-CT is intimately linked to modern image analysis frameworks, which we will cover later in this chapter. μ-CT is quickly becoming the standard in quantifying and elucidating structure-function relationships in biological sciences, and has been increasingly used in plant science research [34, 35, 87, 95, 97, 130, 154].

All the datasets used in this thesis, albeit from different sources, were all scanned at the Hounsfield Facility (University of Nottingham), and all followed the scanning protocol described by Mathers et al. [101], Pajor et al. [110]. To summarise the process, for each sample, a 5 mm leaf disc was cut out from the middle (lengthways) of the leaf, to either side of the mid-vein. The scans were performed with a Nanotom X-ray CT scanner (GE Sensing and Inspection Technologies GmbH, Wunstorf, Germany). The leaf disc scans were obtained at a spatial resolution of 2.75 μm, with an energy of 65 kV and 140 µA, with an exposure time of 750 ms with a total scan time of 30 minutes per disc.

The radiographs were converted to 3D volumes by using a filtered back projection algorithm. They were converted into aligned TIFF stacks (an image format used by the image processing software) along the z-axis using VG StudioMAX (version 2.2.0; Volume Graphics GmbH, Heidelberg, Germany).

A masking process was necessary, as some 2D slices, especially those at the top and bottom of the leaf, contained background airspace that was not part of the leaf's internal structure - the masks ensure that these are removed. Masks were prepared semi-automatically in Avizo Fire software (version 6.0.0 Fire; Thermo Fisher Scientific, USA) using the `Label Field` function, followed by a binarisation process using `I_threshold`.

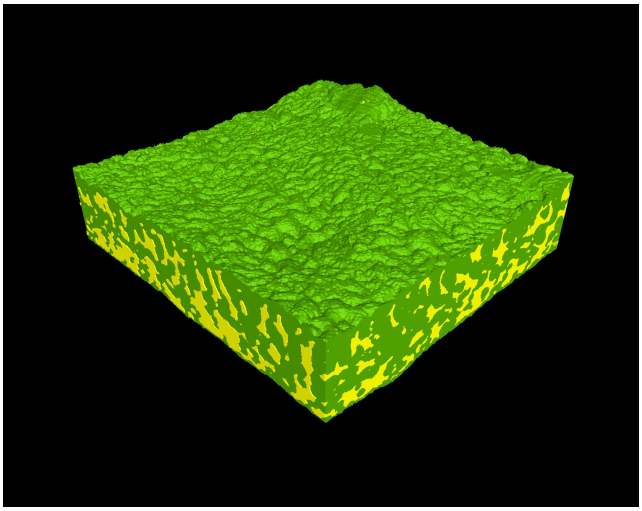

Figure 2.2: 3D rendering of a μ-CT scan of a leaf selection of *Arabidopsis thaliana* (Col-0), highlighting the leaf tissue (green) and air channels (yellow). This figure was obtained from the Hounsfield Facility, University of Nottingham.

2.3 μ-CT Data Analysis

The rest of the workflow is primarily done through the FIJI distribution of ImageJ [129], and is largely adapted from the methodology of Mathers et al. [101]. It should be specified here, that for some mutant lines analysed in this thesis, the steps starting here until the particle analysis step were pre-done, but still verified by the thesis author. For the mutant lines ATML1$_{pro}$: KRP1 and *re6*, the image analysis workflow was entirely performed by the thesis author. The structural characterisation past the particle analysis step was performed by the thesis author for all mutant lines. A visual example of the entire workflow from Mathers et al. [101] is shown below, before we describe the individual steps for our data analysis workflow.

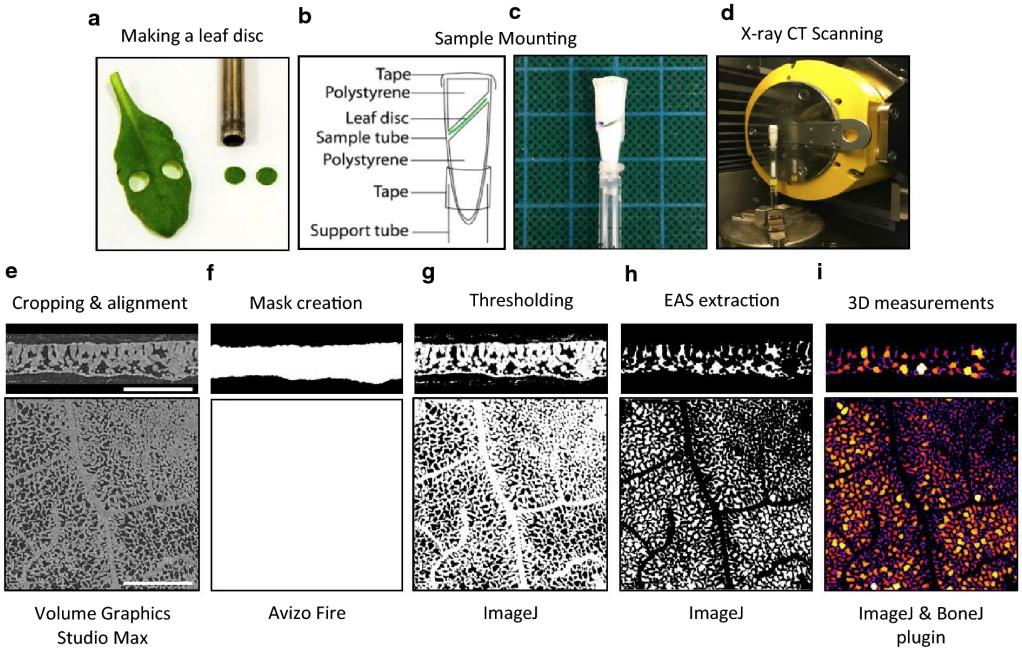

Figure 2.3: Step-by-step stages of the μ-CT workflow, taken from Mathers et al. [101].

To begin, using FIJI, the aligned mask TIFF stacks were automatically thresholded using the `MaxEntropy` algorithm, with the colour range set to `B&W`. Similarly, the aligned image TIFF stacks were also automatically thresholded using the `IsoData` algorithm, with the same colour range as masks, as previously performed in Lehmeier et al. [87], Lundgren et al. [95], Mathers et al. [101].

Before continuing any further, we had to ensure that the global scale was set to 0.00275 mm (which is equal to the pixel resolution), with an aspect ratio of 1 and units set to mm. The air channels were then extracted using the `Image Calculator` in FIJI, by adding (`XOR` process) the binarised and thresholded mask and image TIFF stacks. This resulted in a stack that only contains the air channels. This process was repeated for all stacks, and these stacks were denoised through the selective median filter `Remove Outliers`, which removed both foreground and background particles of size 3 times or less of the spatial resolution.

A Region of Interest (ROI) was then selected from the air channel space stacks by using the `Specify` option under the `Edit>Selection` menu. A ROI of 400×400 voxels was selected for each stack, avoiding major venation, which can artificially increase structural measurements such as porosity. The coordinates of the ROI were noted so that the process can be repeated on the mask stacks. The ROI was extracted by using the `Duplicate` function, with the `Duplicate Stack` option ticked.

With the 3D stacks now thresholded/binarised, and after having selected a region of interest, we then used FIJI built-in particle analysis tool (which uses edge detection algorithms) to detect and quantify every air channel per slice, for every slice, returning individual measurements of perimeter, area, position in stack, amongst other descriptors. A summarised file containing the average information per slice was also generated. This process was also repeated on all the associated mask stacks.

We were interested in obtaining structural descriptors of the air channels specifically, and from the measured perimeters, an equivalent air channel diameter could be calculated using the circle equation:

$$\text{Air channel diameter, } \rho = \frac{\text{perimeter}}{\pi}. \tag{2.2}$$

We were also interested in measuring the air channel depth. Leaves of *Arabidopsis thaliana* are dicotyledonous, and have 2 distinct layers within the mesophyll, namely the palisade and spongy layer. Here, we were interested solely in the palisade mesophyll, but that first entailed identifying where the palisade mesophyll layer started and ended within the leaf.

The rationale behind only considering the palisade layer was because it is generally accepted to be the main part of a dicot leaf that drives photosynthesis, where the major portion of incident light (i.e., photosynthetic active radiation, PAR) was absorbed, with the spongy layer only receiving between 10-25% of the average PAR absorbed by the palisade mesophyll [14, 45, 47, 68, 74, 113, 163]. The spongy layer is thought to be of minor importance when it comes to CO_2 fixation, and is assumed to participate in reflecting light back to the palisade, while facilitating CO_2 diffusion to it [142, 148]. However, there is evidence pointing towards the spongy mesophyll being a more active participant of photosynthesis in shade-adapted plants [74]. For the purposes of this study, we will only consider the palisade mesophyll layer.

The identification of the palisade mesophyll layer, and subsequently the palisade air channel depth, is mostly done through visual inspection, as the palisade layer scans (both greyscale and binarised) are identified by a more regular arrangements of the cells and air channels, often in a columnar fashion, while the transition to spongy was indicated by a shift towards more porous slices, with bigger air spaces.

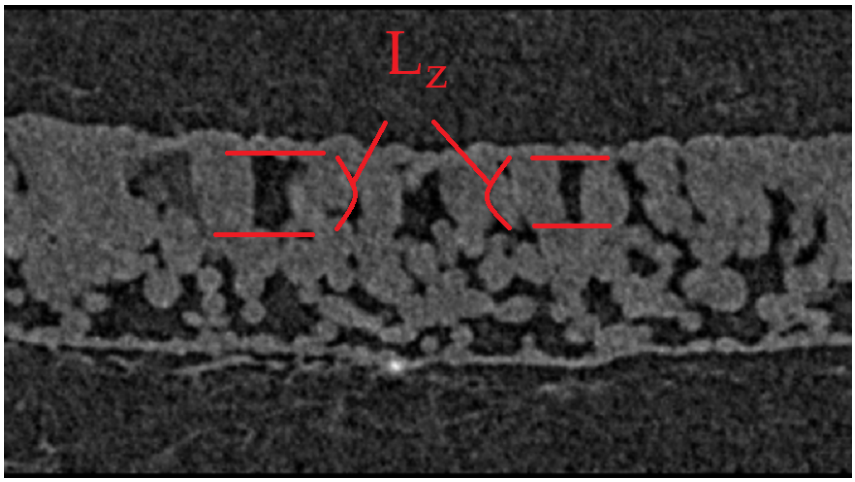

Figure 2.4: Zooming into a 3D reconstruction of the air channels of *Arabidopsis thaliana* to show individual air channels.

The palisade air channel perimeters were also observed to be much smaller than their spongy counterparts, and therefore we also used that as a marker of palisade layer identification, as shown in Fig. 2.5.

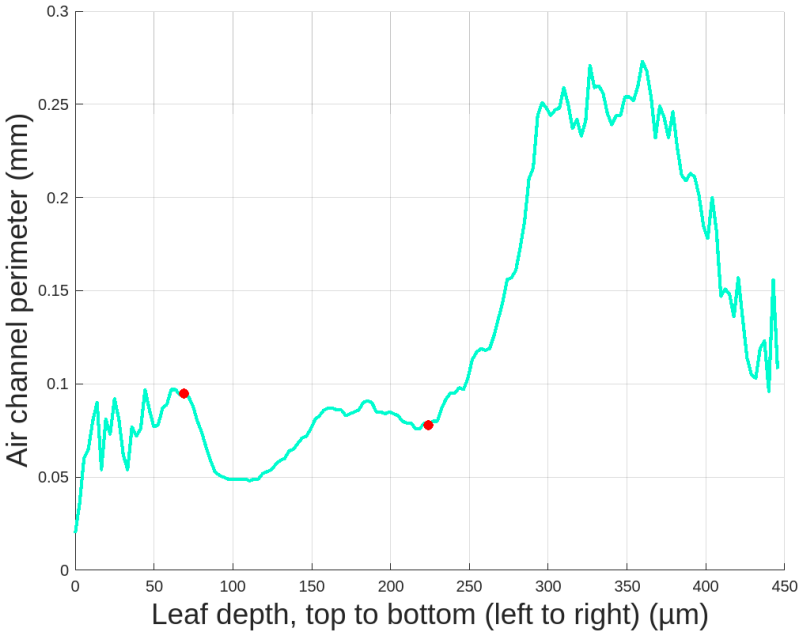

Figure 2.5: Measured average air channel diameter per slice against leaf depth for a *Arabidopsis thaliana* ($ATML1_{pro}$: KRP1) sample, showing that the transition from palisade to spongy layer can clearly be identified (red markers showing start and stop of palisade layer)

The slice numbers of the two markers were recorded, and the air channel depth. L_z, was calculated by:

$$L_z = n_{slice} \times \text{Resolution}, \tag{2.3}$$

where n_{slice} was the number of slices between (and including) the markers, and Resolution was the equal to the pixel, or spatial, resolution, which was the thickness of a single slice.

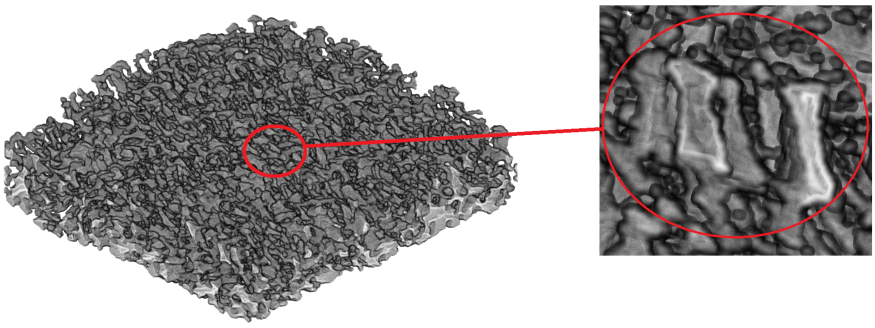

Figure 2.6: Greyscale horizontally resliced μ-CT scan of *Arabidopsis thaliana* showing the air channel depth identification.

Now that the palisade mesophyll layer was clearly identified, we could also obtained an average palisade air channel diameter for each sample:

$$\text{Average palisade air channel diameter, } \rho = \frac{(\sum \text{perimeter})/\pi}{\sum \text{n}_{\text{air channels}}}, \tag{2.4}$$

where $\sum$ perimeter is the sum of all air channel perimeters in all slices forming the palisade layer, and $\sum \text{n}_{\text{air channels}}$ is the total number of air channels in all slices forming the palisade layer.

Finally, the last structural descriptor of interest, palisade mesophyll porosity, was also calculated by:

$$\text{Porosity, P} = \frac{\sum \text{A}_{\text{air channels}}}{\sum \text{A}_{\text{m}}}, \tag{2.5}$$

where $\sum \text{A}_{\text{air channels}}$ and $\sum \text{A}_{\text{m}}$ are the sum of the area of air channels, and the mask area for all slices in the palisade layer. Note that the mask area contains both the air channel and cell areas within the leaf.

2.4 Gas Exchange Data Collection and Analysis

This section covers the collection of gas exchange data and the extraction of two photosynthetic traits of interest from said data. All the data was obtained pre-collected and paired to the μ-CT data, and the analysis of the gas exchange data was performed by the author of this thesis.

Gas exchange data was collected using a LI-COR gas exchange system (Li-6400 or Li-6800, depending on the source, but the principle remains the same). The apparatus has a clamp which shuts the leaf (or part of it) in an enclosed chamber where environmental conditions can be carefully controlled and monitored. Air flows through a reference Infra-Red Gas Analyser (IRGA), into the leaf chamber, and out a sample IRGA as shown below. Environmental variables such as light, CO_2 level, humidity, temperature, etc., are controlled to stable values.

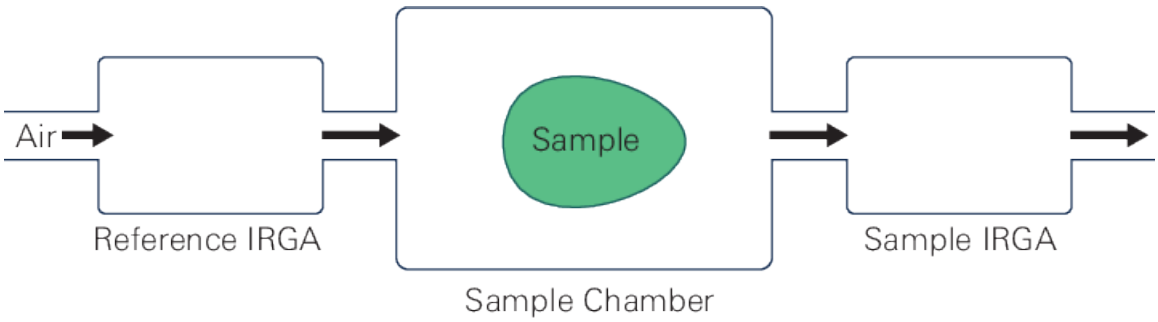

Figure 2.7: Simple schematic of how the Li-6800 collects data. [https://www.licor.com/env/support/LI-6800/topics/introduction.html], in the section 'The Gas Exchange System'.

The LI-COR system measures the flow rate of air entering and exiting the chamber, along with the concentrations of CO_2 and H_2O entering and leaving as well through a reference and sample IRGA [90]. The LI-COR system then computes the mass flow rate of said gases into and out of the chamber. The difference in CO_2 measurements, for instance, are due to leaf-level CO_2 assimilation. The intercellular CO_2 concentration, C_i, is also inferred by computing the difference (in and out) of all the fundamental parameters controlled and measured by the LI-COR system.

For gas exchange measurements, data is usually collected in the form of a response curve known as the $A - C_i$ curve, which depicts the relationship between leaf-level CO_2 assimilation rate, A, and intercellular CO_2concentration C_i. The process for this generally involves starting at ambient CO_2 (taking as 400 ppm in all of our data sources), and then incrementally decreasing the CO_2 level around the plant, all the while recording the associated assimilation value. It is important at this stage to ensure that the plant is not kept at low CO_2 for too long to prevent photosynthetic inhibition. The CO_2 level in the chamber is then incrementally raised back to ambient levels, and from that point onward, it is incrementally raised until the assimilation value plateaus to a saturation value. This gives us the CO_2 assimilation rate as a response to varying levels of CO_2 concentrations. An example of an $A - C_i$ curve is shown below.

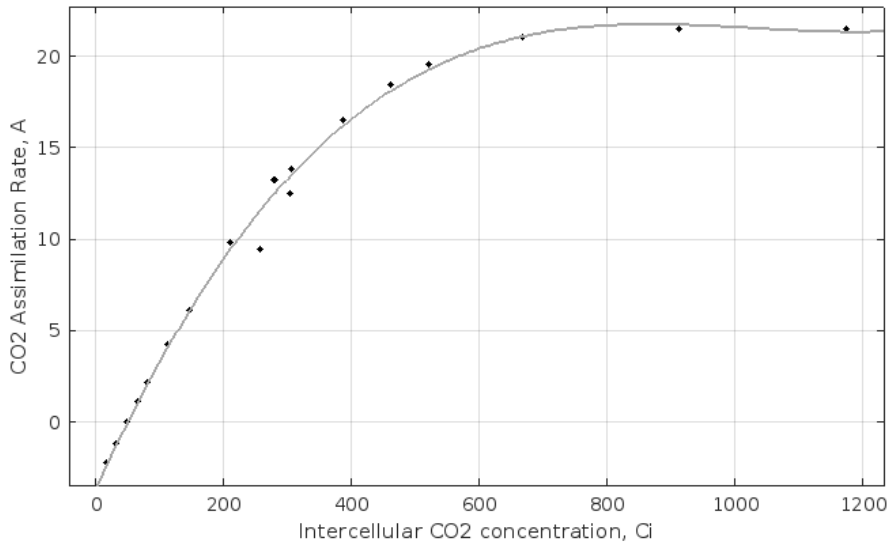

Figure 2.8: Example of an $A - C_i$ curve for *Arabidopsis thaliana*.

One of the photosynthetic traits we are interested in the is CO_2 assimilation rate at ambient CO_2 levels, referred to as A_{400} - generally a few data points are collected at this value, so we can obtain a more robust averaged value of A_{400} for each sample. The other photosynthetic trait we are interested in estimating is the mesophyll conductance to CO_2, g_m.

Mesophyll conductance is a complex measure of the conductance of CO_2 along its diffusional pathway, from the intercellular air channels, into the mesophyll cells and into the chloroplasts, where CO_2 assimilation occurs Flexas et al. [55, 56, 57]. It is still the subject of active research, and the decomposition and quantification of its individual diffusional pathways still require elucidating, largely owing to current technical limitations. There are several estimation methods and tools made available which allow for the estimation of g_m through anatomical methods, light responses curves, $A - C_i$ curves, or a combination of these, amongst others. We opted for a fitting tool presented by Sharkey [134], Sharkey et al. [135], which only required $A - C_i$ curves. This also ensured that our g_m were independent of our structural measurements (this doesn't necessarily mean that they are not related).

Through non-linear curve fitting (and minimising the sum of squared model deviation), the fitting tool allows the user to manually fit the data around 3 stages of

CO_2 assimilation limitations: RuBisCO limitation, RuBP-regeneration limitation, and TPU limitation, which we all briefly covered in Chapter 1, with the Long and Bernacchi [92] parameterisation of the FvCB model. An expression for g_m in terms of CO_2 partial pressure inside the chloroplast, $C_c = C_i - A/g_m$, can be substituted into parameterised expression for the RuBisCO and RuBP-regeneration limitations to obtain an estimated g_m. An example of the fitting tool used with some $A - C_i$ data is shown.

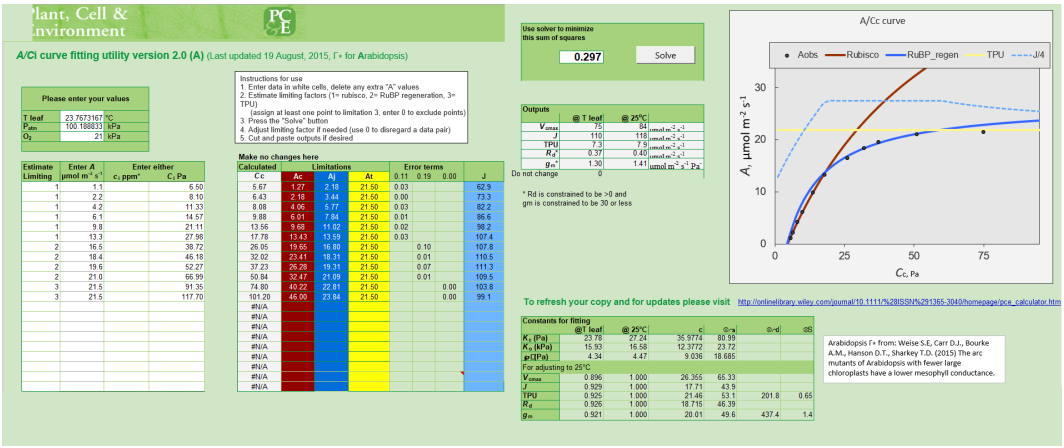

Figure 2.9: Example of the $A - C_i$ solver [134, 135].

Thus, we obtained estimations for two leaf-level photosynthetic traits, A_{400} and g_m, which were paired with local structural measurements of the palisade air channels per sample.

2.5 Mutant Characterisation

In this section, we bring the structural measurement and gas exchange measurements methods together to obtained paired datasets for a selection of *Arabidopsis thaliana* mutants that differ from wild-type *Arabidopsis thaliana* in their structure and photosynthetic performance. We have here selected Col-0 as the control. Col-0 is the commonest accession of the Colombia ecotype (collected natural line of *Arabidopsis thaliana*), and was obtained from Dr Alice Baillie (School of Biosciences, University of Sheffield) [4].

Figure 2.10: *Arabidopsis thaliana*, Col-0.

Each mutant is described in terms of palisade mesophyll structure and photosynthetic traits, relative to Col-0, and a binarised top-down μ-CT slice of the palisade mesophyll is presented next to a Col-0 slice after each mutant description (the slice is taken approximately from the middle of the palisade mesophyll, with black representing cellular material, and white representing air channels). The averaged structural and photosynthetic measurements for each mutant is shown in table 2.1 below. A set of bar charts comparing the collected parameters for each mutant (averaged) is also shown after the mutant descriptions. A more detailed table, per sample, is presented at the end of the chapter as well.

The following two lines (*EPF2-OE* & *focl*) are stomatal variants. As a reminder, stomata are the leaf's pores - they are formed by a pair of specialised cells known as guard cells found on the leaf's surface, and regulate gas exchange between the leaf and the atmosphere by opening and closing [170]. The mutants of interest here either have an altered density, or the stomatal cells themselves have been affected in a way that indirectly affects the underlying mesophyll structure. While we are not modelling stomatal effects directly in this thesis, it is worth noting that the formation of stomata and leaf mesophyll air spaces is known to be coordinated [4, 37], and hence these mutants could be of interest to us.

The *focl* line was obtained from Lundgren et al. [95], and described by Hunt et al. [72] and Hunt and Gray [71]. The *focl* mutants have had the final stages of formation of the cuticular ledge (an extension of the stomatal cell walls) disrupted. What this entails is that the stomatal opening is occluded, resulting in increased leaf temperature and reduced plant size, most likely as a consequence of limited CO_2 exchange. At leaf maturity, the majority (up to 90%) are still completely occluded, leaving only a small portion of stomata open, allowing for limited gas exchange. The *focl* line is characterised by poor CO_2 assimilation rate (the lowest in our set of mutants), low mesophyll conductance, and relatively larger air channels compared to Col-0 while having a similar palisade mesophyll porosity, which implies less cellular material is available for photosynthesis.

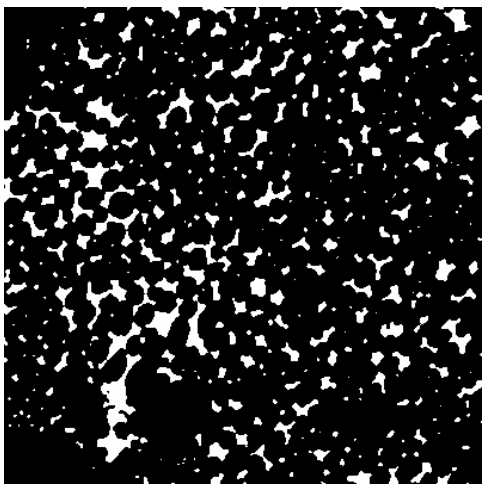

Figure 2.11: Binarised top-down view of Col-0 palisade mesophyll.

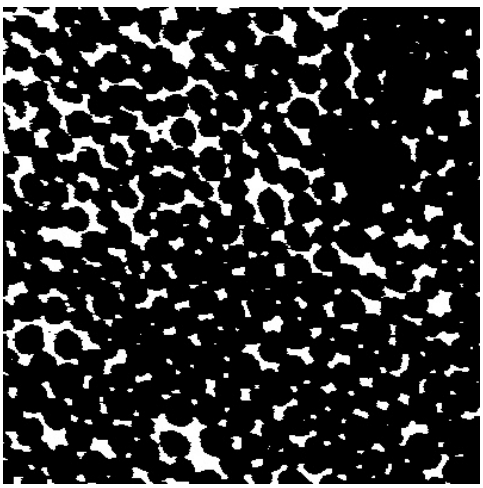

Figure 2.12: Binarised top-down view of *focl* palisade mesophyll.

The *EPF2-OE* line was also obtained from Lundgren et al. [95] and described by Hunt and Gray [70]. Here, the overxepression of *EPF2*, an epidermal patterning factor, led to a drastic decrease of stomatal density. Interestingly enough, on average, the palisade mesophyll porosity and air channel diameter of *EPF2-OE* mutants was similar to Col-0 and the photosynthetic traits were also comparable. However, it is to be noted that, individually, more variance was observed in the measured parameters for *EPF2-OE* than for Col-0. This later becomes apparent in the results of section 2 of Chapter 4.

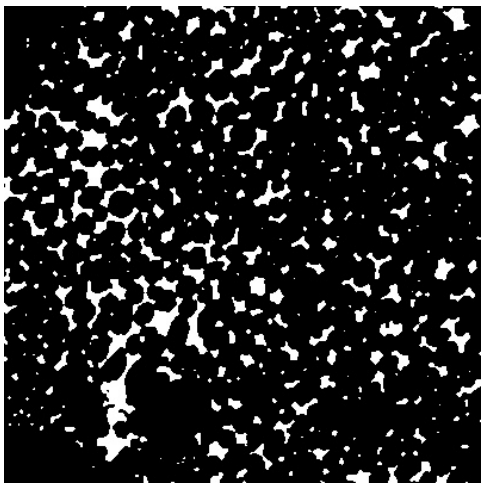

Figure 2.13: Binarised top-down view of Col-0 palisade mesophyll.

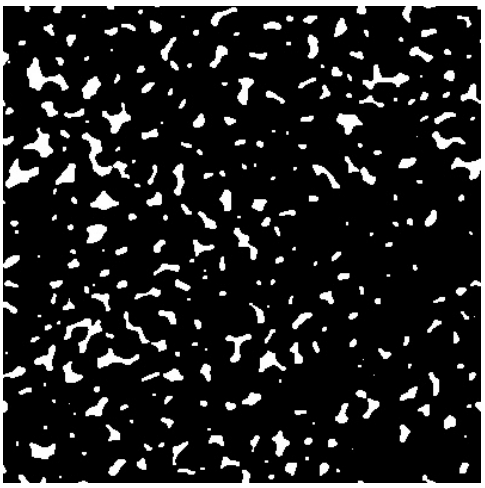

Figure 2.14: Binarised top-down view of *EPF2-OE* palisade mesophyll.

These following two lines (*arp3* & *qua2*) are impaired in their cell walls, and were both obtained from Baillie [4]. In plants, cell walls of adjacent cells adhere to one another through a cell wall layer called the middle lamella, which is rich in a polymer called pectin [169, 181]. The middle lamella must be manipulated to allow cells in the mesophyll to separate, but this separation must be carefully regulated to prevent the leaf from disintegrating. In these two lines from Baillie [4], the commonest type of pectin in the middle lamella, namely homogalacturonan (of which it is a major component) was affected, with reported effects to the cell separation and adhesion in the mesophyll [27].

The *arp3* line, as is mutant in a protein complex that regulates the actin cytoskeleton (which is involved in the process of cell division and leaf morphogenesis). More specifically, there is a disorganisation of the actin cytoskeleton, which leads to cell adhesion and cell shape defects Deeks and Hussey [32], Mathur et al. [102]. The cell adhesion defects extend to the epidermal cells [40], and also lead to stomatal opening defects [89]. According to Baillie [4], the μ-CT results of *arp3* are visually quite similar to Col-0, albeit with a recorded higher palisade mesophyll porosity and air channel diameter, as seen in table 2.1. The mesophyll conductance of *arp3* was low relative to Col-0, and the average CO_2 assimilation rate was also slightly lower.

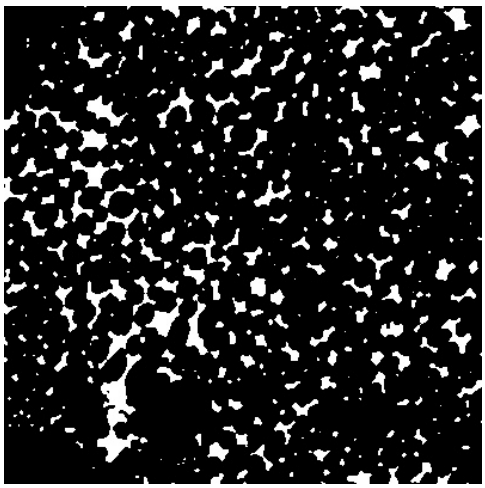

Figure 2.15: Binarised top-down view of Col-0 palisade mesophyll.

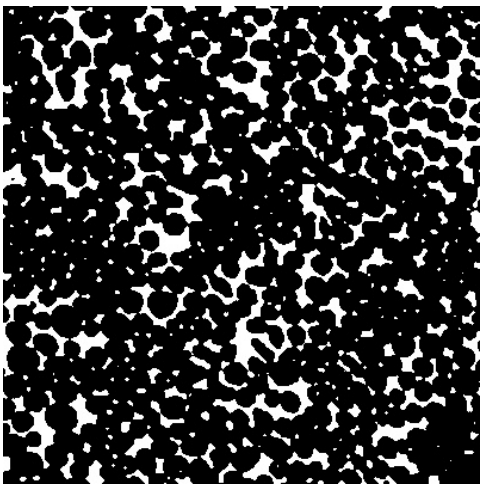

Figure 2.16: Binarised top-down view of *arp3* palisade mesophyll.

QUASIMODO2 (QUA2) is an enzyme involved in the pectin biosynthesis process (i.e., pectin generation) Mouille et al. [106]. The *qua2* mutation causes a defect in the pectin biosynthesis, leading to a large reduction in homogalacturonan (the commonest pectin type in the middle lamella, as stated earlier), leading to severe wall adhesion defects Barnes et al. [5], Du et al. [39], Mouille et al. [106], Whitewoods [168]. The *qua2* mutant can be classed as a 'dwarf' mutant. In the palisade mesophyll, this is characterised by an increased porosity, and fewer, larger air channels. Perplexingly, the *qua2* mutant outperforms Col-0 in terms of CO_2 assimilation. Baillie [4] observed that *qua2* had a similar stomatal density to Col-0 suggesting that the improvement in CO_2 assimilation was not related to any stomatal changes.

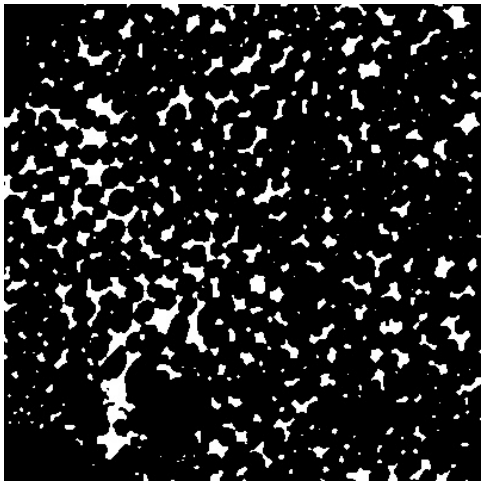

Figure 2.17: Binarised top-down view of Col-0 palisade mesophyll.

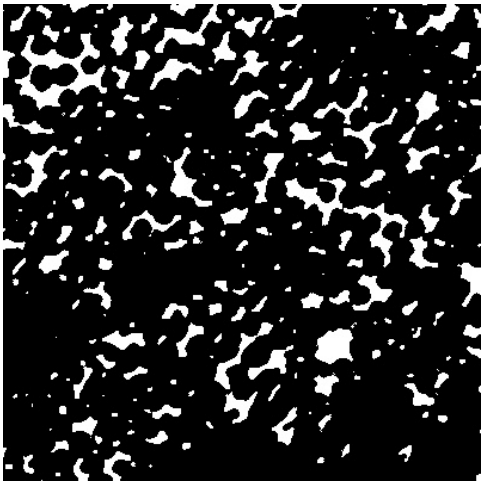

Figure 2.18: Binarised top-down view of *qua2* palisade mesophyll.

The $ATML1_{pro}$: KRP1 line is a transgenic mutant obtained from Lehmeier et al. [87]. This line is described by Lehmeier et al. [87] as a combination of targeting the *KRP1* expression to the mesophyll and expressing the gene behind the *ATML1* promoter, leading to an increase in epidermal cell size. More interestingly for us, this mutation also led to a significant decrease in mesophyll cell size, accompanied by an increased mesophyll cell density. Within the palisade, cells were more densely packed, leading to smaller air channels (with an increased density of air channels). $ATML1_{pro}$: KRP1 is characterised by a lower porosity than Col-0 in both the palisade and spongy mesophyll layers. Relative to Col-0, $ATML1_{pro}$: KRP1 mutants were found to have more circular air channels through the palisade. Photosynthetically, we observed a significantly higher mesophyll conductance, and slightly higher CO_2 assimilation rates.

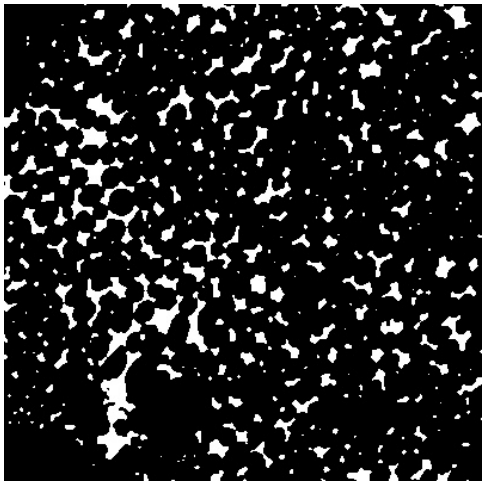

Figure 2.19: Binarised top-down view of Col-0 palisade mesophyll.

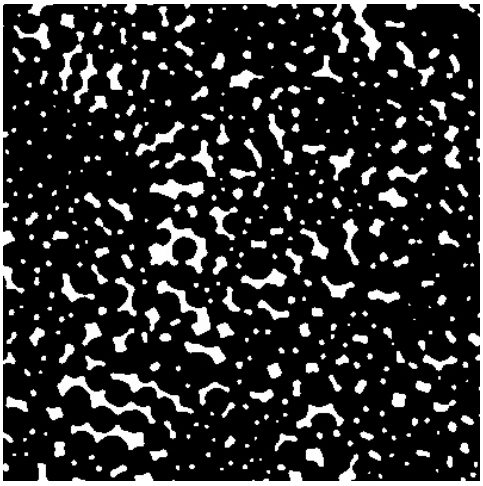

Figure 2.20: Binarised top-down view of $ATML1_{pro}$: KRP1 palisade mesophyll.

The *re6* mutant is the most 'extreme' line in our datasets. It was obtained as unused data originally collected for Lehmeier et al. [87], and its internal architecture is described by González-Bayon et al. [62]. It is a reticulate mutant (i.e., the leaf shows a more reticulated veination pattern) carrying the *re6* allele of the *RE* gene. This mutation here is very clear visually - *re6* leaves are described as having 'holes' in the matrix of mesophyll cells (i.e., very large gaps between cells). The cell proliferation is dramatically affected, leading to an extreme reduction in cell density in interveinal areas (which is specifically where we try to identify regions of interest for structural characterisation). Consequently, the density of cells containing chloroplasts is also greatly reduced, which, from a photosynthetic point of view, is reflected in a lower CO_2 assimilation rate (see table 2.1). It is to be clarified that while internal leaf structure is greatly disrupted, the development of plastids, such as chloroplasts (responsible for photosynthesis), is not. That implies that the reduced CO_2 assimilation rate is due to the dramatic reduction of photosynthetic cells, rather than a disruption of the photosynthetic process itself. On a leaf-level, leaf shape is seemingly not affected, but leaf size is greatly reduced. To summarise, the *re6* mutant is characterised by very large palisade air channel diameters, high porosity and a relatively lower CO_2 assimilation rate compared to Col-0. While the *whole* leaf thickness of *re6* was found to be lower than that of Col-0 [62], we observed that the palisade mesophyll thickness of *re6* was thicker.

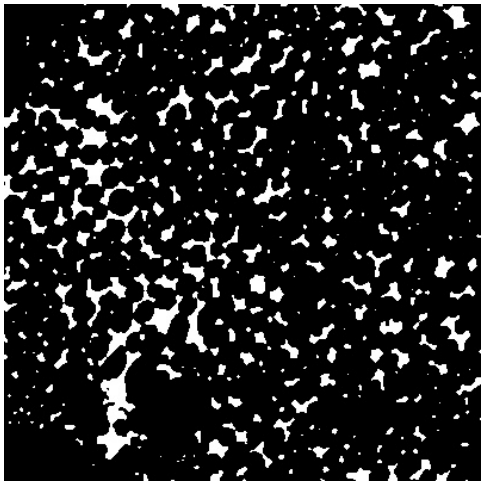

Figure 2.21: Binarised top-down view of Col-0 palisade mesophyll.

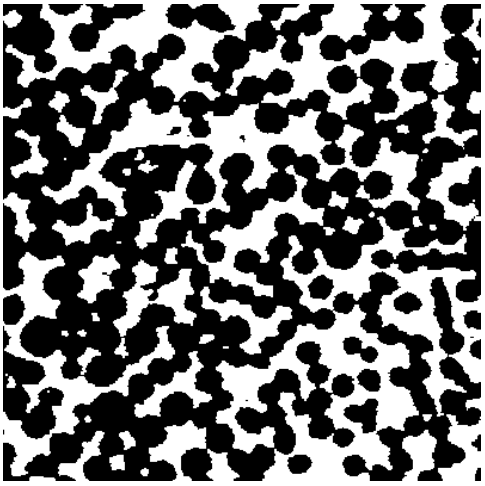

Figure 2.22: Binarised top-down view of *re6* palisade mesophyll.

To conclude, we have selected a range of *Arabidopsis thaliana* mutants from literature, that differ from wild type *Arabidopsis thaliana*, Col-0, either structurally in their palisade mesophyll, and/or in terms of photosynthetic performance. We have described a workflow adapted from published methods to extract simple but meaningful structural descriptors of the palisade mesopyhll air channels. We also analysed gas exchange data for each of the mutants, and extracted key photosynthetic traits, which we paired with the structural descriptors. Fig. 2.23, for instance, shows the relationship between palisade air channel depth and air channel diameter for a sample of each mutant, clearly showing the structural differences between each chosen mutant. Table 2.1 and Figures 2.24-2.28 show the averaged measured structural descriptors and photosynthetic traits for each mutant, and Table 2.2 shows the individual (per sample) parameters quantified for each mutant.

Table 2.1: Table of averaged structural and photosynthetic parameters per mutant line. Note that Porosity is shown as a ratio (range 0-1).

Mutant	Air Channel Depth L_z, µm	Average Air Channel Diameter ρ, µm	Measured Assimilation A_{400}, µmol m^2 s^1	Mesophyll conductance(25°C) g_m, µmol m^2 s^1Pa^1	Porosity P
Col-0	91.3	24.8	14.46	1.39	0.144
arp3	105.42	34.49	13.57	1.15	0.196
qua2	89.38	36.99	17.19	1.82	0.18
EPF2-OE	105.42	24.84	13.72	1.46	0.154
focl	135.85	28.7	10.93	1.18	0.143
$ATML1_{pro}$: KRP1	158.81	21.96	15.21	1.69	0.135
re6	176	107.49	11.24	1.35	0.321

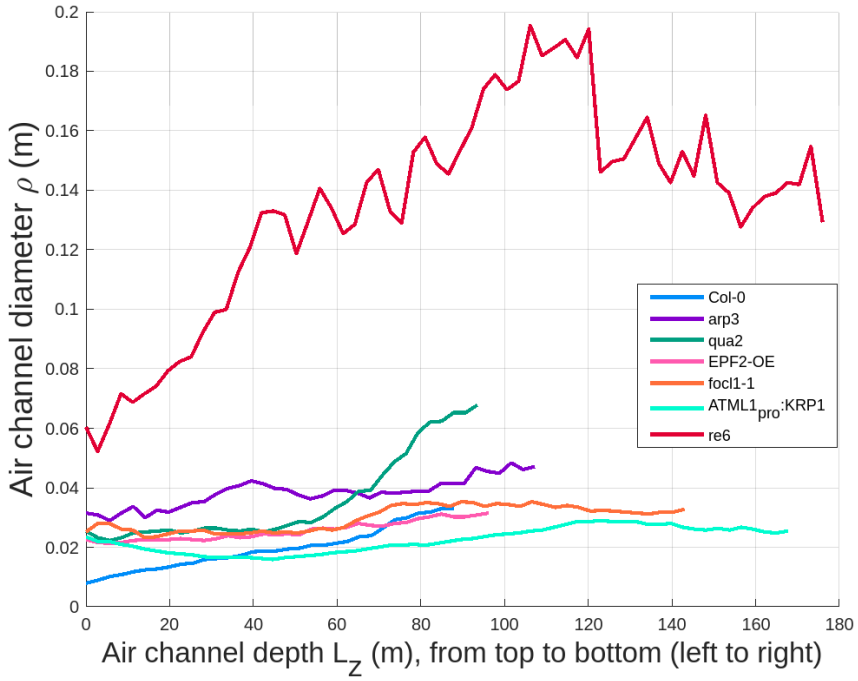

Figure 2.23: Air channel diameter with respect to air channel depth through the mesophyll for a single sample of each *Arabidopsis thaliana* mutant, showing the relative difference in both air channel diameters and depths.

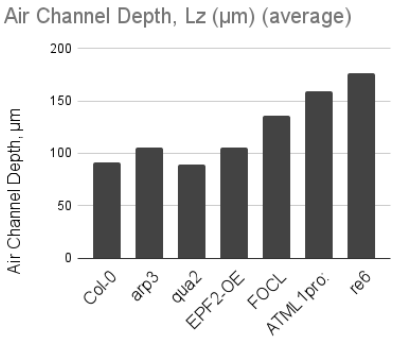

Figure 2.24: Air channel depth, L_z.

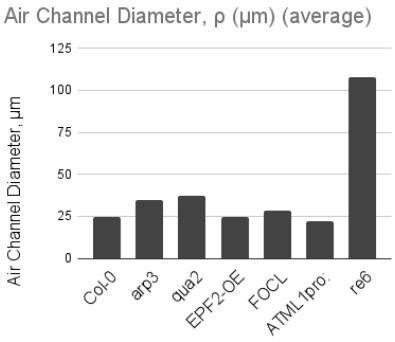

Figure 2.25: Air channel diameter, ρ.

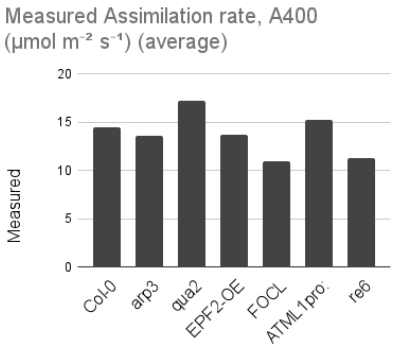

Figure 2.26: Measured CO_2 assimilation rate, A_{400}

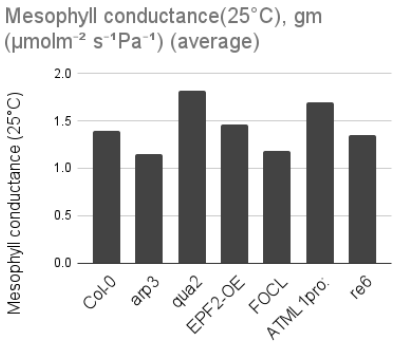

Figure 2.27: Mesophyll conductance to CO_2 (25 °C), g_m.

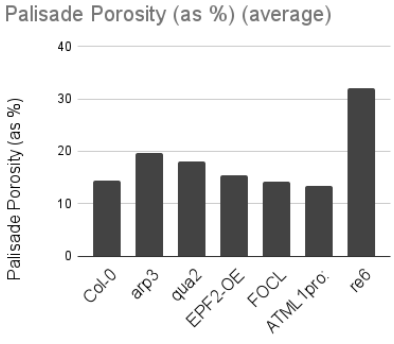

Figure 2.28: Palisade mesophyll porosity, P.

Table 2.2: Table showing all the collected structural and photosynthetic parameters for invididual samples. Note that if specified, u or d stands for up or down, and indicates where on the leaf/plant the sample was measured.

Mutant	Air Channel Depth µm	Air Channel Diameter , µm	Measured Assimilation µmol m^2 s^1	Mesophyll conductance(25°C) molm^2 s^1Pa^1	Porosity P (as a ratio)
Col-0_1	82.5	22.35	13.83	1.41	0.117
Col-0_2	88	19.55	14.16	1.32	0.125
Col-0_3	112.75	22.27	13.78	1.33	0.144
Col-0_5	88	26.4	15.04	1.34	0.157
Col-0_6	85.25	33.43	15.48	1.53	0.175
arp3_2	107.25	38.36	13.77	1.22	0.199
arp3_4	121	30.02	13.51	1.08	0.196
arp3_9	88	35.08	13.42	1.15	0.194
qua2_1	96.25	36.87	16.54	1.96	0.18
qua2_3	93.5	35.71	17.63	1.79	0.185
qua2_4	85.25	36.83	18.72	1.73	0.17
qua2_6	82.5	38.56	15.85	1.79	0.186
EPF2-OE_1	96.25	25.55	13.16	1.42	0.102
EPF2-OE_4	121	20.49	12.55	1.31	0.157
EPF2-OE_6	99	28.47	15.45	1.65	0.203
focl1-1_1d	143	29.76	12.37	1.25	0.146
focl1-1_2d	145.75	25.77	9.07	1.08	0.141
focl1-1_3u	123.75	29.83	8.83	1.12	0.132
focl1-1_4u	143	29.66	11.44	1.23	0.154
focl1-1_6u	123.75	28.46	12.92	1.24	0.142
$ATML1_{pro}$: KRP1_5u	156.75	22.79	14.68	1.57	0.126
$ATML1_{pro}$: KRP1_6u	176	22.5	16.18	1.61	0.18
$ATML1_{pro}$: KRP1_7u	167.75	22.43	14.84	1.77	0.122
$ATML1_{pro}$: KRP1_8u	134.75	20.11	15.15	1.79	0.099
re6_7u	170.5	87.93	10.25	1.18	0.273
re6_9u	176	134.83	12.26	1.45	0.427
re6_10u	181.5	99.72	11.21	1.42	0.263

Chapter 3

A Modelling Framework for Palisade CO_2 Uptake

3.1 The basis for a leaf structural model

In Chapter 1, we covered how key photosynthesis models were mostly biochemical in nature, being 'leaf-level' models and carrying no information about intercellular leaf structure. Past efforts to incorporate structural information often resulted in cumbersome equations (such as explicit integrations over individual planes in 3D) with little to no reliable data to test and validate such models appropriately [24, 121, 122]. Such models often relied on some hard to verify or dubious assumptions, such as uniform CO_2 concentration, which we now know to instead be a gradient of concentration across the mesophyll [112–114].

Such models were also conceived prior to modern imaging or measurement methods allowing for the precise quantification of intercellular structure in 3D. As covered in Chapter 2, the use of μ-CT methods allowed us to gain intimate knowledge of the intercellular air channel structure. In this chapter, we combine this structural data, paired with gas exchange measurements and knowledge of CO_2 diffusion to design a modelling framework for palisade CO_2 uptake within the air channels.

Air channels are modelled as uniformly distributed, discrete, vertical tubes, and the tissue between these channels is not cellularised within our model. While the tubes are represented as cylinders in our formulae and diagrams, it is important to note that the circle equation serves only to contribute to a nominal calculation of surface area, so the mismatch in cross-sectional shape between true air channels and our model is immaterial. Our simplified leaf is assumed to be amphistomatous, with CO_2 entering the leaf on both ends of the air channel [11, 38].

For the purposes of our model, photosynthesis is assumed to be in steady-state. While these conditions do not necessarily reflect field conditions, they are more representative of the carefully controlled lab environment under which the analysed samples plants are grown, allowing for a simpler mathematical analysis. Gas exchange measurements used to evaluate the model were also collected under steady state conditions [87, 95, 134]. Stomatal dynamics, which are an order magnitude slower than biochemical photosynthetic responses, are not considered here, as environmental conditions and water levels are also assumed to be constant for steady-state photosynthesis [160].

In the interests of simplifying the subsequent analysis, an assumption is made that the mesophyll conductance to CO_2 is constant throughout the depth of the palisade layer [49, 55, 116], implying the light intensity is uniform, as is the density of chloroplasts. This assumption will be challenged in the next chapter.

The leaf is assumed to be isobaric (at atmospheric pressure), and isothermic at a constant temperature of 25 °C (298.15 K). The leaf is also assumed to be under constant and saturating light (acclimated to high light), with constant water supply resulting in consistently turgid cells, implying that the cell shape does not change and in turn does not affect air channel shape [141]. We treat the cell water content as 100%, although in practice cells also contain a variety of solutes, proteins and lipid membranes [25].

The diffusion coefficient of CO_2 in air at 25 °C is taken as 1.39×10^{-5} $m^2\,s^{-1}$ from Pritchard and Currie [118]. Note that we also adopted a value of 400 ppm (in $\mu L\,L^{-1}$) for the concentration of CO_2 at atmospheric levels in Chapter 2, and this has to be converted to the SI units for molar concentration ($mol\,m^{-3}$). This results in a value of $\phi_{CO_2} = 0.0164$ $mol\,m^{-3}$. A more detailed calculation is given

in Appendix A.

3.2 Governing equation derivation

In 1994, at the end of his review of diffusion of CO_2 and other gases in leaves, Parkhurst [112] proposed that a single air channel in the palisade mesophyll could be modelled as a circular tube. The flux of CO_2 through the leaf is proposed to follow Fick's first law of diffusion, which states that diffusive flux is proportional to the concentration gradient, and dependent on temperature, viscosity and particle size [54]. In the proposed model, the air channels of the palisade mesophyll are abstracted as idealised microscopic tubes of length L_z and diameter ρ, with CO_2 concentrations at the base (CO_2 entry point) and top of the tube $\phi_{CO_2}(0)$ & $\phi_{CO_2}(L_z)$, respectively. Assuming steady-state photosynthesis, these CO_2 concentrations will be constant, with $\phi_{CO_2}(0) = \phi_{CO_2}(L_z)$. We begin by considering the net CO_2 flux within an infinitesimally small section (Δz) along the vertical axis of a single idealised air channel (Fig. 3.1). J represents diffusive flux, and $\phi_{CO_2}(z)$ is the concentration of CO_2 at depth z.

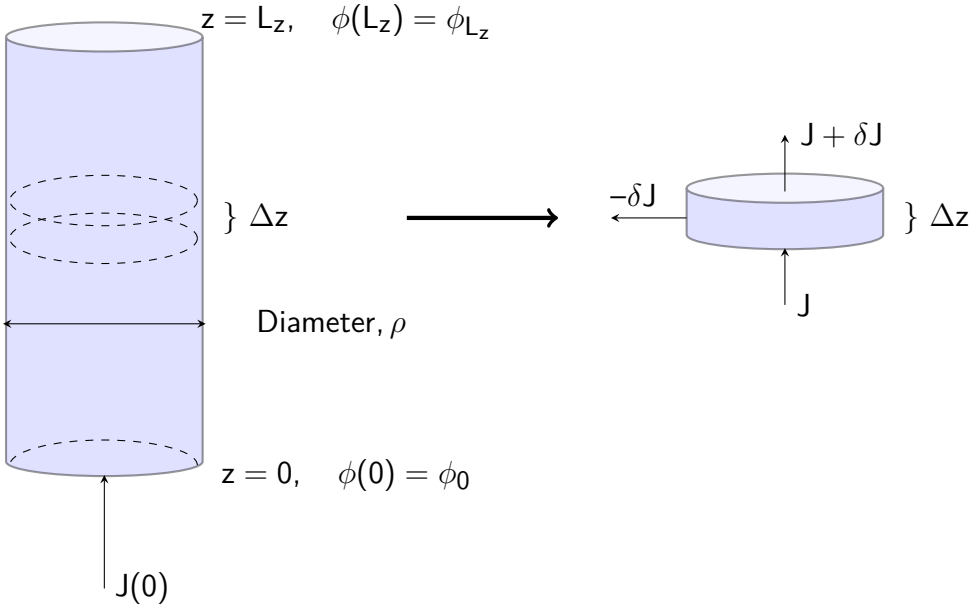

Figure 3.1: Idealised microscopic tube representation of palisade mesophyll air channel

Assuming steady-state photosynthesis, the net CO_2 uptake across the internal walls of an infinitesimal air channel slice of depth Δz is given by:

$$\frac{\pi\rho^2}{4} \times \delta J = -(\pi\rho\Delta z) G_{CO_2} \phi_{CO_2}(z),$$

$$\text{[Cross-sectional area]} \times \text{[Net flux difference]} = \text{[Volume of gas through walls]}, \tag{3.1}$$

where G_{CO_2} is a non-molar conductance coefficient to CO_2, representing the ease of CO_2 diffusion from the air channels into the cells. Expanding and simplifying equation (3.1) results in:

$$\begin{aligned} \delta J &= \frac{-4 G_{CO_2}}{\rho} \phi_{CO_2}(z) \Delta z, \\ \frac{\delta J}{\Delta z} &= \frac{-4 G_{CO_2}}{\rho} \phi_{CO_2}(z). \end{aligned} \tag{3.2}$$

According to Fick's first law, the diffusive flux of CO_2 is:

$$J(z) = -D_{CO_2} \frac{d^2 \phi_{CO_2}(z)}{dz^2}, \tag{3.3}$$

where D_{CO_2} is the diffusion coefficient of CO_2 in air. This can be substituted into equation (3.1):

$$\begin{aligned} -D_{CO_2} \frac{d^2 \phi_{CO_2}(z)}{dz^2} &= \frac{-4 G_{CO_2}}{\rho} \phi_{CO_2}(z), \\ \frac{d^2 \phi_{CO_2}(z)}{dz^2} &= \frac{4 G_{CO_2}}{\rho D_{CO_2}} \phi_{CO_2}(z). \end{aligned} \tag{3.4}$$

We thus obtain a diffusion-driven governing equation in the form of a second-order boundary-value ordinary differential equation, with a sink term G_{CO_2}, acting as a CO_2 conductance coefficient:

$$\frac{d^2 \phi_{CO_2}(z)}{dz^2} = \frac{\kappa^2}{\rho} \phi_{CO_2}(z); \quad \kappa = \sqrt{4 G_{CO_2} / D_{CO_2}}, \tag{3.5a}$$

with boundary conditions:

$$z = 0, \phi_{CO_2}(0) = \phi_{CO_2,0}, \tag{3.5b}$$

$$z = L_z, \phi_{CO_2}(L_z) = \phi_{CO_2(L_z),L_z}. \tag{3.5c}$$

A check of dimensional consistency between left and right hand sides of equation (3.5a) is in order here:

$$\frac{\text{mol}}{\text{m}^3}\frac{1}{\text{m}^2} = \frac{1}{\text{m}}\frac{\text{s}}{\text{m}^2}\frac{\text{mol}}{\text{m}^3} \times [\text{units of } G_{CO_2}],$$
$$\Rightarrow [\text{units of } G_{CO_2}] = \text{m}\,\text{s}^{-1}.$$

Hence, G_{CO_2} in this formulation is clearly different to how mesophyll conductance g_m is typically defined in the literature, with its units of $\mu\text{mol}\,\text{m}^{-2}\,\text{s}^{-1}\,\text{Pa}^{-2}$. This is resolved by applying a unit conversion proposed by Woodward et al. [172], and also seen in Muir [107]:

$$G_{CO_2} = T_K R g_m, \tag{3.6}$$

where T_K is the temperature in Kelvin, R is the molar gas constant and g_m is the mesophyll conductance to CO_2.

3.3 Model derivation

3.3.1 A solution for intercellular CO_2 concentration with respect to air channel depth

Using the boundary conditions at the bottom and top of a single palisade air channel given in (3.5b, 3.5c), the governing equation (3.5a) can be solved to obtain an expression for the intercellular CO_2 concentration in the air channel, as it varies with the depth of the air channel.

A general solution of the following form for (3.5a) can be assumed:

$$\phi_{CO_2}(z) = \alpha e^{\frac{\kappa}{\sqrt{\rho}}z} + \beta e^{-\frac{\kappa}{\sqrt{\rho}}z}. \tag{3.7}$$

The boundary conditions (3.5b are substituted 3.5c) into equation (3.7) to fix the coefficients α, $\beta \in \mathbb{R}$:

$$\phi_{CO_2}(0) = \alpha + \beta, \tag{3.8a}$$

$$\begin{aligned}
\phi_{CO_2}(L_z) &= \alpha e^{\frac{\kappa}{\sqrt{\rho}}L_z} + \beta e^{-\frac{\kappa}{\sqrt{\rho}}L_z}, \\
&= \alpha e^{\frac{\kappa}{\sqrt{\rho}}L_z} + (\phi_{CO_2}(0) - \alpha) e^{-\frac{\kappa}{\sqrt{\rho}}L_z}, \\
&= \alpha\left(e^{\frac{\kappa}{\sqrt{\rho}}L_z} - e^{-\frac{\kappa}{\sqrt{\rho}}L_z}\right) + \phi_{CO_2}(0) e^{-\frac{\kappa}{\sqrt{\rho}}L_z}, \\
\Longrightarrow \alpha &= \frac{\phi_{CO_2}(L_z) - \phi_{CO_2} e^{-\frac{\kappa}{\sqrt{\rho}}L_z}}{e^{\frac{\kappa}{\sqrt{\rho}}L_z} - e^{-\frac{\kappa}{\sqrt{\rho}}L_z}}.
\end{aligned} \tag{3.8b}$$

Inserting (3.8b) into (3.8a) yields:

$$\begin{aligned}
\beta &= \phi_{CO_2}(0) - \frac{\phi_{CO_2}(L_z) - \phi_{CO_2} e^{-\frac{\kappa}{\sqrt{\rho}}L_z}}{e^{\frac{\kappa}{\sqrt{\rho}}L_z} - e^{-\frac{\kappa}{\sqrt{\rho}}L_z}}, \\
&= \frac{\phi_{CO_2}(0) e^{\frac{\kappa}{\sqrt{\rho}}L_z} - \phi_{CO_2}(0) e^{-\frac{\kappa}{\sqrt{\rho}}L_z} - \phi_{CO_2}(L_z) + \phi_{CO_2} e^{-\frac{\kappa}{\sqrt{\rho}}L_z}}{e^{\frac{\kappa}{\sqrt{\rho}}L_z} - e^{-\frac{\kappa}{\sqrt{\rho}}L_z}}, \\
&= \frac{\phi_{CO_2}(0) e^{\frac{\kappa}{\sqrt{\rho}}L_z} - \phi_{CO_2}(L_z)}{e^{\frac{\kappa}{\sqrt{\rho}}L_z} - e^{-\frac{\kappa}{\sqrt{\rho}}L_z}}.
\end{aligned} \tag{3.9}$$

Hence the solution to (3.5a) is:

$$\begin{aligned}
\phi_{CO_2}(z) &= \frac{\phi_{CO_2}(L_z) - \phi_{CO_2} e^{-\frac{\kappa}{\sqrt{\rho}}L_z}}{e^{\frac{\kappa}{\sqrt{\rho}}L_z} - e^{-\frac{\kappa}{\sqrt{\rho}}L_z}} e^{\frac{\kappa}{\sqrt{\rho}}z} + \frac{\phi_{CO_2}(0) e^{\frac{\kappa}{\sqrt{\rho}}L_z} - \phi_{CO_2}(L_z)}{e^{\frac{\kappa}{\sqrt{\rho}}L_z} - e^{-\frac{\kappa}{\sqrt{\rho}}L_z}} e^{-\frac{\kappa}{\sqrt{\rho}}z}, \\
&= \frac{\phi_{CO_2}(L_z)\left(e^{\frac{\kappa}{\sqrt{\rho}}z} - e^{-\frac{\kappa}{\sqrt{\rho}}z}\right) + \phi_{CO_2}(0)\left(e^{\frac{\kappa}{\sqrt{\rho}}(L_z - z)} - e^{-\frac{\kappa}{\sqrt{\rho}}(L_z - z)}\right)}{2\sinh\left(\frac{\kappa}{\sqrt{\rho}}L_z\right)}, \\
&= \frac{2\phi_{CO_2}(L_z)\sinh\left(\frac{\kappa}{\sqrt{\rho}}z\right) + 2\phi_{CO_2}(0)\sinh\left(\frac{\kappa}{\sqrt{\rho}}(L_z - z)\right)}{2\sinh\left(\frac{\kappa}{\sqrt{\rho}}L_z\right)}, \\
&= \frac{\phi_{CO_2}(L_z)\sinh\left(\frac{\kappa}{\sqrt{\rho}}z\right) + \phi_{CO_2}(0)\sinh\left(\frac{\kappa}{\sqrt{\rho}}(L_z - z)\right)}{\sinh\left(\frac{\kappa}{\sqrt{\rho}}L_z\right)}.
\end{aligned} \tag{3.10}$$

Evaluating the left hand side of (3.5a) using (3.10) yields:

$$\begin{aligned}
\frac{d^2\phi_{CO_2}(z)}{dz^2} &= \frac{d}{dz}\left(\frac{\phi_{CO_2}(L_z)\frac{\kappa}{\sqrt{\rho}}\cosh\left(\frac{\kappa}{\sqrt{\rho}}z\right) - \phi_{CO_2}(0)\frac{\kappa}{\sqrt{\rho}}\cosh\left(\frac{\kappa}{\sqrt{\rho}}(L_z - z)\right)}{\sinh\left(\frac{\kappa}{\sqrt{\rho}}L_z\right)}\right), \\
&= \frac{\phi_{CO_2}(L_z)\frac{\kappa^2}{\rho}\sinh\left(\frac{\kappa}{\sqrt{\rho}}z\right) + \phi_{CO_2}(0)\frac{\kappa^2}{\rho}\sinh\left(\frac{\kappa}{\sqrt{\rho}}(L_z - z)\right)}{\sinh\left(\frac{\kappa}{\sqrt{\rho}}L_z\right)}, \\
&= \frac{\kappa^2}{\rho}\phi_{CO_2}(z),
\end{aligned}$$

hence proving that (3.10) is the solution to (3.5a). Solutions to (3.10) are shown in figure 3.2 for various values of air channel diameters ρ.

An important deduction can be made from the inspection of (3.10). In the limit $(\kappa/\sqrt{\rho}) \to 0$, corresponding to either negligible cell wall uptake, or very wide air channels, we should expect the concentration to linearly decrease from bottom to top of the channel. In other words, we expect a constant concentration gradient. This can be seen for air channels as big as the order of magnitue 10^{-4}, shown by the red line on figure 3.2.

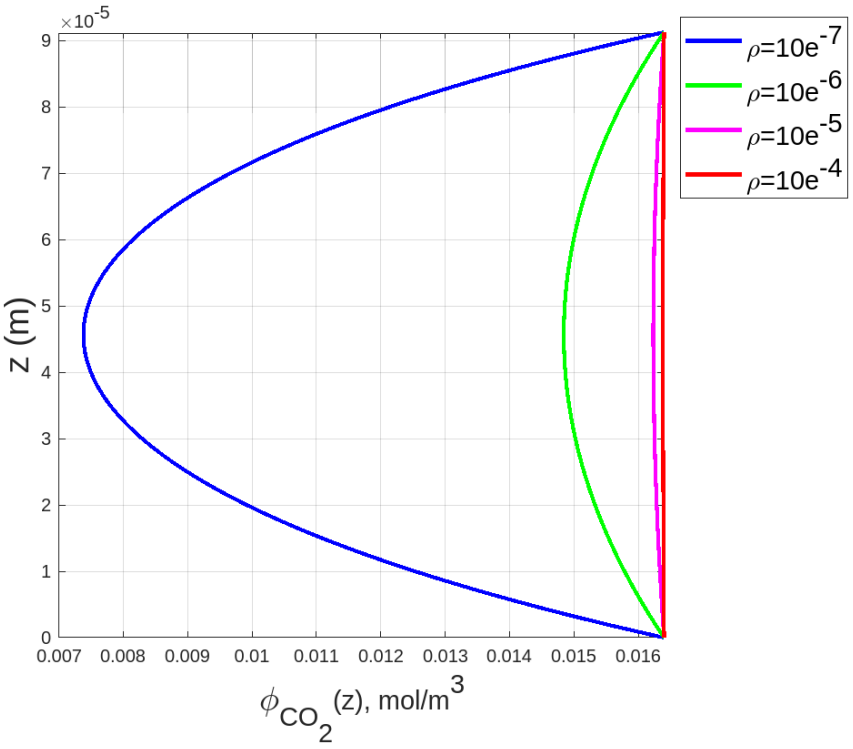

Figure 3.2: CO_2 concentration against air channel depth for various values of air channel diameter.

This can be more formally verified by applying L'Hôpital's rule:

$$\begin{aligned}
\frac{d}{dz}\left(\lim_{\frac{\kappa}{\sqrt{\rho}}\to 0}\phi_{CO_2}(z)\right) &= \frac{d}{dz}\left(\lim_{\frac{\kappa}{\sqrt{\rho}}\to 0}\frac{\frac{d}{d\frac{\kappa}{\sqrt{\rho}}}\left(\phi_{CO_2}(L_z)\sinh\left(\frac{\kappa}{\sqrt{\rho}}z\right)+\phi_{CO_2}(0)\sinh\left(\frac{\kappa}{\sqrt{\rho}}(L_z-z)\right)\right)}{\frac{d}{d\frac{\kappa}{\sqrt{\rho}}}\left(\sinh\left(\frac{\kappa}{\sqrt{\rho}}L_z\right)\right)}\right),\\
&= \frac{d}{dz}\left(\lim_{\frac{\kappa}{\sqrt{\rho}}\to 0}\frac{\phi_{CO_2}(L_z)z\cosh\left(\frac{\kappa}{\sqrt{\rho}}z\right)+\phi_{CO_2}(0)(L_z-z)\cosh\left(\frac{\kappa}{\sqrt{\rho}}(L_z-z)\right)}{L_z\left(\cosh\left(\frac{\kappa}{\sqrt{\rho}}L_z\right)\right)}\right),\\
&= \frac{d}{dz}\left(\frac{\phi_{CO_2}(L_z)z+\phi_{CO_2}(0)(L_z-z)}{L_z}\right),\\
&= \frac{\phi_{CO_2}(L_z)-\phi_{CO_2}(0)}{L_z}.
\end{aligned} \tag{3.11}$$

The observation made above is obtained, as expected.

3.3.2 CO_2 uptake rate formulation - 1D case

Equation (3.10) describes the air channel CO_2 concentration with respect to air channel depth z. The right hand side of (3.1) describes the CO_2 uptake, and (3.10) can be substituted back into it, and this can then be integrated with respect to air channel depth. From that, we can obtain an expression for U_{CO_2}, the *uptake rate* of CO_2 for a **single** palisade air channel:

$$
\begin{aligned}
U_{CO_2} &= \phi_{CO_2} G_{CO_2} \rho \int_0^{L_z} \phi_{CO_2}(z) dz, \\
&= \frac{\pi G_{CO_2} \rho}{\sinh\left(\frac{\kappa}{\sqrt{\rho}} L_z\right)} \int_0^{L_z} \phi_{CO_2}(L_z) \sinh\left(\frac{\kappa}{\sqrt{\rho}} z\right) + \phi_{CO_2}(0) \sinh\left(\frac{\kappa}{\sqrt{\rho}}(L_z - z)\right) dz, \\
&= \frac{\pi G_{CO_2} \rho}{\sinh\left(\frac{\kappa}{\sqrt{\rho}} L_z\right)} \frac{\sqrt{\rho}}{\kappa} \left[\phi_{CO_2}(L_z) \cosh\left(\frac{\kappa}{\sqrt{\rho}} z\right) - \phi_{CO_2}(0) \cosh\left(\frac{\kappa}{\sqrt{\rho}}(L_z - z)\right) \right]_0^{L_z}, \\
&= \frac{\pi G_{CO_2} \rho}{\sinh\left(\frac{\kappa}{\sqrt{\rho}} L_z\right)} \frac{\sqrt{\rho}}{\kappa} \left(\phi_{CO_2}(L_z) \cosh\left(\frac{\kappa}{\sqrt{\rho}} L_z\right) - \phi_{CO_2}(0) - \cdots \right. \\
&\left. \cdots - \phi_{CO_2}(L_z) + \phi_{CO_2}(0) \cosh\left(\frac{\kappa}{\sqrt{\rho}} L_z\right) \right), \\
&= \frac{\pi G_{CO_2} \rho^{3/2}}{\kappa \sinh\left(\frac{\kappa}{\sqrt{\rho}} L_z\right)} \left(\phi_{CO_2}(0) + \phi_{CO_2}(L_z) \right) \left(\cosh\left(\frac{\kappa}{\sqrt{\rho}} L_z\right) - 1 \right), \\
&= \pi G_{CO_2} \rho^{3/2} \left(\phi_{CO_2}(0) + \phi_{CO_2}(L_z) \right) \left(\coth\left(\frac{\kappa}{\sqrt{\rho}} L_z\right) - \operatorname{csch}\left(\frac{\kappa}{\sqrt{\rho}} L_z\right) \right).
\end{aligned}
\tag{3.12}
$$

It is interesting to see how this solution behaves for large and small values of air channel diameter ρ. Starting with small values of ρ, we note that:

$$
\coth\left(\frac{\kappa}{\sqrt{\rho}} L_z\right) - \operatorname{csch}\left(\frac{\kappa}{\sqrt{\rho}} L_z\right) \to 1 \text{ as } \rho \to 0, \tag{3.13}
$$

and hence $U_{CO_2} \to 0$ as $\rho \to 0$ also. This implies that, as the single air channel gets smaller with respect to its diameter, the CO_2 uptake rate also decreases. Proceeding to large values of ρ, the hyperbolic terms of the right hand side have

the following Taylor series expansions:

$$\coth\left(\frac{\kappa}{\sqrt{\rho}}L_z\right)) = \frac{\sqrt{\rho}}{\kappa L_z} + \frac{1}{3}\frac{\kappa}{\sqrt{\rho}}L_z + \cdots, \tag{3.14}$$

$$\operatorname{csch}\left(\frac{\kappa}{\sqrt{\rho}}L_z\right)) = \frac{\sqrt{\rho}}{\kappa L_z} - \frac{1}{6}\frac{\kappa}{\sqrt{\rho}}L_z + \cdots \tag{3.15}$$

Hence, from the leading order behaviour of (3.14) and (3.15) (i.e., the emergent behaviour of the term with the largest order of magnitude for each of these), the difference between the two terms decay as $\sim 1/\sqrt{\rho}$, and thus U_{CO_2} grows quasi-linearly with ρ as $\rho \to \infty$. Essentially, this analysis implies that for a single air channel, U_{CO_2} increases positively as air channel diameter ρ increases, and is largely a function of the air channel diameter ρ.

3.3.3 CO_2 uptake rate formulation - 2D case

The problem in the previous analysis is is is difficult to infer whole leaf behaviour from the results of a single air channel. The analysis suggests that as the air channel diameter increases, so does the CO_2 uptake rate. So this begs the question of why do leaves not have arbitrarily large air channels? There must be another as yet unmodelled factor to consider. We remind the reader here that we are actually interested in the amount of intercellular exposed surface area available for CO_2 diffusion, as it is known that CO_2 uptake and photosynthetic efficiency are intrinsically linked to the intercellular exposed surface area [2, 87] (and our model is conveniently formulated in a way that decomposes this into air channel diameter and depth). The problem here is that tube diameter has no influence on total surface area - one large air channel has the same surface area as two air channels of half the diameter, as highlighted in Ren et al. [124].

Leaves have a limited area within which the cells and air channels are arranged. It may therefore be more meaningful to introduce a constraint on a number of air channels within a given cross-sectional area, to more accurately represent the biology at hand. Let us assume that a number of air channels, N, are packed within a square cross-section of the leaf, with side length L_x, and area L_x^2, as shown in figure 3.3.

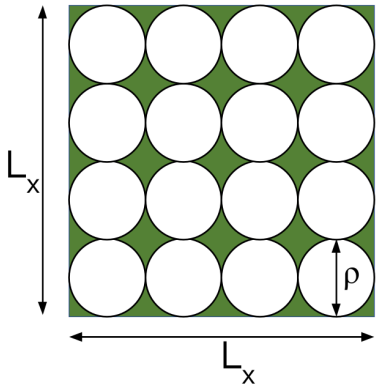

Figure 3.3: Top-down view of the assumed homogeneous palisade air channel arrangement within a bounded area.

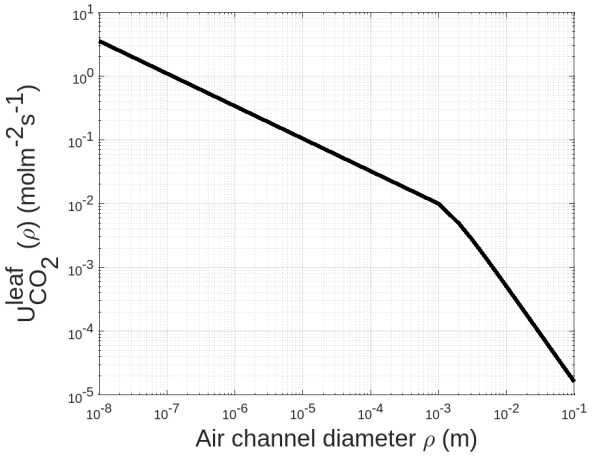

Figure 3.4: CO_2 uptake rate for the air channel arrangement on the left, as a function of air channel diameter.

Now, within this region of interest L_x^2, we have a constraint $L_x^2 = N\rho^2$, which gives us the number of air channels as $N = \frac{L_x^2}{\rho^2}$. To obtain the CO_2 uptake rate per leaf area, we can therefore multiply the expression for CO_2 uptake rate of a single air channel (3.12) by the number of air channels N, and divide it by the leaf (or region of interest) area L_x^2:

$$U^{leaf}_{CO_2} = N \times U_{CO_2} \times \frac{1}{L_x^2} = \frac{U_{CO_2}}{\rho^2}. \tag{3.16}$$

We can then compute (3.16) for a range of air channel diameters, resulting in Figure 3.4, with model parameters such as L_z and G_{CO_2} taken as averaged Col-0 values from table 2.2. Once more, using the relation from equation (3.13), it is clear that the CO_2 uptake rate of N air channels within a leaf area is now maximised when $\rho \to 0$. This bears more resemblance to reality, where a leaf might contain several smaller air channels, as opposed to a single large one. However, this is still not quite right. For very small air channels of the order of the mean free path of CO_2 molecules and smaller, we might expect a reduction in the CO_2 diffusion coefficient, and the assumption of Fickian diffusion may no longer hold, ceding its position to Knudsen (molecular) diffusion, another means of diffusion which is more prevalent when the diffusion path is on the same scale or smaller than the mean free path of the particles involved [88]. This observation also breaks down when considering that there are other gases present in the air channel, such as water

vapour, with much larger mean free path values than CO_2 implying that leaves most likely do not possess infinitesimally small air channels for gaseous diffusion. In addition to this, the mean free path for CO_2 at standard temperatures and pressures is $\sim 6 \times 10^{-8}$ m, which is approximately two orders of magnitude lower than observed air space diameters for *Arabidopsis thaliana* [87], pointing to other, more important factors.

3.3.4 CO_2 uptake rate formulation - 2D case with cell thickness

The assumed air channel arrangement in Figure 3.3 was headed in the right direction. However, in this arrangement, air channels are packed around each other, and are 'touching', implying that there is cellular material between two air channels, which lacks biological realism. In reality, one would expect the air channels to be arranged between packed cells in the palisade mesophyll. It is therefore more meaningful to revisit the constraint in Figure 3.3, where we now consider multiple air channels and the cell thickness, or d between them. The cell thickness d can be assumed to be one or more palisade cells in between air channels, where d is at least in the range of tens of μm, which is the scale expected for *Arabidopsis thaliana* cells [153, 173].

Consider a uniform arrangement of N air channels in an idealised leaf region of area L_x^2 (Fig. 3.5). d represents the spacing between air channels, occupied by cellular material, and its minimum value must be non-zero (cell thickness $d > 0$).

We can revisit the constraint L_x^2, which now results in $L_x^2 = N(\rho + d)^2$. We can now obtain an expression for CO_2 uptake rate for N channels per leaf area L_x^2 by multlying U_{CO_2} by the number of air channels N and dividing by L_x^2, resulting in:

$$U_{CO_2}^{leaf} = \frac{\pi G_{CO_2} \rho^{3/2} \left(\phi_{CO_2}(0) + \phi_{CO_2}(L_z) \right)}{\kappa (\rho + d)^2 \sinh\left(\frac{\kappa}{\sqrt{\rho}} L_z \right)} \left(\cosh\left(\frac{\kappa}{\sqrt{\rho}} L_z \right) - 1 \right). \tag{3.17}$$

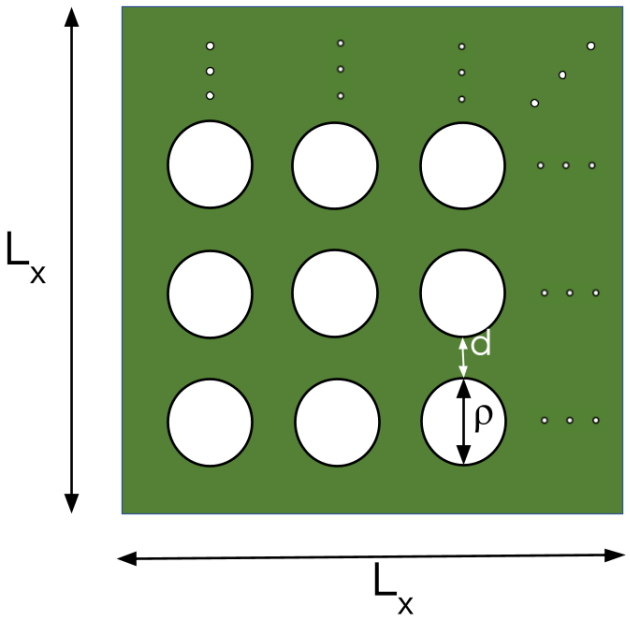

Figure 3.5: Top-down view of the assumed homogeneous palisade air channel arrangement within a bounded area.

Equation (3.17) allows us to estimate the total of CO_2 uptake per unit time for a given leaf area based on the number, diameter and spacing of the air channels within that leaf region. This model allows us to predict the optimal air channel diameter for CO_2 uptake, and to investigate how measured air channel diameters from real leaves compare to this prediction.

The new parameter for cell thickness, d, can also be calculated from the constraint $L_x^2 = N(\rho+d)^2$. In Chapter 2, we defined an expression for palisade porosity as:

$$\text{Porosity, } P = \left[\frac{\text{Total channel Area}}{\text{Total Mask Area}}\right]. \tag{3.18}$$

The total mask area here is L_x^2, and the total channel area is given by N times the area of one air channel (using the circle area equation). This means:

$$\text{Porosity, } P = \frac{N\pi\rho^2/4}{L_x^2} = \frac{N\pi\rho^2/4}{N(\rho+d)^2},$$

$$P = \frac{\pi\rho^2}{4(\rho+d)^2}. \tag{3.19}$$

We can rearrange (3.19) to obtain an expression for cell thickness, d, in terms of palisade porosity P and air channel diameter ρ:

$$d = \left(\frac{1}{2}\sqrt{\frac{\pi}{P}} - 1\right)\rho. \tag{3.20}$$

In our model (3.17), CO_2 uptake is dependent on the structural variables, air channel diameter ρ and cell thickness d, which in turn collectively determine air channel number, N, within a given leaf area. Our calculation also incorporates the conductance constant G_{CO_2} which depends upon temperature and g_m (mesophyll conductance to CO_2). Using measured values of these variables from paired x-ray μ-CT and gas exchange data sets from leaves of Arabidopsis plants, we are able to constrain certain parameters to investigate the effect of varying another.

We used measured values of mean air channel diameter, mean air channel depth and mean mesophyll conductance from our control, Col-0, to parameterise the model, and modelled the relationship between CO_2 uptake rate and air channel diameter by varying the value of ρ (Fig. 3.6). This analysis revealed that the relationship between $U^{leaf}_{CO_2}$, CO_2 and ρ has a unique global maximum, which represents the 'optimal' air channel diameter to maximise CO_2 uptake rate. This result makes intuitive sense: since the cell thickness, d, is fixed, CO_2 uptake within a given leaf area is limited at both small and large air channel diameters, as exposed mesophyll surface area is constrained by channel size or number respectively. The maximum exposed mesophyll surface area for a given leaf area is achieved with a medium number of medium-sized air channels. Essentially, with d fixed, at low porosities (small air channels) there is very little exposed intercellular surface area, and at high porosities (large air channels), there is once more very little exposed area with respect to the amount of cellular tissue available for photosynthesis [124, 150].

This result is consistent with the widely held notion that internal exposed mesophyll surface area, which in our model is determined by air channel diameter ρ, is a key structural parameter in the limitation of CO_2 uptake from the air channels into the mesophyll [87, 124, 125, 150].

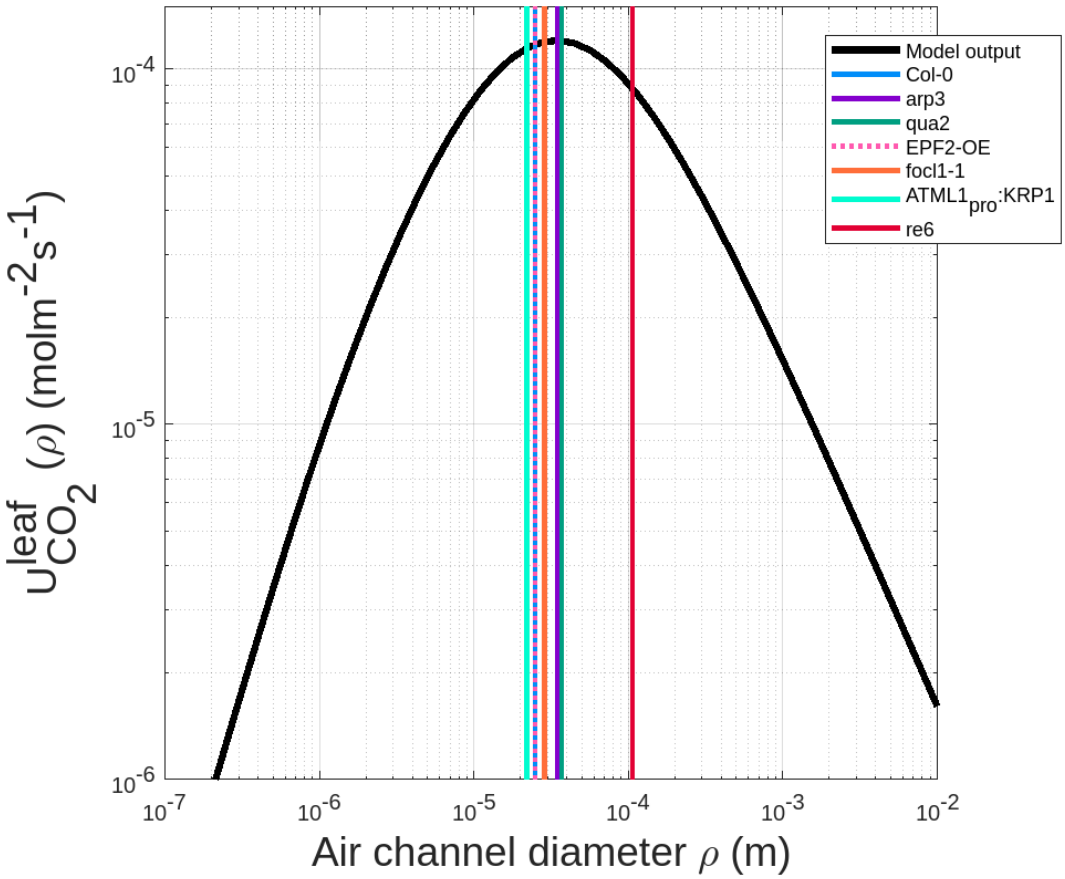

Figure 3.6: CO_2 uptake rate for N air channels per leaf area as a function of air channel diameter.

We compared the modelled optimum air channel diameter to the measured values from the same data set used to extract values for the parameters that we fixed (g_m and air channel inter-distance). The range of measure values for the air channel diameters of Arabidopsis mutants is represented by the coloured lines in Fig. 3.6. The modelled global optimum lies within the range of measured Arabidopsis air channel diameters. This alignment of experimental and theoretical data suggests that the model is successfully capturing some element of how air channel structure relates to CO_2 uptake within the leaf. It is worth highlighting *re6* (red line on Figure 3.6), which is a mutant with high porosity, and relatively lower CO_2 assimilation rate, also matches the observed notion that large air channels within a fixed leaf area limits photosynthesis.

Chapter 4

Predictive Modelling of Leaf Structure to Function

4.1 Introduction

With the CO_2 uptake rate model, CO_2 uptake is dependent on the structural variables air channel diameter ρ and cell thickness d, which in turn collectively determine air channel number, N, within a given leaf area. Our calculation also incorporates the conductance coefficient G_{CO_2} which depends upon temperature and g_m (mesophyll conductance to CO_2). Using measured values of these variables from paired x-ray μ-CT and gas exchange data sets from leaves of *Arabidopsis thaliana* plants, we are able to constrain certain parameters to investigate the effect of varying another parameter, notably highlighting the relationship between modelled CO_2 uptake rate $U_{CO_2}^{leaf}$ and air channel diameter ρ.

While modelled values for optimal air channel diameter are well-matched to measured values from Arabidopsis leaves, there is a discrepancy between the corresponding values of CO_2 uptake rate, with the model predicting CO_2 uptake around $7\times$ to $11\times$ greater than measured values (Table 4.1). This chapter covers the re-parameterisation of the CO_2 uptake rate model, exploring the difference between *measured* CO_2 *assimilation*, and the re-parameterised *effective* CO_2 *uptake*.

Table 4.1: Displaying the large scaling error between the measured and modelled CO_2 uptake rates for samples of wild-type Arabidopsis, Col-0

Sample	Measured CO_2 assimilation rate A_{400} [μmol m^{-2} s^{-1}]	Modelled CO_2 uptake rate $U^{leaf}_{CO_2}$[μmol m^{-2} s^{-1}]	Scaling error [$\frac{U^{leaf}_{CO_2}}{A_{400}}$]
Col-0_1	13.83	96.56	7.21
Col-0_2	14.16	117.18	8.28
Col-0_3	13.78	150.93	10.95
Col-0_5	15.04	111.44	7.41
Col-0_6	15.48	108.89	7.03

4.2 Cross-validated parameterisation of the CO_2 uptake rate model

We sought to identify the source of this error by considering each of the structural and physiological parameters that contribute to the calculation of CO_2 uptake. We deem the error unlikely to have arisen from structural parameters such as air channel diameter or air channel depth, as these can be visually checked. A more likely source of the discrepancy in modelled uptake and measured assimilation is either the calculated g_m value, which contributes to the conductance coefficient G_{CO_2}, or the unit conversion formula.

While we did assume that the conductance coefficient G_{CO_2} was an invariant parameter quantifying how CO_2 moves from the air channels into the cell tissue across the entire leaf, we should appreciate how complex the real situation really is. Our coefficient is calculated from the mesophyll conductance to CO_2 g_m, which describes how CO_2 reaches the sites of fixation within the chloroplasts after travelling though a number of biochemical and structural barriers, often varying on external environmental factors, and intracellular ones such as enzyme levels, or chloroplast size and density [55, 94, 151, 174]. As discussed in the model derivation, g_m is estimated solely from $A - C_i$ (gas exchange) data, largely ignoring some of these highly variable factors. In addition to this, a very simplistic conversion equation (3.6) was assumed, only accounting for the leaf temperature. It might be more realistic to model several stages of the mesophyll conductance and implement several of these factors, for instance modelling intercellular airspace conductance

and liquid phase conductance. Unfortunately, measurements, or even estimates of several required parameters are largely unavailable due to current technical limitations, or rely on even more assumptions, and attempting to quantify these for a line of mutants would be ambiguous at best [57].

While the model captures several key structural parameters, internal mechanisms that are not captured have no explicit descriptors, and the biochemical properties are largely represented by a global value per leaf through the conductance coefficient G_{CO_2} . Therefore, the error is indeed likely to lie in how this factor is estimated: some mutants, albeit having a similar palisade structure, can have a different conductance coefficients (Col-0 and *arp3*, for instance, have rather similar intercellular air channel structures, but *arp3* has a much lower mesophyll conductance and lower CO_2 assimilation rate). This could be due to a multitude of factors that are not captured by the generalised CO_2 uptake model, such as varying chloroplast concentrations inside the cells, different internal pathway lengths (e.g., different cell membrane thicknesses, or different RuBisCO concentrations or activity levels).

Another potential source of error is the assumed CO_2 concentration at the top and bottom of the air channel. We assumed amphistomatous behaviour, but the abaxial and stomatal densities of *Arabidopsis thaliana* could vary, leaning more towards hypostomatous behaviour [185].

A two-fold sensitivity analysis is in order to assess which of these is most likely to be the source of discrepancy. Figure 4.1 illustrates the CO_2 uptake rate model as a function of G_{CO_2} (i.e., $U^{leaf}_{CO_2}(G_{CO_2})$). Structural values such as air channel diameter ρ are taken from Col-0 values, and the adaxial CO_2 concentration is taken at 100%, 50% and 25% of the abaxial CO_2 concentration over three runs of the model.

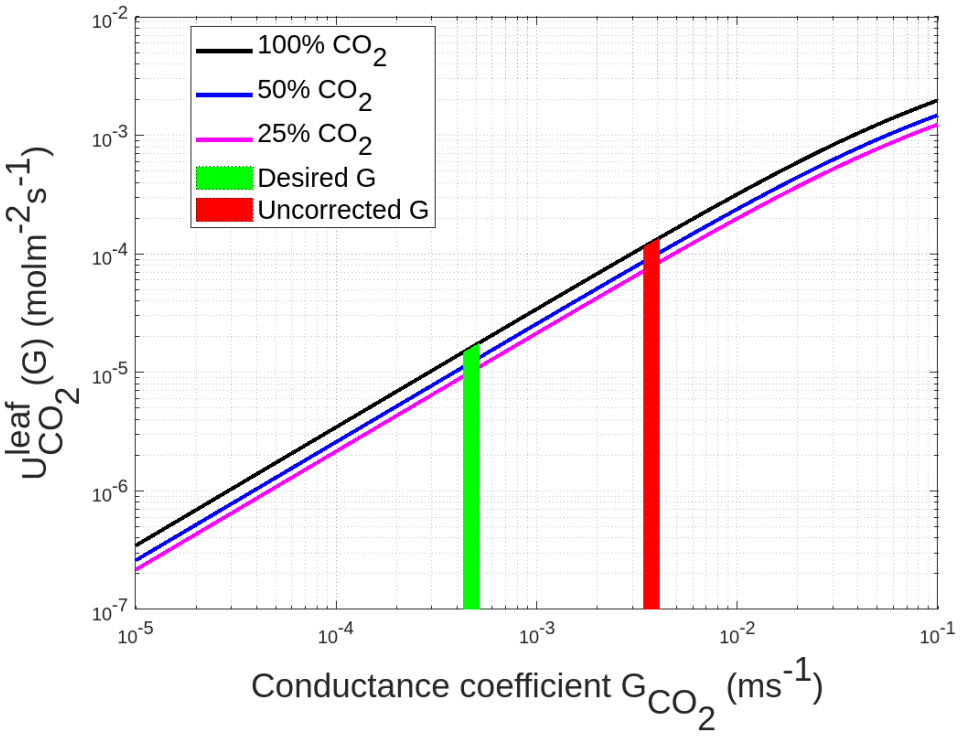

Figure 4.1: CO_2 uptake rate as a function of the CO_2 conductance coefficient, for 3 different boundary conditions of CO_2 concentrations.

This sensitivity analysis supports the hypothesis that the source of error is indeed likely to be the calculated G_{CO_2} using the conversion equation (3.6), which is also leading to an overestimation of $U^{leaf}_{CO_2}$ by roughly an order of magnitude.

To test our hypothesis that the scaling error arises from the conductance coefficient G_{CO_2}, we equated the modelled CO_2 uptake rate ($U^{leaf}_{CO_2}$) to the measured CO_2 assimilation rate (A_{400}) values, and numerically solved for a value of G_{CO_2}, referred to as *desired* G_{CO_2} to distinguish it from that derived from equation (3.6). The scaling error for values of *desired* G_{CO_2} against calculated G_{CO_2} matched the errors observed in table 4.1 in terms of order of magnitude.

This test, along with Table 4.1 and Fig. 4.1, seems to show that a lot more CO_2 diffuses from the air channel into the mesophyll tissue than the amount of CO_2 that is assimilated, suggesting that this process of conversion from diffusion to assimilation is quite inefficient. In fact, C3 photosynthesis is well documented to be quite an inefficient process. One of the major culprits behind this lack of efficiency in converting diffused CO_2 is the catalytic enzyme RuBisCO, one of the

enzymes behind the C3, or Calvin Cycle, that we gave an overview of in Chapter 1 [120]. RuBisCO in an enzyme with a very low turnover and surprisingly low affinity for CO_2, given its central role in photosynthesis [164]. To make things worse, it also catalyses two competing reactions: carboxylation and oxygenation (through photorespiration) [117]. The carboxylation part is what leads to the photosynthetic carbon cycle, where CO_2 is eventually assimilated by the leaf [143]. The oxygenation causes a loss of already fixed CO_2, and can lower photosynthetic output by 25-30% [133].

The level of detail in both our paired structural/gas exchange datasets, and our model parameters does not allow us to make the clear assertion that RuBisCO is the sole culprit behind the CO_2 uptake model overestimating its output. However, we can at least appreciate that it may be a factor (and one of many unmodelled parameters) behind this inefficiency. It is clear that there are also be other factors at play here, For instance, water vapour flux inside the air channels (where CO_2 also diffuses) was found to be a major limitation of maximising photosynthetic gas exchange in coffee plants, leading to a large diffusional resistance (which implied low chloroplastic CO_2), while the coffee RuBisCO was tuned to operate at low chloroplastic CO_2 conditions [100].

What we can do to remediate this situation, however, is fit our model using the measured gas exchange parameters (both A_{400} and g_m) to re-parameterise the model, which then should allow us to get a prediction on the '*effective*' CO_2 uptake rate, i.e., a prediction on the amount of CO_2 that is diffused into the mesophyll and actually used. We can centre this around G_{CO_2}, and introduce a correction term in equation (3.6) - a term which will arise out of the fitting process.

The inclusion of such terms when fitting models built from first principles to measured data is not uncommon. One example that might be relevant here is a modelling framework designed by Parkhurst and Mott [113] to investigate the extent to which CO_2 diffusion limits CO_2 assimilation, developed from a previous model by Kirschbaum and Farquhar [83]. A term β was included to account for both unit conversions and the change from CO_2 diffusion rate from one point to the CO_2 assimilation rate at that point.

Going back to our own modelling framework, let us introduce a correction factor

for G_{CO_2}, η, required to make the model output match measured assimilation values (i.e., finding out a value of G_{CO_2} such that the model output is equal to the measured value) , resulting in a modified Woodward equation (equation (3.6)):

$$\hat{G}_{CO_2} = \eta g_m R T_K, \tag{4.1}$$

where $\hat{G}_{CO_2}$is the corrected conductance coefficient, obtained from numerically solving our model for the case when $U^{leaf}_{CO_2} = A_{400}$ (i.e., modelled output is equal to the measured value). We used the results in to calculate a corresponding η for each Col-0 sample, then applied the **Leave-One-Out (L-O-O) cross validation** method of parameter tuning, which generally produces low bias for small sample sizes [18]. This method excludes each sample in turn, and merges the other samples to form a mean correction weight $\bar{\eta}$. Taking a sample set that has 3 samples (i.e., $n = 3$) for instance, the correction on the *first* sample would be:

$$\hat{G}_{CO_2,1} = \bar{\eta}_{2,3} \times g_{m,1} \times R T_K, \tag{4.2}$$

where $\bar{\eta}_{2,3}$ is the mean of the correction factors of the remaining (*second and third*) samples, and $g_{m,1}$ is the mesophyll conductance of the first sample. The corrected conductance coefficients do greatly improve the match between measured and modelled uptake rates. Table 4.2) shows the new '*effective*' CO_2 uptake rates from the model against measured CO_2 assimilation rate values, along with the scaling error, for all of our Col-0 samples.

Table 4.2: Modelled '*effective*' CO_2 uptake rate for Col-0.

Sample	Measured CO_2 assimilation rate $A_{400}[\mu mol\, m^{-2}\, s^{-1}]$	Modelled effective CO_2 uptake rate $U^{leaf}_{CO_2}[\mu mol\, m^{-2}\, s^{-1}]$	Scaling error $[\frac{U^{leaf}_{CO_2}}{A_{400}}]$
Col-0_1	13.83	11.78	1.14
Col-0_2	14.16	14.91	0.95
Col-0_3	13.78	20.59	0.67
Col-0_5	15.04	13.67	1.10
Col-0_6	15.48	13.11	1.18

Interestingly, when we carry out the same process of correction factor calculation on other Arabidopsis mutants, we find that the factor varies per mutant. In order to quantify how the modelled '*effective*' CO_2 uptake rate of our chosen

Arabidopsis thaliana mutants differ from the control Col-0, we introduced an extra term, $\boldsymbol{\alpha}$, such that:

$$\boldsymbol{\eta}_{\text{mutant}} = \boldsymbol{\alpha}_{\text{mutant}} \times \bar{\boldsymbol{\eta}}_{\text{Col–0}}, \tag{4.3}$$

where $\bar{\boldsymbol{\eta}}_{\text{Col–0}}$ is the average correction weight of all Col-0 samples. The $\boldsymbol{\alpha}$ term, which shall be referred to as the *deviation factor*, is the correction weight for mutants normalised by the correction weight of Col-0, providing us with a quantified measure of how mutants *deviate* from the control samples of Col-0 in terms of the prediction of '*effective*' CO_2 uptake rate (Note that this implies $\boldsymbol{\alpha} \approx$ 1 for Col-0).

We can therefore obtain a corrected and cross-validated prediction on the effective CO_2 uptake rate within the palisade through the inclusion of a correction factor $\boldsymbol{\eta}$ obtained from fitting measured gas exchange data to the model. Through the inclusion of an extra term $\boldsymbol{\alpha}$, we can also quantify the performance of our selection of mutants relative to the control line.

Table 4.3 shows the average comparison between the measured CO_2 assimilation rates and the predicted effective CO_2 uptake rate values. Some of the larger prediction errors arise from an observed variance in the measured CO_2 assimilation rate, calculated mesophyll conductance and air channel measurements for certain mutants, such as *EPF2-OE*.

Table 4.3: Average corrected performance, characterised for each mutant.

Sample	Deviation factor $\boldsymbol{\alpha}$	Measured CO_2 assimilation rate A_{400} [μmol m^{-2} s^{-1}]	Modelled effective CO_2 CO_2 uptake rate $U^{\text{leaf}}_{CO_2}$ [μmol m^{-2} s^{-1}]	Mean scaling Error $[\frac{U^{\text{leaf}}_{CO_2}}{A_{400}}]$
Col-0	1.00	14.46	14.81	1.01
arp3	1.01	13.57	14.16	1.02
qua2	1.11	17.19	17.61	1.01
EPF2-OE	1.20	13.72	23.60	0.67
focl	0.69	10.93	11.06	1.01
$ATML1_{pro}$: KRP1	0.54	15.21	17.33	0.96
reб	0.96	11.24	11.40	1.00

Fig. 4.2 shows the modelled '*effective*' CO_2 uptake rates plotted against the measured CO_2 assimilation rates for all individual samples of all mutants, with a reference line showing the case where the model perfectly predicts the measured value (i.e., modelled value = measured value). The model output looks reasonable for all mutants except perhaps for *EPF2-OE* where it overestimates some samples by a larger margin than the rest of the mutants. This is likely due to a higher variance observed in the measured values of CO_2 assimilation rate, mesophyll conductance and air channel diameter for *EPF2-OE* as seen in table 2.2.

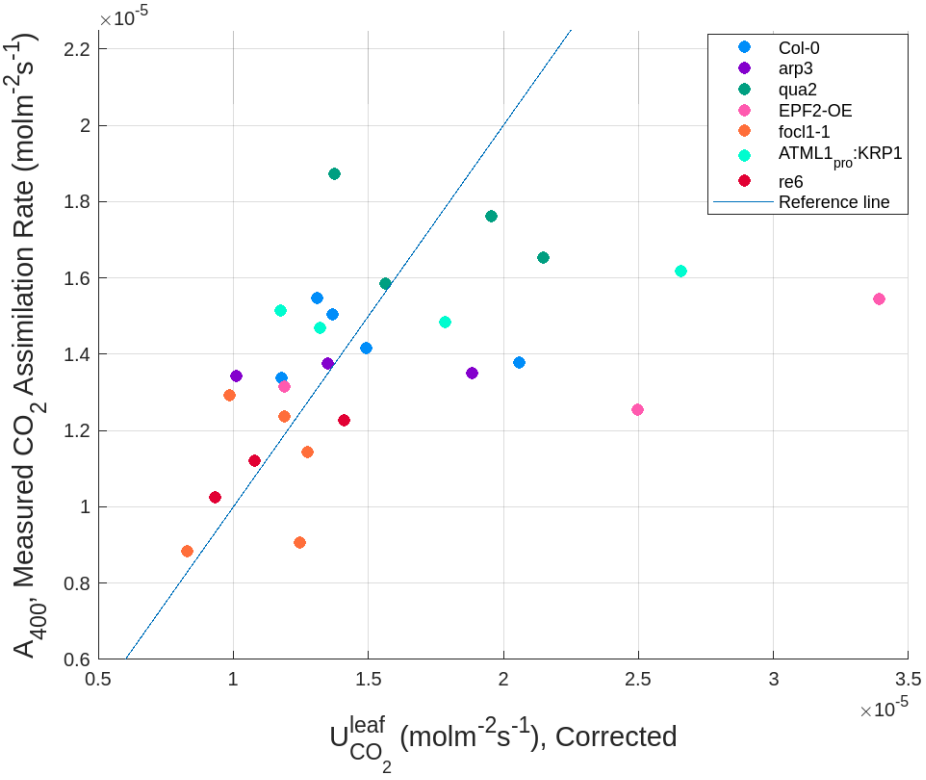

Figure 4.2: *Effective* CO_2 uptake rate model outputs plotted against *measured* CO_2 assimilation rates per sample of each mutant. The straight line represent the case where the modelled output perfectly matches the measured assimilation rate.

We also saw in Chapter 3 (specifically equations (3.14), (3.15)) that the model behaviour was modulated in large part by the air channel diameter, and our *EPF2-OE* samples were had a large range of values for that parameter. This shows that the model is sensitive to sample sets that have a high variance, and may tend to under or over predict for such samples.

The main result from Chapter 3 (Fig. 3.6) can be repeated now that knowledge from the measured gas exchange data has been fully incorporated into the model via parameter fitting. The result is now much more reflective of the observations done during mutant characterisation in Chapter 2.5. For instance, the averaged Col-0 performance with respect to air channel diameter lies on the curve (fitted for Col-0). The *qua2* mutant, despite structural defects leading to enlarged air channels, clearly performs better than Col-0. The $ATML1_{pro}$: KRP1 line has slightly smaller air channels (and smaller cells), and also performs better, which lines up with the observation from Théroux-Rancourt et al. [150] that densely packed, smaller cells are linked with increased CO_2 diffusion, and hence uptake. Once more, the *re6* mutant, with extreme palisade mesophyll structure defects (very large air channels), is seen to perform relatively poorly.

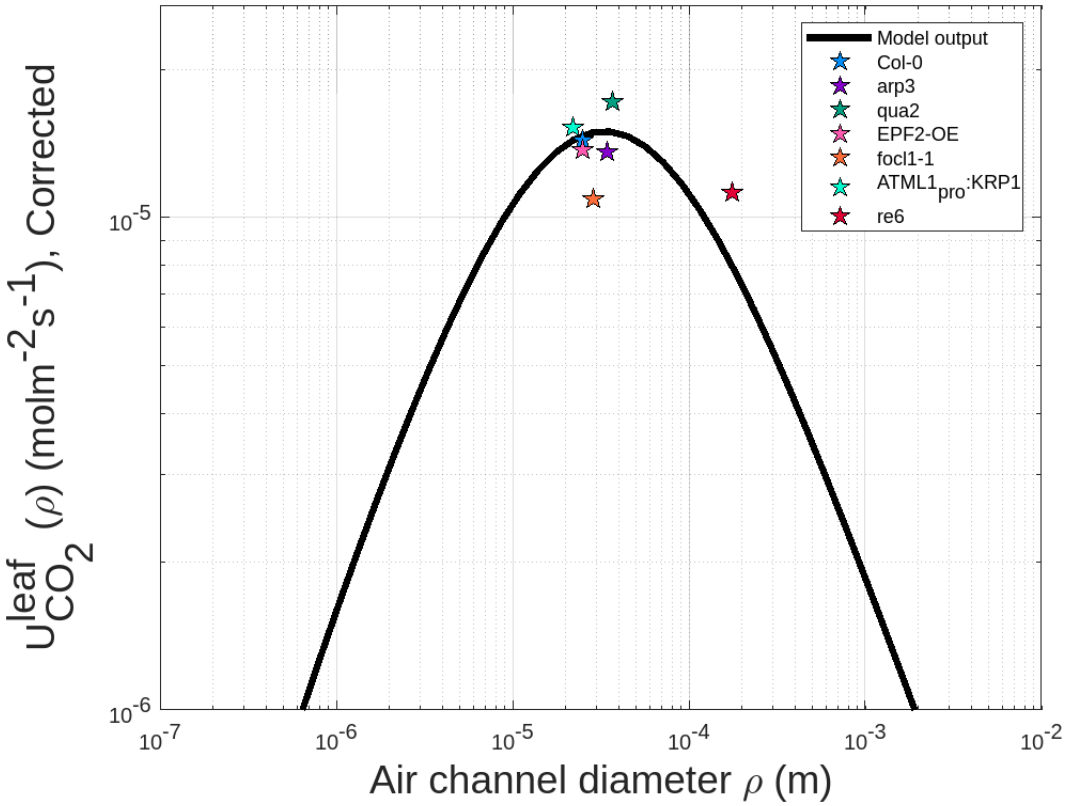

Figure 4.3: *Effective* CO_2 uptake rate as a function of air channel diameter ρ. The stars are markers of *measured* CO_2 assimilation rates with respect to air channel diameter for each mutant.

4.3 How does air channel depth affect CO_2 uptake?

While α can be thought of as a measure of how mutants deviate from the control line, Col-0, the current analysis does not reveal much about its physical significance in terms of its relationship with the mesophyll palisade structure. To investigate how the deviation factor α is related to the internal leaf structure, we compared it to our various structural parameters. We observed a strong, negative relationship between α and palisade air channel depth, L_z.

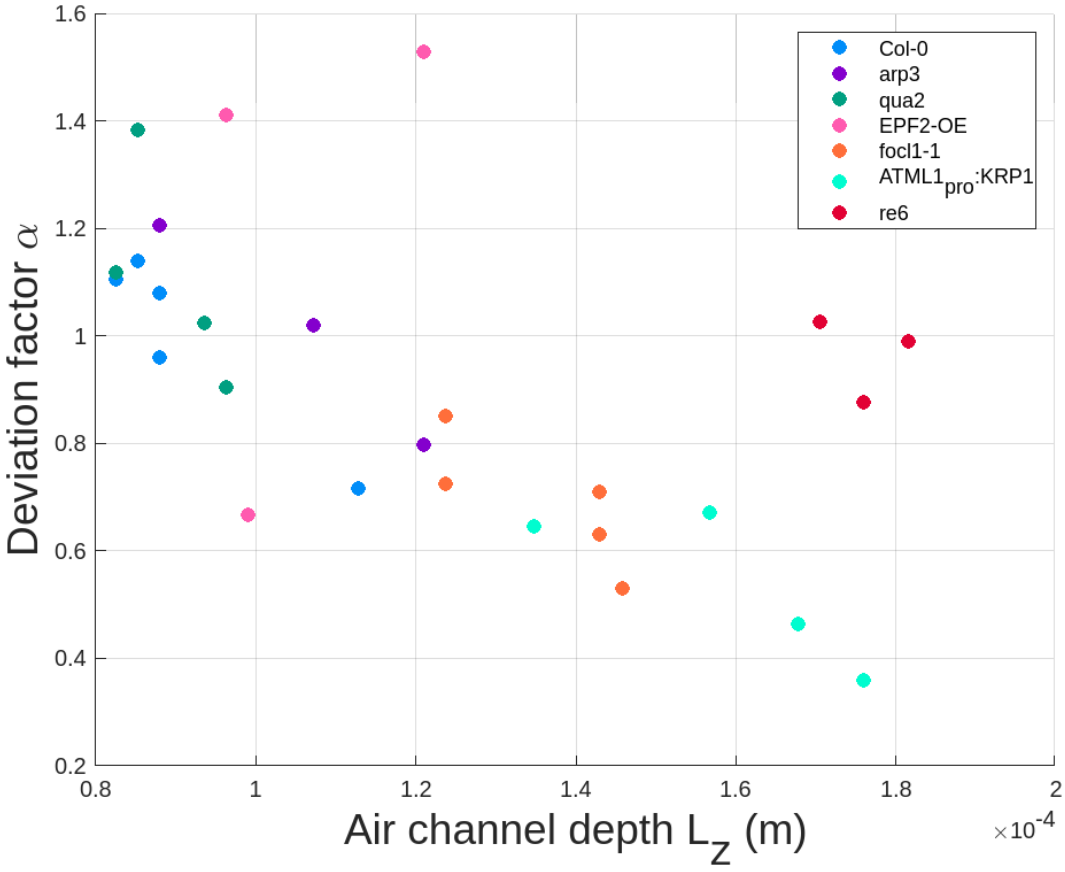

Figure 4.4: Deviation factor α against air channel depth L_z.

This observation suggests the the '*effective*' CO_2 uptake rate is a function of air channel depth, and leaves with shorter palisade air channels may be more efficient at photosynthetic conversion of CO_2 diffused from the air channels. This would imply a trend in which leaves with shorter diffusion pathways within the palisade

mesophyll are better at assimilating CO_2, which could suggest an optimisation of inner mesophyll structure. These results contrast the perhaps expected opposite results, where one might initially expect deeper air channels to uptake more CO_2 solely by virtue of having a larger volume.

We can consider prior work by Evans and Vogelmann [51], Vogelmann and Evans [162] and Borsuk and Brodersen [13] to try and make sense out of this. It is known that CO_2 fixation within the mesophyll cells is affected by light, essentially mediating chloroplast profiles through cell depth. Chloroplasts, the photosynthetic apparatus inside of mesophyll cells, will shift their position inside of the cells as a response to light, either moving towards the light source, or moving away from excess light in a process called photoprotection to prevent photoinhibition (stress caused by excess light, which can damage the leaf and reduce photosynthetic efficiency) [85]. A study by Gotoh et al. [63] showed that light-induced chloroplast movement was restricted for a thick leaved *Arabidopsis thaliana* mutant (the *angustifolia* mutant, specifically targeted to have a thick palisade layer), while for Col-0, light-induced movement of chloroplasts through the mesophyll was less restricted. The thick leaved mutant showed a higher chloroplast content per leaf area, which was the reason attributed to enhanced photosynthesis, but this mutation could be more expensive in terms of resource allocation and balancing, and past a certain thickness increase, the leaf could be seeing diminishing returns in terms of investment and photosynthetic yield, which is why the wild-type *Arabidopsis thaliana* is relatively thinner [69]. This would suggest that for a thinner or shorter palisade mesophyll, the light absorption profile, chloroplast concentrations and intercellular CO_2 concentration profiles might overlap better, leading to an 'easier' CO_2 uptake.

This brings us to the concept of sun and shade leaves, and the link between CO_2 assimilation and mesohyll depth, or thickness [147]. Sun leaves have been observed and modelled to be thicker (with a more columnar palisade mesophyll) [147] - being at the top of the plant, they have more readily access to the external resource that is light. It is therefore 'easier' for them to scatter light down a thicker palisade layer and into the spongy mesophyll layer, also allowing this lower to participate in photosynthesis. However, while an increased mesophyll thickness is accompanied with increased surface area available to chloroplasts facing air spaces, it is also accompanied by an increase in diffusional resistance (i.e., a decrease in conductance

as the pathways lengthen), and an increase in construction and maintenance costs of the leaf for the plant. Shade leaves, on the other hand, are larger in area but also thinner - this could be explained as an 'optimisation' attempt by the leaf in order to make better use of light, which is more limited for shade leaves. Shade leaves have been observed to use less chlorophyll to capture an equivalent amount of light for photosynthesis compared to sun leaves, with their CO_2 assimilation being best correlated to their palisade cell shape (i.e., depth) and chloroplast distribution, suggesting that their thinner palisade is an adaptation to maximise photosynthesis [86]. Temme et al. [146] also experimentally observed that thinner leaves tended to show improved mesophyll conductance to CO_2 (when grown under low CO_2), which would further support our own observations.

We can take the opportunity here to appreciate some unmodelled factors that may affect our observations, such as chloroplast size, density and movement (the latter of which we discussed). Zurzycki [186] postulated that chloroplast movement, when considered as a function of incident irradiance (irradiance falling directly on the leaf surface), maximised the use of limiting light for photosynthesis, and minimised damage caused by excess light to photosynthetic apparatus [111]. A study by Jeong et al. [79] demonstrated that a large population of smaller chloroplasts (the chloroplasts observed in wild-type *Arabidopsis thaliana* can be described as such) was better in terms of photosynthesis than having fewer, enlarged chloroplasts. A large group of smaller chloroplasts offered more surface area for the intercellular CO_2. In addition to this, a better performance was linked to the chloroplast stroma (the internal matrix of the chloroplast) thickness. The rearrangement of chloroplasts through the mesophyll was therefore better facilitated by many small chloroplasts than fewer, larger ones.

Other unmodelled traits that could be of interest are cell wall thickness & composition. Knauer et al. [84] observed that mesophyll conductance imposed a limit to photosynthesis, but no direct relationship was found between mesophyll conductance and RuBisCO content and 'true' carboxylation capacity of RuBisCO. It was instead suggested that the cell wall thickness was a factor affecting g_m [23, 49, 50, 158, 159, 178]. More specifically, differences in both the cell wall thickness and composition (hence, the cell wall porosity) were found to affect g_m, and ultimately, CO_2 assimilation [3, 44, 58].

4.4 Does the conductance coefficient vary with air channel depth?

The extensive evidence from literature, presented above, shows us that the situation at hand is incredibly complex, and also seems to suggest that photosynthetic traits such as mesophyll conductance g_m vary through the palisade mesophyll depth rather than acting as a constant value throughout the entire leaf. In our discussion, we laid out that chloroplasts moved through the mesophyll as a response to irradiance incident on the leaf surface.

There, we posit that mesophyll conductance g_m (upon which our conductance coefficient G_{CO_2} is dependent) varies proportionately to the surface area of chloroplasts exposed to the intercellular air spaces, the position of which is mediated by the leaf incident irradiance [49].

Aalto and Juurola [2], Kirschbaum [82], Lloyd et al. [91], Vogelmann and Martin [163], amongst others, showed that the light absorption profiles through the leaf mesophyll could be approximated by the Beer-Lambert law, which describes the attenuation of light with respect to the material it is travelling through [103]. We can use the form presented by Lloyd et al. [91], adapted to our nomenclature:

$$I = c_1 I_0 e^{-c_2 z / L_{leaf}} \quad , \tag{4.4}$$

where:

- I_0 is the incident irradiance (photon irradiance on the leaf surface) (mol quanta $m^{-2}\,s^{-1}$),
- c_1 is a constant that can take on values greater than 1 to account for internal scattering effects near the adaxial surface (upper surface),
- c_2 is a constant describing the rate of exponential decay,
- z is the distance from the surface of the leaf (m),
- L_{leaf} is leaf thickness (m).

c_1 was experimentally estimated to be around 1.1 for the light intensity in the palisade layer to remain high, while the attenuation (or extinction) coefficient c_2

was fitted at a value of 2.4, both of which we will use in Fig. 4.5 below. The incident irradiance was fitted to a saturating value of 1500 mol quanta m^{-2} s^{-1}, taken from Aalto and Juurola [2]. They, along with Evans [48], remarked that the palisade layer may minimise scattering effects and 'guide' light to the spongy mesophyll through collimation, where large scattering effects may enhance light capture. This may imply a more uniform profile than the one presented by the Beer-Lambert law, but we will not be taking this case into account for our analysis.

Borsuk and Brodersen [13] also showed that the chlorophyll content through the mesophyll depth could be estimated through a simple quadratic equation. Using hierarchical clustering on a range of collected data for several species, they identified the presence of several clusters of species that shared similar concentration profiles, and assigned different numerical coefficients for the quadratic expression of each cluster - we will be using the values assigned to the cluster *Arabidopsis thaliana* is found in. Fig. 4.5 shows the fitted Beer-Lambert law and the Borsuk-Brodersen chlorophyll concentration equation overlaid.

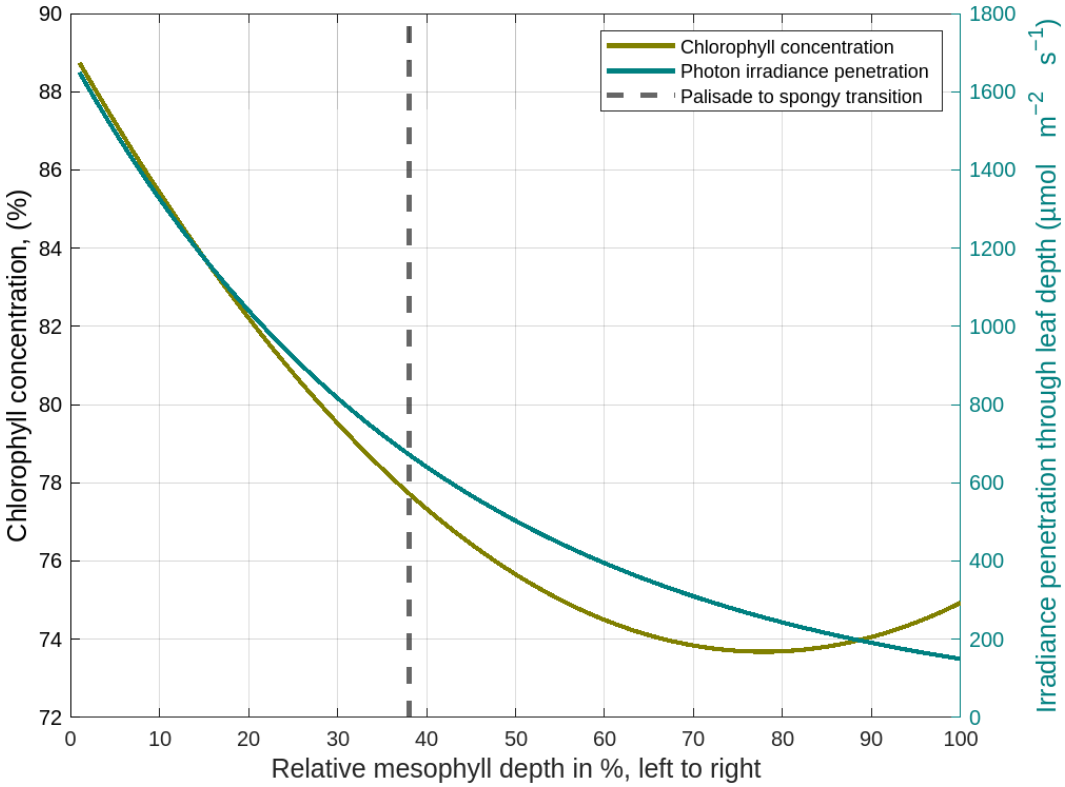

Figure 4.5: Chlorophyll concentration and light absorption profiles with respect to mesophyll depth.

Fig. 4.5 also includes a reference line to indicate the transition from palisade to spongy within the mesophyll.

While both chloroplastic distribution and light absorption are well aligned to each other and seem like promising avenues, mathematically describing their combined mechanistic effects isn't as simple as just adding or multiplying both expressions into our governing equation. Indeed, the situation is more complex than this. Rather than haphazardly guessing a model structure that holds little to no mechanistic basis, let us instead prescribe an arbitrary polynomial with sufficient degrees of freedom for $G_{CO_2}(z)$, and then brute force a parameter search over the values of the coefficients that minimise the error. The resulting shape of $G_{CO_2}(z)$ might then guide us towards a physical explanation for the profile (i.e., the combined behaviour of light and chlorophyll).

$$G_{CO_2}(z) = w_1 + w_2 z + w_3 z^2 + w_4 z^3 + \dots, \tag{4.5}$$

where $w_1, w_2, w_3 \dots$ are the polynomial coefficients to be determined.

Given a variable expression for G_{CO_2} (4.5), an exhaustive Leave-One-Out (L-O-O) Cross Validation grid search method can be designed determine the weights $w_1, w_2, \dots$ that gives the minimum mean squared error between the modelled output and the equivalent measured value, as described by the algorithm below. Note that with a varying $G_{CO_2}(z)$ instead of a constant G_{CO_2}, this turns our model of $U_{CO_2}^{leaf}$ into a semi-analytical expression - solving it analytically returns a solution in the form of Airy functions or modified Bessel functions, which are hard to interpret physically and tell us nothing meaningful about the new model behaviour. We instead opt to solve the model numerically through a finite-difference method, as shown in the algorithm below.

As the exhaustive grid search is very computationally expensive, a smaller subset of our collected *Arabidopsis thaliana* data is used to test this algorithm (n=3 for Col-0, *arp3*, *qua2*, *EPF2-OE* each).

Algorithm 4.1 L-O-O CV Grid search for polynomial coefficients of $G_{CO_2}(z)$

Result: Finding 'best' set of weight values (using min squared error)
Define constants (e.g., array of air channel diameters ρ, L_z etc.)
e.g., $\rho = \begin{bmatrix} \underbrace{\rho_1\ \rho_2\ \rho_3}_{\text{mutant 1}} & \rho_4 & \rho_5 & \rho_6 & \cdots & \rho_i \end{bmatrix}$
Define weight vector, e.g., $\mathbf{W} = \begin{bmatrix} W_1 & W_2 \& \ldots W_j \end{bmatrix}$

for $k = 1 \cdots$ length(ρ *vector)* **do**
  for $l = 1 \cdots$ length(W *vector)* **do**
    Nest an extra for loop here for every additional weight coefficient
    Set up finite difference matrices (inner for loop process because of varying L_z's)
    Solve for CO_2 uptake U by integrating numerically
  end
end
This results in a matrix of modelled uptake values for all mutants and weight values: $U = \begin{bmatrix} U^{\rho_1,W_1} & U^{\rho_1,W_2} & \ldots & U^{\rho_1,W_j} \\ U^{\rho_2,W_1} & U^{\rho_2,W_2} & \ldots & U^{\rho_2,W_j} \\ \vdots & \vdots & \ddots & \vdots \\ U^{\rho_i,W_1} & U^{\rho_i,W_2} & \ldots & U^{\rho_i,W_j} \end{bmatrix}$
Calculate squared error matrix SqErr$= |A_{400} - U|^2$

Leave one out procedure takes place here:
for *exclude_idx* $= 1 \cdots$ length(ρ *vector)* **do**
  desired_idx = [1:(exclude_idx -1), (exclude_idx+1):length(ρ vector)] (This process excludes a sample row-wise)
  desired_err = SqErr(desired_idx, :)
  J(exclude_idx) = sum(desired_err,1)
end
The process above is a cost function to minimise the error: i.e., $\rightarrow$ Cost function $J_M(j, k, l, \ldots) = \sum_{i \neq M} E(j, k, l, \ldots)$
Best weights, $W_M^* = \text{argmin}_{j,k,l,\ldots} J_M(j, k, l, \ldots)$
Re-predict CO_2 uptake using best Ws per sample
Calculate new $\hat{G}$ and mean squared error of model performance with respect to measured values.

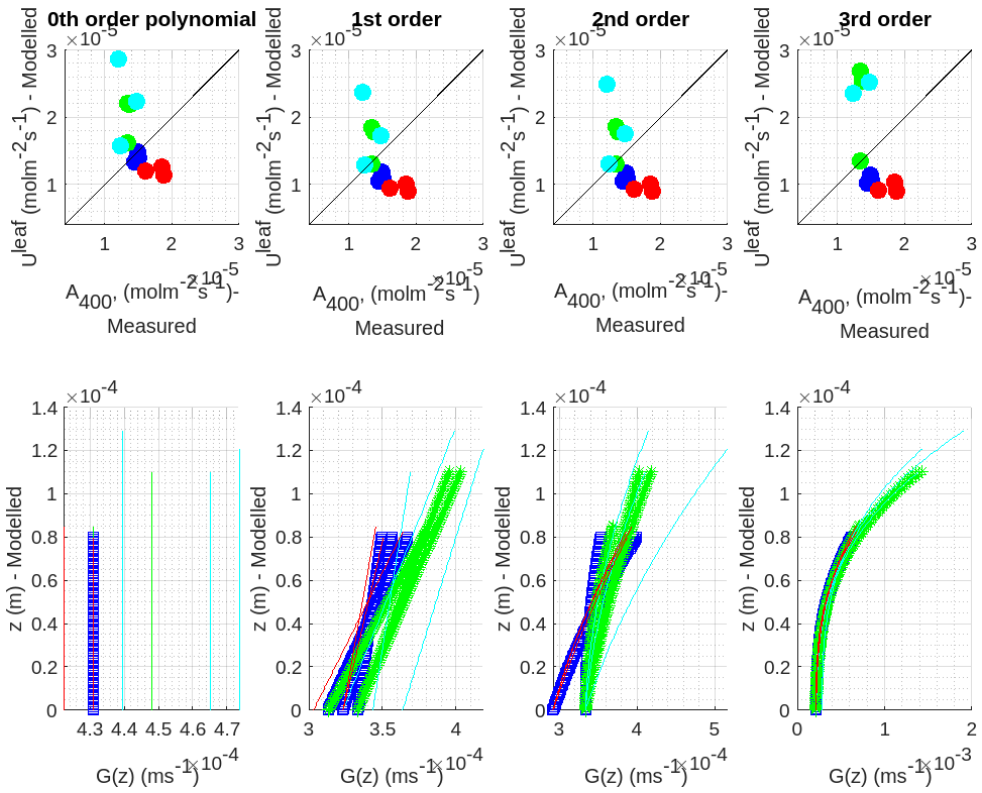

Figure 4.6: Grid search method result for increasing polynomial orders.

The grid search method turned out to get increasingly computationally expensive, with the search resolution getting worse as the dimensionality increased, mostly owing to the space between each data point increasing as the number of dimensions increased, causing the higher dimensional search spaces to be rather sparse despite having more points than the lower ones (the curse of dimensionality!). The polynomial coefficient search space was restricted to positive values for this search in an attempt to preserve an acceptable resolution - however, given more computational resources, the search should most definitely include negative coefficient values in the space too, as these would provide a greater search space area. The result shown in Figure 4.6 is rather poor, as one would expect the spread of predicted $U^{leaf}_{CO_2}$ values in the upper graphs to reduce as the polynomial order increased. However, we instead do not observe a decrease an error, leading us to believe that the resolution of the search space is either too coarse. We therefore ran the algorithm again, but with a search space containing twice as many points across *each* dimension, leading to much more possible points in the higher order search spaces.

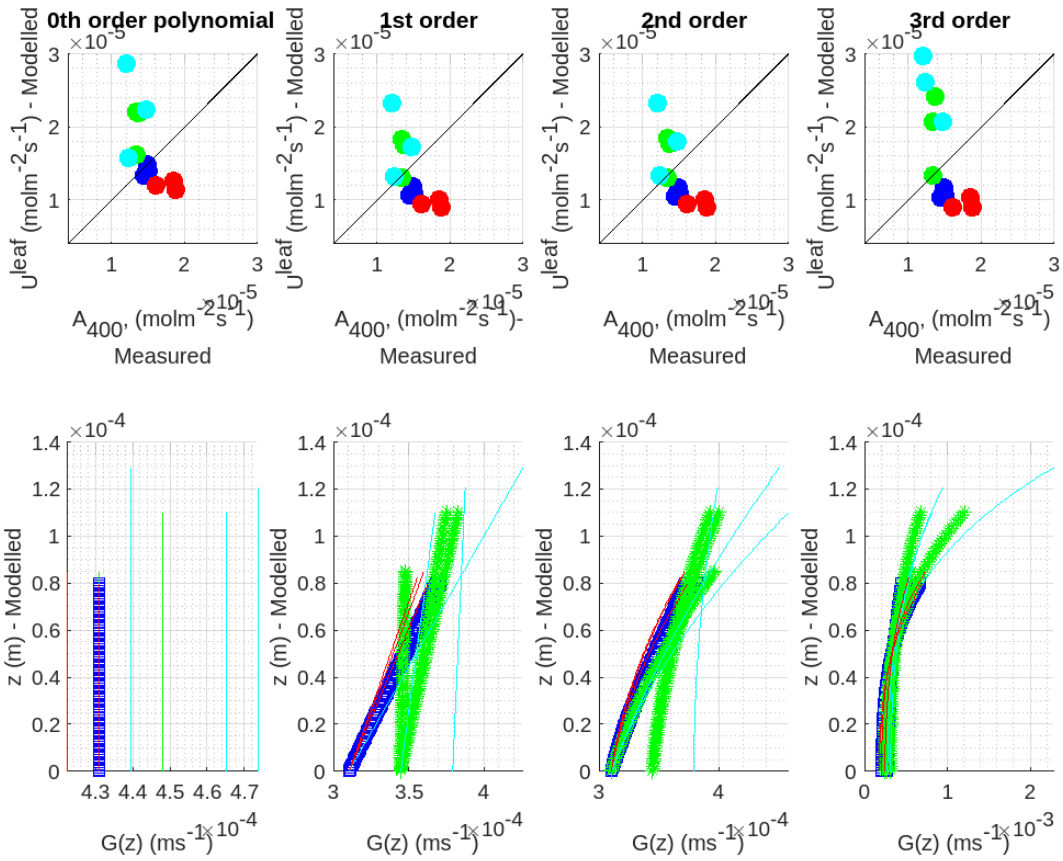

Figure 4.7: Grid search method result for increasing polynomial orders, over a search space twice as dense as the previous run.

The result however, was much of the same, with the exhaustive seach algorithm once more not reducing the spread of predicitions (and hence the prediction error) as the order increased. As seen above, exhaustive grid searches do not scale up particular well to higher dimensional spaces (over 2D). In particular, running exhaustive grid searches over finer resolutions as the dimensions increase turned out to be prohibitively expensive.

Random search methods, on the other hand, are well adapted for our model formulation here, and should cost a fraction of the computational cost of the exhaustive grid search method, while also providing a better coverage of the search space [8]. Here, we opt for a guided random search method: the genetic algorithm.

Genetic Algorithms (GA) have been around since the 1970s and are a type of numerical optimiser which is based upon the idea of biological evolution and

survival of the fittest. Genetic algorithms operate on a string structure (set of parameters) which are evolved over time. In general they are comprised of a number of steps including, but not limited to, crossover, recombination, mutation and selection. These steps allow for information to be passed on from parents to offspring while also allowing for additional changes to take place. They initiate its search from a population of points rather than a single one. Genetic algorithms have several advantages including the ability to deal with complex problems and parallelism [140].

We can therefore design a L-O-O cross-validated GA method to search for polynomial coefficient values of $G_{CO_2}(z)$ that would best fit our model. The datasets are separated into n folds of training and validation sets using a L-O-O approach, and then run through a standard GA with the following settings

The fitness function for the GA method can be defined as:

$$j = \text{argmin} \sum \Big(|\text{Measured } CO_2 \text{ assimilation rate} - \text{Modelled } CO_2 \text{ uptake rate}| \Big). \tag{4.6}$$

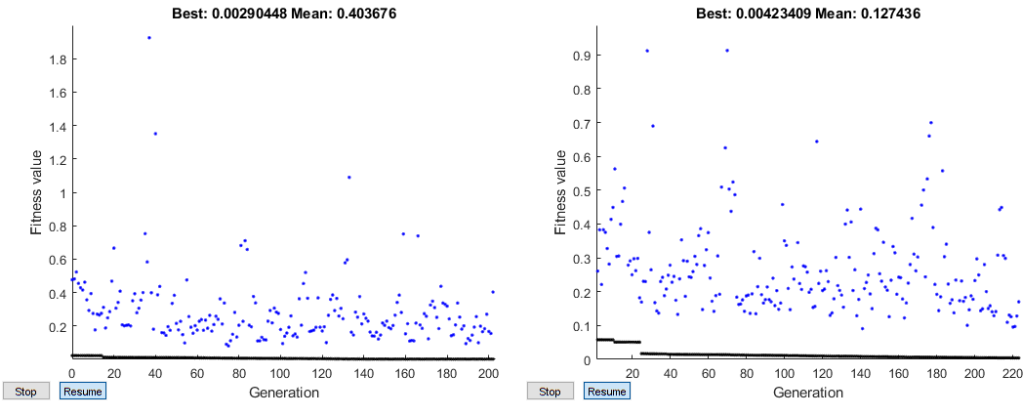

Figure 4.8: Two separate genetic algorithm runs, both failing to converge.

The GA results above show that while the fitness function does slightly converge initially, as the generations progress, it does not converge to a set of similar solutions over the various datasets, therefore not predicting a set pattern or behaviour in $G_{CO_2}(z)$, with a large number of oscillations between the mean and best values, which suggests that the model is not being correctly fitted. Two possible explanations are that the GA method is unable to predict a trend, or that the

model is incapable of predicting any underlying behaviour we might expect from $G_{CO_2}(z)$.

We demonstrated that there was a strong relationship between air channel depth L_z, CO_2 uptake rate and CO_2 conductance coefficient G_{CO_2}. An appreciation was made about G_{CO_2} being highly like to vary with air channel depth as a response to factors such as light irradiance and palisade chlorophyll distribution. However, instead of guessing a potentially incorrect expression involving these two, we opted to represent $GCO_2(z)$ as a polynomial expression, with the intent to solve our model with a now variable conductance coefficient using our paired structural measurements and $A - C_i$ gas exchange data.

Both an exhaustive grid search method and a random search method (genetic algorithm) failed to provide a consistent pattern or behaviour for a $G_{CO_2}(z)$ that varied with air channel depth, even when explored with increasing degrees of freedom in the polynomial expression. This potentially implies three scenarios: either the model is missing some key parameters/variables, some other current parameters should be explored as now being variables (to channel depth L_z, for instance), or this behaviour simply cannot be modelled using the type of $A - C_i$ data we have collected.

We suggest repeating this experiment by collecting data from *Arabidopsis thaliana* mutant lines with documented changes to the mesophyll thickness, such as the *angustifolia* line with increased mesophyll thickness [63, 81], or with mutants that have been engineered to have different chloroplast behaviour, density or size, for instance fewer, enlarged chloroplasts, like the *arc* line [167], with more detailed measurements of cell wall structural properties and chloroplast size, density and location recorded. This may then allow us to shed some more light on the observation in Fig. 4.3, and more clearly formulate the relationship between palisade mesophyll structure, CO_2 uptake, CO_2 assimilation and mesophyll conductance.

Chapter 5

A Modelling Framework for Water Loss in the Palisade Mesophyll Air Channel

5.1 Motivation

CO_2 enters the leaf through the leaf's pores (stomata), where it diffuses through the intercellular air channels. where it is uptaken the cells for CO_2 assimilation. As this pathway connects the inner leaf to the atmosphere, the leaf also loses water from its cells, into the air channels and to the outside of the leaf in the form of water vapour, through a process known as transpiration [126]. The leaf therefore acts both as a CO_2 sink and a H_2O source [42]. As the leaf transpires, the plant ensures a continuous flow of water through its internal hydraulic system to replace this loss. This clearly indicates a shared pathway through the leaf mesophyll air channels for both CO_2 and water vapour.

In addition to this, if plants lose water in excess (i.e., they experience water stress), both structural and physiological components of the leaf will become affected. Water loss can lead to a loss of turgor pressure (the water pressure within the cell that helps it maintain its shape), which directly influences cell shape and

leaf porosity, therefore altering the amount of intercellular surface area available for CO_2 uptake [131, 132]. This has also been documented to affect mesophyll conductance, as its individual pathways, such as cell wall thickness and permeability, also suffer as a consequence [179]. Water-related changes to the structure and physiology also affect hydraulic parameters, such as the leaf hydraulic conductance - defined as a measure of the ratio of water flow rate and water potential gradient across the leaf (not a direct equivalent to mesophyll conductance, but the principle of similitude may be applied here) [57].

To conclude, photosynthetic traits such as CO_2 assimilation and mesophyll conductance, hydraulic traits such as transpiration and leaf hydraulic conductance & leaf structure have been documented to be related, either through a coordination of CO_2 gas exchange and hydraulic flow, or through the structure constraining photosynthetic and hydraulic function [31, 57, 105, 115, 152, 179]. However, underpinning this relationship at a local scale (e.g., at the mesophyll scale) remains challenging, as directly measuring hydraulic behaviour at such a scale proves to be non-trivial and is technically challenging [75, 171]. However, with measurements of individual mesophyll air channels quantifying the leaf mesophyll structure, paired with gas exchange measurements, and theoretical knowledge of water vapour loss, is it possible to investigate the relationship between palisade mesophyll structure, CO_2 uptake and water vapour loss? We will set out to achieve this objective in this chapter.

5.2 Water loss model

Before diving into modelling a water loss model, let us re-iterate that assumptions made for the CO_2 uptake modelling process hold here as well. An expression for the concentration of water vapour within the palisade air channel can be obtained in a similar fashion to the CO_2 concentration equation (3.10) seem in Chapter 3. However, we must first revisit the diffusion-driven equation (3.5a). By considering Fick's second law of diffusion, we can represent (3.5a) as a time-varying expression:

$$\frac{\partial \phi_{CO_2}(z,t)}{\partial t} = D_{CO_2}\frac{\partial^2 \phi_{CO_2}(z,t)}{\partial z^2} - \frac{4G_{CO_2}}{\rho}\phi_{CO_2}(z,t). \tag{5.1}$$

Equation (5.1) contains a sink term for the CO_2 conductance. Here, we can instead introduce a source term $\phi^{cell}_{H_2O}$ (the concentration of water inside cells surrounding the air channel) to assume an equivalent expression for water vapour loss. Since cells are primarily made up of water, we choose to parameterise this source term as being equal to the molar volume of water at 25 °C at atmospheric pressure [25]. This is given as 18.07 $cm^3\,mol^{-1}$, which equals to 5.54×10^4 $mol\,m^{-3}$ to match our modelling framework [161]. Note that $\phi^{cell}_{H_2O}$ is a constant.

$$\frac{\partial\phi_{H_2O}(z,t)}{\partial t} = D_{H_2O}\frac{\partial^2\phi_{H_2O}(z,t)}{\partial z^2} + \frac{4G_{H_2O}}{\rho}\left(\phi^{cell}_{H_2O} - \phi_{H_2O}(z,t)\right), \tag{5.2a}$$

with given boundary conditions:

$$z = 0, \phi_{H_2O}(0) = \phi_{H_2O,0}, \tag{5.2b}$$

$$z = L_z, \phi_{H_2O}(L_z) = \phi_{H_2O,L_z}. \tag{5.2c}$$

In the steady-state, (5.2a) simplifies to a second order boundary-value *non-homogeneous* differential equation with a source term:

$$\frac{d^2\phi_{H_2O}(z)}{dz^2} = \frac{\lambda^2}{\rho}\left(\phi_{H_2O}(z) - \phi^{cell}_{H_2O}\right); \quad \lambda = \sqrt{4G_{H_2O}/D_{H_2O}}, \tag{5.3}$$

where G_{H_2O} is the conductance coefficient of water content from the cells into the airspace, and D_{H_2O} is the diffusion coefficient of water vapour. Both of these will be parameterised with values taken from literature in the next section.

As (5.3) is a *non-homogeneous* differential equation, we cannot simply assume a general solution for $\phi_{H_2O}(z)$. Instead, the method of undetermined coefficients must be used. To find the general solution to the non-homogeneous equation (5.3), let us consider its associated *homogeneous* equation first:

$$\frac{d^2\phi_{H_2O}(z)}{dz^2} - \frac{\lambda^2}{\rho}\phi_{H_2O}(z) = 0, \tag{5.4}$$

also known as the complimentary equation to (5.3).

From Chapter 3, we know that the general solution to the complimentary equation (5.4) should be of the form:

$$\phi_{H_2O,\mathcal{C}}(z) = ae^{\frac{\lambda}{\sqrt{\rho}}z} + be^{-\frac{\lambda}{\sqrt{\rho}}z}. \tag{5.5}$$

Let $\phi_{\mathcal{PS}}(z) = \mathcal{P}$ be any particular solution to the non-homogeneous equation (5.3). The general solution of (5.3) then takes the form:

$$\phi_{H_2O,g} = \phi_{H_2O,\mathcal{C}}(z) + \phi_{\mathcal{PS}(z)}. \tag{5.6}$$

As the source term is a constant, let us assume that $\mathcal{P}$ is a constant as well. As such, the second-order derivative of $\phi_{\mathcal{PS}}(z)$, $\frac{d^2}{dz^2}(\phi_{\mathcal{PS}}) = 0$. This, along with $\phi_{\mathcal{PS}} = \mathcal{P}$, are substituted back into (5.3):

$$\begin{aligned} \frac{d^2\phi_{\mathcal{PS}}}{dz^2} &= \frac{\lambda^2}{\rho}\phi_{\mathcal{PS}}(z) - \frac{\lambda^2}{\rho}\phi^{cell}_{H_2O}, \\ -\frac{\lambda^2}{\rho}\phi_{\mathcal{PS}}(z) &= -\frac{\lambda^2}{\rho}\phi^{cell}_{H_2O}, \\ \phi_{\mathcal{PS}}(z) &= \phi^{cell}_{H_2O}, \\ \implies \mathcal{P} &= \phi^{cell}_{H_2O}. \end{aligned} \tag{5.7}$$

The general solution of the non-homogeneous equation (5.3) is then:

$$\phi_{H_2O}(z) = Ae^{\frac{\lambda}{\sqrt{\rho}}z} + Be^{-\frac{\lambda}{\sqrt{\rho}}z} + \phi^{cell}_{H_2O}. \tag{5.8}$$

Since the solution for the CO_2 uptake rate model takes a hyperbolic form, we can also convert (5.8) to a hyperbolic general solution for consistency:

$$\begin{aligned} \phi_{H_2O}(z) &= A\left[\cosh\left(\frac{\lambda}{\sqrt{\rho}}z\right) + \sinh\left(\frac{\lambda}{\sqrt{\rho}}z\right)\right] + B\left[\cosh\left(\frac{\lambda}{\sqrt{\rho}}z\right) - \sinh\left(\frac{\lambda}{\sqrt{\rho}}z\right)\right] + \phi^{cell}_{H_2O}, \\ &= \alpha\cosh\left(\frac{\lambda}{\sqrt{\rho}}z\right) + \beta\sinh\left(\frac{\lambda}{\sqrt{\rho}}z\right) + \phi^{cell}_{H_2O}. \end{aligned} \tag{5.9}$$

Use boundary conditions (5.2b, 5.2c) to fix the coefficients $\alpha, \beta \in \mathbb{R}$:

$$\begin{aligned} \phi_{H_2O}(0) &= \alpha\cosh(0) + \beta\sinh(0) + \phi^{cell}_{H_2O}, \\ \implies \alpha &= \phi_{H_2O}(0) - \phi^{cell}_{H_2O}. \end{aligned} \tag{5.10}$$

$$\phi_{H_2O}(L_z) = \alpha \cosh\left(\frac{\lambda}{\sqrt{\rho}} L_z\right) + \beta \sinh\left(\frac{\lambda}{\sqrt{\rho}} L_z\right) + \phi_{H_2O}^{cell}. \tag{5.11}$$

Substitute (5.11) into (5.10):

$$\begin{aligned}
\phi_{H_2O}(L_z) &= \left(\phi_{H_2O}(0) - \phi_{H_2O}^{cell}\right) \cosh\left(\frac{\lambda}{\sqrt{\rho}} L_z\right) + \beta \sinh\left(\frac{\lambda}{\sqrt{\rho}} L_z\right) + \phi_{H_2O}^{cell}, \\
\beta \sinh\left(\frac{\lambda}{\sqrt{\rho}} L_z\right) &= \phi_{H_2O}(L_z) - \left(\phi_{H_2O}(0) - \phi_{H_2O}^{cell}\right) \cosh\left(\frac{\lambda}{\sqrt{\rho}} L_z\right) - \phi_{H_2O}^{cell}, \\
\implies \beta &= \frac{\phi_{H_2O}(L_z) - \left(\phi_{H_2O}(0) - \phi_{H_2O}^{cell}\right) \cosh\left(\frac{\lambda}{\sqrt{\rho}} L_z\right) - \phi_c}{\sinh\left(\frac{\lambda}{\sqrt{\rho}} L_z\right)}.
\end{aligned} \tag{5.12}$$

Coeffs. α and β can be substituted in the general solution of hyperbolic form (5.9):

$$\begin{aligned}
\phi_{H_2O}(z) &= \left(\phi_{H_2O}(0) - \phi_{H_2O}^{cell}\right) \cosh\left(\frac{\kappa}{\sqrt{\rho}} z\right) + \cdots \\
&\cdots \left(\frac{\phi_{H_2O}(L_z) - \left(\phi_{H_2O}(0) - \phi_{H_2O}^{cell}\right) \cosh\left(\frac{\kappa}{\sqrt{\rho}} L_z\right) - \phi_{H_2O}^{cell}}{\sinh\left(\frac{\kappa}{\sqrt{\rho}} L_z\right)}\right) \sinh\left(\frac{\kappa}{\sqrt{\rho}} z\right) + \phi_{H_2O}^{cell} \\
&= \frac{\left(\phi_{H_2O}(0) - \phi_{H_2O}^{cell}\right) \cosh\left(\frac{\kappa}{\sqrt{\rho}} z\right)}{\sinh\left(\frac{\kappa}{\sqrt{\rho}} L_z\right)} + \frac{\phi_{H_2O}(L_z) \sinh\left(\frac{\kappa}{\sqrt{\rho}} z\right)}{\sinh\left(\frac{\kappa}{\sqrt{\rho}} L_z\right)} - \cdots \\
&\cdots \frac{\left(\phi_{H_2O}(0) - \phi_{H_2O}^{cell}\right) \cosh\left(\frac{\kappa}{\sqrt{\rho}} L_z\right) \sinh\left(\frac{\kappa}{\sqrt{\rho}} z\right)}{\sinh\left(\frac{\kappa}{\sqrt{\rho}} L_z\right)} - \frac{\phi_{H_2O}^{cell} \sinh\left(\frac{\kappa}{\sqrt{\rho}} z\right)}{\sinh\left(\frac{\kappa}{\sqrt{\rho}} L_z\right)} + \frac{\phi_{H_2O}^{cell} \sinh(\frac{\kappa}{\sqrt{\rho}} L_z)}{\sinh\left(\frac{\kappa}{\sqrt{\rho}} L_z\right)}.
\end{aligned} \tag{5.13}$$

Simplify using hyperbolic identities:

$$\begin{aligned}
\phi_{H_2O}(z) &= \frac{\left(\phi_{H_2O}(L_z) - \phi_{H_2O}^{cell}\right) \sinh\left(\frac{\kappa}{\sqrt{\rho}} z\right)}{\sinh\left(\frac{\kappa}{\sqrt{\rho}} L_z\right)} + \cdots \\
&\cdots + \frac{\left(\phi_{H_2O}(0) - \phi_{H_2O}^{cell}\right) \sinh\left(\frac{\kappa}{\sqrt{\rho}} (L_z - z)\right) + \phi_{H_2O}^{cell} \sinh\left(\frac{\kappa}{\sqrt{\rho}} L_z\right)}{\sinh\left(\frac{\kappa}{\sqrt{\rho}} L_z\right)}.
\end{aligned} \tag{5.14}$$

Evaluating LHS of (5.3) using (5.14) yields:

$$\begin{aligned}
&\frac{d^2\phi_{H_2O}(z)}{dz^2} = \\
&\frac{d}{dz}\left[\frac{\left(\phi_{H_2O}(L_z)-\phi^{cell}_{H_2O}\right)\left(\frac{\kappa}{\sqrt{\rho}}\right)\cosh\left(\frac{\kappa}{\sqrt{\rho}}z\right)-\left(\phi_{H_2O}(0)-\phi^{cell}_{H_2O}\right)\left(\frac{\kappa}{\sqrt{\rho}}\right)\cosh\left(\frac{\kappa}{\sqrt{\rho}}(L_z-z)\right)}{\sinh\left(\frac{\kappa}{\sqrt{\rho}}L_z\right)}\right] \\
&= \frac{\left(\phi_{H_2O}(L_z)-\phi^{cell}_{H_2O}\right)\left(\frac{\kappa^2}{\rho}\right)\sinh\left(\frac{\kappa}{\sqrt{\rho}}z\right)-\left(\phi_{H_2O}(0)-\phi^{cell}_{H_2O}\right)\left(\frac{\kappa^2}{\rho}\right)\sinh\left(\frac{\kappa}{\sqrt{\rho}}(L_z-z)\right)}{\sinh\left(\frac{\kappa}{\sqrt{\rho}}L_z\right)}.
\end{aligned} \tag{5.15}$$

We remind the reader that both $\phi^{cell}_{H_2O}$ and $\frac{\kappa}{\sqrt{\rho}}L_z$ are both constants. Therefore, the pooled parameter $\frac{\phi^{cell}_{H_2O}\sinh\left(\frac{\kappa}{\sqrt{\rho}}L_z\right)}{\sinh\left(\frac{\kappa}{\sqrt{\rho}}L_z\right)}$ is also a constant, and goes to zero when $\phi_{H_2O}(z)$ is differentiated. The constant of integration that appears by integrating it back is equal to the constant that gets cancelled out, proving this solution is correct.

We can continue by using the same approach taken to obtain the CO_2 uptake model here. In order to model *water loss rate* from the cell into the air channel, termed as $\Gamma_{H_2O}(z)$, we can integrate the water loss with respect to air channel depth:

$$\begin{aligned}
\Gamma_{H_2O} &= \int_0^{L_z}\left(\pi\rho G_{H_2O}\phi_{H_2O}(z)\Delta z\right), \\
&= \pi\rho G_{H_2O}\int_0^{L_z}\phi_{H_2O}(z)dz.
\end{aligned} \tag{5.16}$$

$$\begin{aligned}
\Gamma_{H_2O}(z) = \pi\rho G_{H_2O}\int_0^{L_z}&\frac{\left(\phi_{H_2O}(L_z)-\phi^{cell}_{H_2O}\right)\sinh\left(\frac{\lambda}{\sqrt{\rho}}z\right)}{\sinh\left(\frac{\lambda}{\sqrt{\rho}}L_z\right)}+\cdots \\
\cdots+&\frac{\left(\phi_{H_2O}(0)-\phi^{cell}_{H_2O}\right)\sinh\left(\frac{\kappa}{\sqrt{\rho}}(L_z-z)\right)+\phi^{cell}_{H_2O}\sinh\left(\frac{\kappa}{\sqrt{\rho}}L_z\right)}{\sinh\left(\frac{\kappa}{\sqrt{\rho}}L_z\right)}dz.
\end{aligned} \tag{5.17}$$

Since the denominator is a constant, this can be broken down into 3 simpler integrations and solved to obtain the following:

$$\begin{aligned}\Gamma_{H_2O} &= \left[\frac{\pi\rho G_{H_2O}}{\sinh\left(\frac{\kappa}{\sqrt{\rho}}L_z\right)}\right] \times \left[\left(\frac{\sqrt{\rho}}{\kappa}\right)\left(\phi_{H_2O}(L_z)+\phi_{H_2O}(0)-2\phi^{cell}_{H_2O}\right)\left(\cosh\left(\frac{\kappa}{\sqrt{\rho}}L_z\right)-1\right)+\cdots\right.\\ &\left.\cdots+L_z\phi^{cell}_{H_2O}\sinh\left(\frac{\kappa}{\sqrt{\rho}}L_z\right)\right]\\ &=(\frac{\pi\rho^{3/2}G_{H_2O}}{\kappa})(\phi_{H_2O}(L_z)+\phi_{H_2O}(0)-2\phi^{cell}_{H_2O})\left[\coth\left(\frac{\kappa}{\sqrt{\rho}}L_z\right)-\operatorname{csch}\left(\frac{\kappa}{\sqrt{\rho}}L_z\right)\right]+\cdots\\ &\cdots+\pi\rho L_z\phi^{cell}_{H_2O}G_{H_2O}.\end{aligned} \tag{5.18}$$

The model can be formally verified by applying the fundamental theorem of calculus on the indefinite integral $\int \phi_{H_2O}(z)dz$, which simply results in $\phi_{H_2O}(z)$. In our case, the process was verified through a symbolic computation using Maple [98].

Just as seen with the CO_2 uptake model, this H_2O model can also be extended for N air channels normalised over the ROI area L_x^2:

$$\Gamma^{leaf}_{H_2O} = \frac{N}{L_x^2}\times\Gamma_{H_2O}(z) = \frac{\Gamma_{H_2O}(z)}{(\rho+d)^2}. \tag{5.19}$$

5.3 The leaf's dilemma - CO_2 or H_2O?

In order to get a better understanding of the leaf hydraulic situation, let us parameterise (5.14), the expression for intercellular water vapour concentration with respect to air channel depth, and (5.19), the water loss rate model per leaf area. For any structural parameters, such as air channel diameter, cellular thickness, and air channel depth, we will use the averaged recorded Col-0 values from our own data.

As covered earlier, the measurement of intercellular air channel water vapour concentrations is non-trivial [99, 171] and we do not possess such measurements in our datasets - our data sources focused on gas exchange measurements, and hydraulic parameters are better captured through different specialist equipment

such as pressure chambers. However, a good approximation for the water vapour concentrations at the boundary conditions (top and bottom of the air channel), $\phi_{H_2O}(0)$ and $\phi_{H_2O}(L_z)$, can be taken as the sampled water vapour concentration recorded in the LICOR chamber from Col-0 samples. Therefore, as we previously assumed amphistomatic behaviour, $\phi_{H_2O}(0) = \phi_{H_2O}(L_z) = 12$ mmol mol^{-1}, which, as a molar volume, is 0.49 mol/m^3.

An extra parameter which will be of interest for the model analysis is the water vapour concentration inside the leaf at saturation. Here, we will borrow a measurement of 35 mmol mol^{-1} from Wong et al. [171], which was measured for cotton (*Gossypium hirsutum L.*) at approximately 25 °C. This parameter is not directly incorporated in the model, but will give us an indication on the water vapour saturation situation inside the air channel.

Next, we need to parameterise G_{H_2O}. This is a difficult situation, as G_{H_2O} is directly analogous to G_{CO_2}, which we derived and fitted from a combination of g_m, the mesophyll conductance to CO_2 and gas exchange data, but there is no *direct* equivalent to mesophyll conductance [57]. However the closest equivalent would be the leaf hydraulic conductance, K_{leaf}, which we described earlier. Measurements of K_{leaf} for intact leaves of Col-0 are available from Grunwald et al. [65], taken as 35 mmol m^{-2} s^{-1} MPa^{-1} at 22 °C. This needs to be adjusted to 25 °C to match our modelling setting. An empirical formula from Sack and Scoffoni [127] can be used:

$$K_{leaf}(25^\circ C) = \frac{K_{leaf}(t)}{\left(0.88862 \times \left(\frac{1}{10^{(1.3272\times(20-t)-0.001053\times(t-20)^2/(t+105))}}\right)\right)}, \quad (5.20)$$

where t is leaf temperature. Then, the Woodward unit conversion [172] can be used to get G_{H_2O}:

$$G_{H_2O} = K_{leaf}(25^\circ C) T_K R. \quad (5.21)$$

For the diffusion coefficient of water vapour in air, we will simply use 2.82×10^{-5} m^2 s^{-1} from Summerhays [145]. With all parameters appropriately fitted, let us now plot (5.14), the intercellular water vapour concentration with respect to air channel depth, over a range of different air channel diameters:

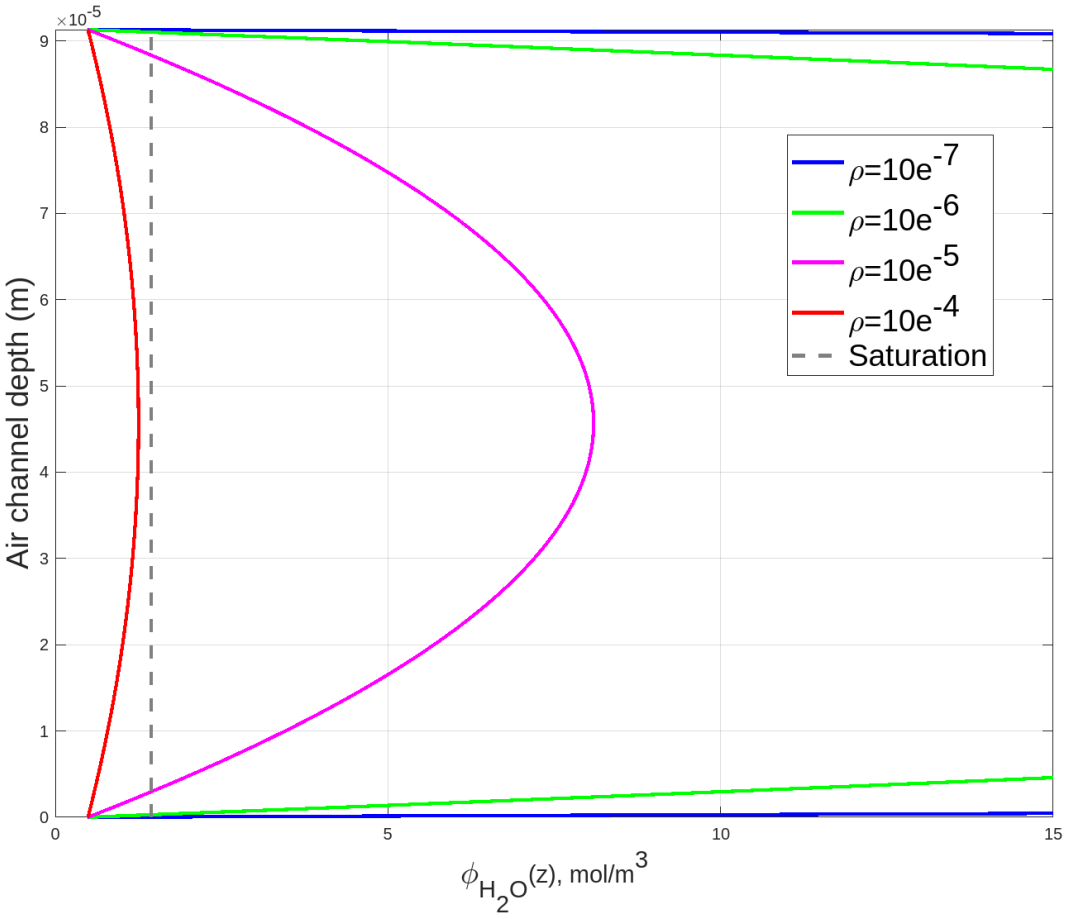

Figure 5.1: Intercellular water vapour concentration against air channel depth for a range of air channel diameters.

The result above reveals rather interesting behaviour from the air channel. The grey dotted line represents the saturation water vapour concentration of the air channel [171], and at the right of that line, the interior can be considered as saturated. The analysis shows that for air channel of size 10^{-5} m and smaller (which is generally what one might measure for *Arabidopsis thaliana*), the air channel is mostly saturated, apart from at the boundary areas, which are the exit points for the water vapour transpirating from the air channel into the atmosphere. The result also implies the presented of unsaturated gradients for large air channels, which is an observation that was also endorsed by Earles et al. [43].

This corroborates the theory put forward by Wong et al. [171] (specifically Fig.1a,b of their theory), suggesting that the humidity inside air channels isn't necessarily uniform and saturated all the way through, but rather, a gradient is

present, and one should expect the concentration to be lower at the top and bottom of the air channels, where openings (usually stomata) are present for the water vapour to escape. The idea of the presence of some areas of unsaturation inside the air channels was also reviewed by Buckley and Sack [16], and evidence of it has been shown by Canny and Huang [20], Cernusak et al. [21], and even as early as 1970 by Jarvis and Slatyer [77]. The analysis also suggests that for quite large air channels, the air channel is not quite as saturated as it could be, and is the most saturated in the middle (furthest away from points of transpiration into the atmosphere). Note that this analysis is for a *single* air channel, and that the analysis of the water vapour loss model, which is per leaf area instead, may provide a more realistic result.

Let us simulate the water vapour loss rate model per leaf area, (5.19), over a range of different air channel diameters:

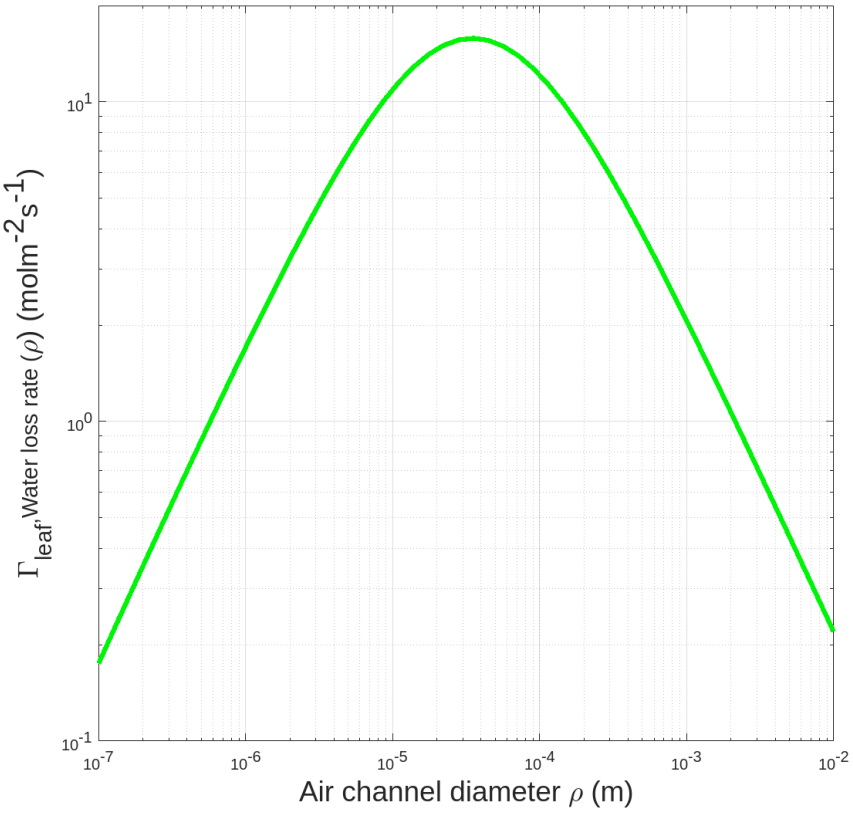

Figure 5.2: Modelled water vapour loss rate over a range of air channel diameters, with both axes in log scale.

The result suggests that water loss is greatly minimised with very small, or very large air channels. It makes sense that infinitesimally small air channels reduce the amount of water loss, as they will be at water vapour saturation concentration almost through the entire depth of the air channel. It may seem perplexing at first that very large air channels also accomplish this minimisation of water loss, but we remind the reader here that the air channel diameter (combined with the air channel depth) is a proxy to the amount of intercellular surface area available for water to diffuse from the cells into the air channels, and out into the atmosphere, and that the model uses a bounded region of interest (just like a leaf having a limited area) - **both very small and very large air channels within a fixed area, such as leaf area, reduce the amount of intercellular surface area available for water to diffuse away**, as seen in Chapter 3 (with the surface area acting as a constraint also described by Ren et al. [124]).

It it perhaps more helpful to compare this water loss prediction with the CO_2 uptake rate model, both over the same range of air channel diameters. For the purpose of better representing this visually, let us now pose the water loss result with an inverted y-axis over a linear scale, as shown in Fig. 5.3. The combined result here may first seem odd. On one hand, the CO_2 model suggests that leaves should avoid very small and very large air channels to maximise CO_2 uptake. On the other hand, the water loss model suggests the opposite - leaves should favour the extremes, i.e., infinitesimally small and infinitely large air channels, and the water vapour loss model even reaches a near zero loss at those extremes. Clearly, the results from both models clash with each other, so what is going on?

The combined results of our models actually exhibit a phenomenon known as the leaf's dilemma. Raschke [123] eleganty described it as: *'Satisfaction of a leaf's need for* CO_2 *requires an intensive gas exchange between mesophyll and atmosphere; prevention of excessive water loss demands that gas exchange be kept low'*. This result from our models is rather surprising, as neither model here contains explicit information about stomatal mechanisms, and yet the leaf's dilemma is typically portrayed from a stomatal point of view - stomata are responsible for dynamically opening and closing to ensuring ample CO_2 supply for photosynthesis, while simultaneously avoiding excessive transpiration [26, 38, 64, 182]. Here, we demonstrate that it is possible to predict the leaf's dilemma with structural models of palisade air channels, without intimate knowledge of the stomatal behaviour.

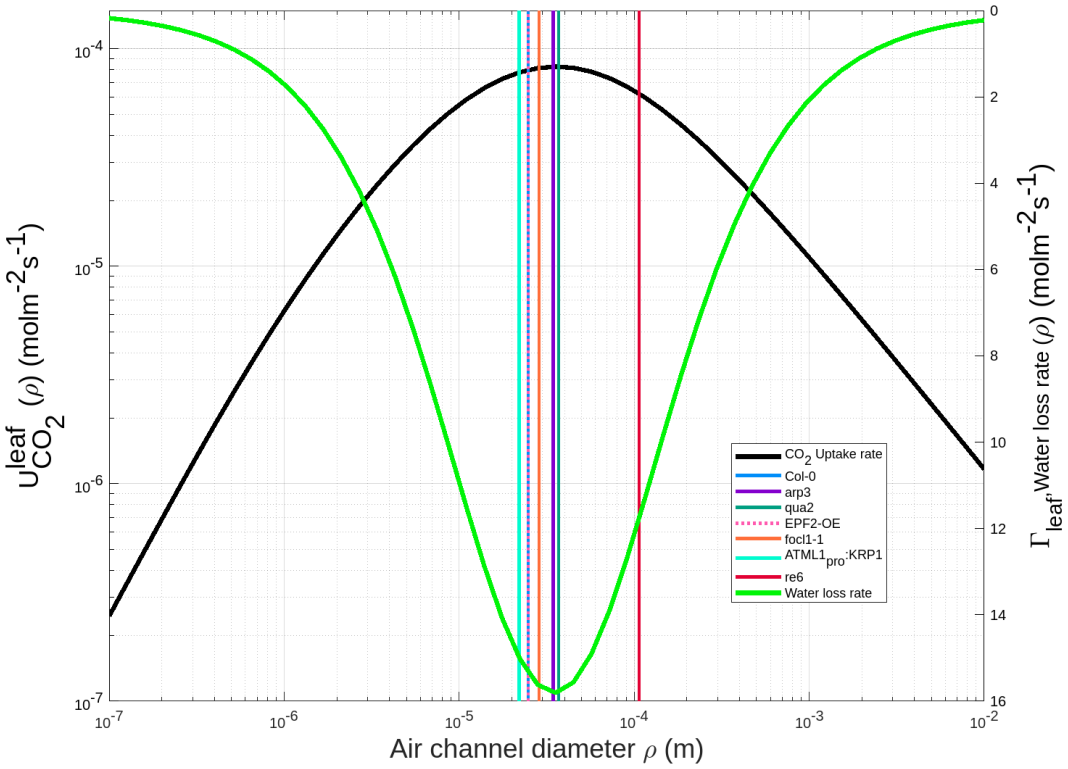

Figure 5.3: CO_2 uptake rate model (black, left log y-axis) compared to water vapour loss rate model (neon green, right linear y-axis), over a range of air channel diameters, with references to measured air channel diameters of *Arabidopsis thaliana* mutants.

However, looking at the prediction on figure 5.3 and focusing on where the measured *Arabidopsis thaliana* mutants lie, one might ask: if the leaf is faced with such a balancing conundrum, shouldn't the measured samples be closer to the intercept of the two models, where the best of both worlds might be? Why do they seem to optimise for CO_2 and disregard minimising water loss?

There are some plausible reasons for this. All the samples were grown under 'optimal' conditions, and as such, had a constant and ample supply of water, and as such may simply favour optimising towards CO_2 uptake as they haven't had to alter leaf architecture to adapt to water stress. While this claim will greatly benefit being verified experimentally by growing the same mutants under different intensities of water stress (i.e., reducing the amount of available water to them), there is already evidence suggesting that well hydrated plants optimise their behaviour for CO_2 assimilation as opposed to water loss [138].

In addition to this, it is known that growth under water stress influences the resulting leaf architecture [22, 108, 128]. Brodribb et al. [15] also observed that while at lower K_{leaf} values, hydraulic conductance and photosynthetic assimilation showed a close correlation, but at higher values ($>$15 mmol m^{-2} s^{-1} MPa^{-1}, compared to the 35 mmol m^{-2} s^{-1} MPa^{-1} we used for model fitting), investing in K_{leaf} no longer followed a proportional relationship with photosynthetic yield and instead lead to diminishing returns - this suggests that species with high K_{leaf}, such as *Arabidopsis thaliana* may skew the balance towards CO_2 uptake over water loss.

Chapter 6

Conclusions and Future Work

6.1 Summary

Throughout the last decade, research on modelling the relationship between leaf morphology, mesophyll structure and leaf function has been greatly facilitated by advances in the imaging field, such as lab-based micro-CT scanning. In this thesis, we were able to quantify the palisade mesophyll at a 3D microscale through measurements obtained from CT data. This allowed us to measure and calculate direct structural descriptors of the palisade geometry, such as air channel diameter and depth. These structural measurements, coupled with the foundational knowledge that plant morphology at different spatial scales has an impact on leaf function [17], for instance the relationship between internal exposed mesophyll surface area and CO_2 assimilation rate [109], lead to us applying Fick's first law of diffusion to obtain a governing equation. Through that, a model of CO_2 uptake in the palisade mesophyll was derived, and was later parameterised & Leave-One-Out cross-validated using gas exchange data, leading to effective CO_2 uptake rate predictions that were close to measured CO_2 assimilation rates.

While there are more complex models that would explicitly describe some of the

internal processes, such as breaking down the conductance pathway into different components such as intercellular air space, cell membrane etc., these often rely on multiple assumptions to quantifying such parameters, which are often kept fixed even if the analysis is extended to various species. Our model circumvented this by relying on a low number of assumptions and key parameters, while still providing a relatively high degree of predictability on the estimated CO_2 uptake, as seen in Table 4.3.

In addition to this, we observed a strong relationship between a deviation factor α derived from the cross-validation and the air channel depth L_z, as shown in figure 4.3, and this observation was dissected and analysed with support from several related observations in relevant literature. One of they key advantages of this model is its scalability, not only in terms of smaller or larger ROIs, but also to a local level, where it can be computed for individual measurements of air channel diameters, perhaps in a similar fashion to the discretisation and computational meshing applied on 3D data, as seen in Ho et al. [68].

Further to this observation, we also concluded that the corrected CO_2 conductance coefficient was highly likely to vary with air channel depth rather than being constant through, and could be a function of light absorption and chlorophyll distribution through the palisade depth. However, due to a lack of mechanistic understanding behind this complex interaction, we opted for a numerical approach by representing the now varying CO_2 conductance coefficient with a polynomial expression. Both an exhaustive search method (grid search) and a random search method (genetic algorithm) were used here, and the results showed that relationship between the CO_2 uptake $U_{CO_2}^{leaf}$ and the CO_2 conductance coefficient $G_{CO_2}(z)$ was likely not a simple mechanistic relationship that could be described by a polynomial equation. This prompted the need to further explore the relationship between palisade mesophyll structure, CO_2 uptake, CO_2 assimilation and mesophyll conductance.

We have also proposed a diffusion-driven water loss model using the same structural parameters as our CO_2 uptake rate model. While this water loss model remained largely conceptual and was not fitted to paired structural and gas exchange, largely owing to the lack of measurements at the air channel scale, we still fit the model using our measured structural data and fir the gaps with knowl-

edge from literature. Despite our limitations, we showed that when compared to the CO_2 uptake rate model, an interesting observation happened where the leaf's dilemma could be shown with two structural models of the intercellular air channel, without explicit knowledge of stomatal behaviour.

To summarise, CO_2 assimilation occurs via diffusion through the intercellular air channels and into the mesophyll tissue, where CO_2 fixation occurs via chloroplasts. Experimental observation indicates that air channel structure is complex and locally variable, but consistent for any one type of plant kept under a constant environment [87]. Experimental data also shows that different types of one plant, i.e., mutants, have differences in either the air channel structure, biochemical parameters such as mesophyll conductance, or both, and concurrently exhibit different rates of assimilation. From this knowledge, we have developed a physical diffusion-based framework focusing on the palisade structure, which is supported by data-driven estimation. As a result, we are able to predict the biological function of intercellular CO_2 uptake rate from the mesophyll structure by applying simple, but solid methods from engineering in plant science.

6.2 Future work

An obvious limitation of this study is the fact that only the palisade mesophyll was modelled. Although it is thought that the spongy layer is not a major contributor to CO_2 assimilation, with its main purpose being to diffuse gas and scatter light [14], the spongy mesophyll has been shown to vary in depth in Arabidopsis mutants [87], and could potentially have an impact on some of the model parameters. Recent studies [14] have shown that some plants could be optimising their spongy mesophyll layer for maximum photosynthesis, which could impact our deviation factor estimation, and give more insight to the role of the spongy layer.

The impact of lateral connections between the air channels has also not been assessed. This would introduce the concept of lateral diffusion and connectivity between air channels into the framework [14, 42]. An extension to the modelling framework could be developed by applying simple graph theoretical models, or transport models as seen in Zheng et al. [183].

As discussed previously, non-invasive and local water flux measurements at the air channel scale are still a novelty [75, 171], and given more adequate research, we will in the future be able to obtain precise measurements to validate the H_2O loss model in Chapter 5. In addition to this, the relationship between CO_2 uptake and H_2O loss within the leaf structure has often been appreciated to be coupled [184]. In reality, changes in water vapour inside the air channel would lead to changes in the diffusion constant of CO_2 and would lead to a knock on effect on the mesophyll conductance to CO_2 and the leaf hydraulic conductance, in turn affecting the CO_2 uptake into the cells from the air channel. Using our two models of CO_2 uptake and H_2O loss, the framework could perhaps be extended into a system of coupled models, where the behaviour of one directly affects the other, leading to a more accurate depiction of the actual physiological scenario in play here.

Appendix A

Calculating the concentration of CO_2

Leaf temperature is assumed to be constant at 25°C, which is 298 15K.

A reminder that Avogadro's number is $N_A = 6.022\,141\,29 \times 10^{23}\,\text{mol}^{-1}$ and the Boltzmann constant, $k_b = 1.38 \times 10^{-23}\,\text{m}^2\,\text{kg}\,\text{s}^{-2}\,\text{K}^{-1}$. Taking $P_{\text{atmospheric}}$ to be $1.01 \times 10^5\,\text{Pa}$, the number of moles of air at 25°C is:

$$N_{\text{mols}} = \frac{PV}{k_b T} \times \frac{1}{N_A} \tag{A.1}$$

This entails that 1 mol of air would take up $\frac{1}{N_{\text{mols}}}$ L $\rightarrow$ 24.36 L.

In SI units, we get $(\frac{1000}{24.36}) = 41.1\text{mol}\,\text{m}^{-3}$

This entails that the CO_2 concentration at atmospheric level is:

$$\begin{aligned} \phi_{CO_2} &= (\text{mol fraction of } CO_2 \text{ in atmosphere}) \times 41.1, \\ &= \frac{400}{1000000} \times 41.1 \\ &= 0.0164\ \text{mol}\,\text{m}^{-3}. \end{aligned} \tag{A.2}$$

Bibliography

[1] T. Aalto and E. Juurola. Parametrization of a biochemical co˜ 2 exchange model for birch (betula pendula roth.). *Boreal Environment Research*, 6(1): 53–64, 2001.

[2] T. Aalto and E. Juurola. A three-dimensional model of CO_2 transport in airspaces and mesophyll cells of a silver birch leaf. *Plant, cell & environment*, 25(11):1399–1409, 2002.

[3] W.W. Adams III and I. Terashima. *The leaf: a platform for performing photosynthesis*, volume 44. Springer, 2018.

[4] A.L. Baillie. The relationship between leaf cellular architecture and leaf-level photosynthesis. September 2017.

[5] W.J. Barnes, E. Zelinsky, and C.T. Anderson. Polygalacturonase activity promotes aberrant cell separation in the quasimodo2 mutant of arabidopsis thaliana. *The Cell Surface*, 8:100069, 2022.

[6] C. Bathellier, G. Tcherkez, G.H. Lorimer, and G.D. Farquhar. Rubisco is not really so bad. *Plant, cell & environment*, 41(4):705–716, 2018.

[7] H.N. Berghuijs, X. Yin, Q.T. Ho, S.M. Driever, M.A. Retta, B.M. Nicolaï, and P.C. Struik. Mesophyll conductance and reaction-diffusion models for co2 transport in c3 leaves; needs, opportunities and challenges. *Plant science*, 252:62–75, 2016.

[8] J. Bergstra and Y. Bengio. Random search for hyper-parameter optimization. *Journal of machine learning research*, 13(2), 2012.

[9] C.J. Bernacchi, A.R. Portis, H. Nakano, S. Von Caemmerer, and S.P. Long. Temperature response of mesophyll conductance. implications for the determination of rubisco enzyme kinetics and for limitations to photosynthesis in vivo. *Plant physiology*, 130(4):1992–1998, 2002.

[10] C. Bernacchi, E. Singsaas, C. Pimentel, A. Portis Jr, and S.P. Long. Improved temperature response functions for models of rubisco-limited photosynthesis. *Plant, Cell & Environment*, 24(2):253–259, 2001.

[11] H.E. Boccalandro, M.L. Rugnone, J.E. Moreno, E.L. Ploschuk, L. Serna, M.J. Yanovsky, and J.J. Casal. Phytochrome b enhances photosynthesis at the expense of water-use efficiency in arabidopsis. *Plant Physiology*, 150(2): 1083–1092, 2009.

[12] J.D. Boerckel, D.E. Mason, A.M. McDermott, and E. Alsberg. Microcomputed tomography: approaches and applications in bioengineering. *Stem cell research & therapy*, 5(6):1–12, 2014.

[13] A.M. Borsuk and C.R. Brodersen. The spatial distribution of chlorophyll in leaves. *Plant Physiology*, 180(3):1406–1417, 2019.

[14] A.M. Borsuk, A.B. Roddy, G. Théroux-Rancourt, and C.R. Brodersen. Structural organization of the spongy mesophyll. *The New Phytologist*, 234(3): 946, 2022.

[15] T.J. Brodribb, N.M. Holbrook, M.A. Zwieniecki, and B. Palma. Leaf hydraulic capacity in ferns, conifers and angiosperms: impacts on photosynthetic maxima. *New phytologist*, 165(3):839–846, 2005.

[16] T.N. Buckley and L. Sack. The humidity inside leaves and why you should care: implications of unsaturation of leaf intercellular airspaces. *American Journal of Botany*, 106(5):618, 2019.

[17] A. Bucksch, A. Atta-Boateng, A.F. Azihou, D. Battogtokh, A. Baumgartner, B.M. Binder, S.A. Braybrook, C. Chang, V. Coneva, T.J. DeWitt, et al. Morphological plant modeling: unleashing geometric and topological potential within the plant sciences. *Frontiers in plant science*, 8:900, 2017.

[18] F.A. Busch and R.F. Sage. The sensitivity of photosynthesis to o2 and co2 concentration identifies strong rubisco control above the thermal optimum. *New Phytologist*, 213(3):1036–1051, 2017.

[19] F.A. Busch, T.L. Sage, A.B. Cousins, and R.F. Sage. C3 plants enhance rates of photosynthesis by reassimilating photorespired and respired co2. *Plant, Cell & Environment*, 36(1):200–212, 2013.

[20] M. Canny and C. Huang. Leaf water content and palisade cell size. *New phytologist*, 170(1):75–85, 2006.

[21] L.A. Cernusak, N. Ubierna, M.W. Jenkins, S.R. Garrity, T. Rahn, H.H. Powers, D.T. Hanson, S. Sevanto, S.C. Wong, N.G. McDowell, et al. Unsaturation of vapour pressure inside leaves of two conifer species. *Scientific reports*, 8(1):7667, 2018.

[22] K. Chartzoulakis, A. Patakas, G. Kofidis, A. Bosabalidis, and A. Nastou. Water stress affects leaf anatomy, gas exchange, water relations and growth of two avocado cultivars. *Scientia horticulturae*, 95(1-2):39–50, 2002.

[23] V.C. Clarke, F.R. Danila, and S. von Caemmerer. CO_2 diffusion in tobacco: a link between mesophyll conductance and leaf anatomy. *Interface Focus*, 11(2):20200040, 2021.

[24] J.R. Cooke and R.H. Rand. Diffusion resistance models. In *Predicting photosynthesis for ecosystem models*, pages 93–121. CRC Press, 1980.

[25] G.M. Cooper, R.E. Hausman, and R.E. Hausman. *The cell: a molecular approach*, volume 4. ASM press Washington, DC, 2007.

[26] I. Cowan. Stomatal behaviour and environment. In *Advances in botanical research*, volume 4, pages 117–228. Elsevier, 1978.

[27] F.B. Daher and S.A. Braybrook. How to let go: pectin and plant cell adhesion. *Frontiers in plant science*, 6:523, 2015.

[28] L. De Veylder, T. Beeckman, and D. Inzé. The ins and outs of the plant cell cycle. *Nature Reviews Molecular Cell Biology*, 8(8):655–665, 2007.

[29] R.M. Deans, T.J. Brodribb, F.A. Busch, and G.D. Farquhar. Plant water-use strategy mediates stomatal effects on the light induction of photosynthesis. *New Phytologist*, 222(1):382–395, 2019.

[30] R.M. Deans, G.D. Farquhar, and F.A. Busch. Estimating stomatal and biochemical limitations during photosynthetic induction. *Plant, Cell & Environment*, 42(12):3227–3240, 2019.

[31] R.M. Deans, T.J. Brodribb, F.A. Busch, and G.D. Farquhar. Optimization can provide the fundamental link between leaf photosynthesis, gas exchange and water relations. *Nature Plants*, 6(9):1116–1125, 2020.

[32] M.J. Deeks and P.J. Hussey. Arp2/3 and 'the shape of things to come'. *Current opinion in plant biology*, 6(6):561–567, 2003.

[33] W. Dewitte, C. Riou-Khamlichi, S. Scofield, J.S. Healy, A. Jacqmard, N.J. Kilby, and J.A. Murray. Altered cell cycle distribution, hyperplasia, and inhibited differentiation in arabidopsis caused by the d-type cyclin cycd3. *The Plant Cell*, 15(1):79–92, 2003.

[34] S. Dhondt, H. Vanhaeren, D. Van Loo, V. Cnudde, and D. Inzé. Plant structure visualization by high-resolution x-ray computed tomography. *Trends in plant science*, 15(8):419–422, 2010.

[35] C. Dorca-Fornell, R. Pajor, C. Lehmeier, M. Pérez-Bueno, M. Bauch, J. Sloan, C. Osborne, S. Rolfe, C. Sturrock, S. Mooney, et al. Increased leaf mesophyll porosity following transient retinoblastoma-related protein silencing is revealed by microcomputed tomography imaging and leads to a system-level physiological response to the altered cell division pattern. *The Plant Journal*, 76(6):914–929, 2013.

[36] M. Doube, M.M. Kłosowski, I. Arganda-Carreras, F.P. Cordelières, R.P. Dougherty, J.S. Jackson, B. Schmid, J.R. Hutchinson, and S.J. Shefelbine. Bonej: free and extensible bone image analysis in imagej. *Bone*, 47(6): 1076–1079, 2010.

[37] G.J. Dow and D.C. Bergmann. Patterning and processes: how stomatal development defines physiological potential. *Current opinion in plant biology*, 21:67–74, 2014.

[38] P.L. Drake, H.J. De Boer, S.J. Schymanski, and E.J. Veneklaas. Two sides to every leaf: water and co 2 transport in hypostomatous and amphistomatous leaves. *New Phytologist*, 222(3):1179–1187, 2019.

[39] J. Du, A. Kirui, S. Huang, L. Wang, W.J. Barnes, S.N. Kiemle, Y. Zheng, Y. Rui, M. Ruan, S. Qi, et al. Mutations in the pectin methyltransferase quasimodo2 influence cellulose biosynthesis and wall integrity in arabidopsis. *Plant Cell*, 32(11):3576–3597, 2020.

[40] J. Du, C.T. Anderson, and C. Xiao. Dynamics of pectic homogalacturonan in cellular morphogenesis and adhesion, wall integrity sensing and plant development. *Nature Plants*, 8(4):332–340, 2022.

[41] A. Du Plessis, C. Broeckhoven, A. Guelpa, and S.G. Le Roux. Laboratory x-ray micro-computed tomography: a user guideline for biological samples. *Gigascience*, 6(6):gix027, 2017.

[42] J.M. Earles, G. Théroux-Rancourt, A.B. Roddy, M.E. Gilbert, A.J. McElrone, and C.R. Brodersen. Beyond porosity: 3d leaf intercellular airspace traits that impact mesophyll conductance. *Plant Physiology*, 178(1):148–162, 2018.

[43] J.M. Earles, T.N. Buckley, C.R. Brodersen, F.A. Busch, F.J. Cano, B. Choat, J.R. Evans, G.D. Farquhar, R. Harwood, M. Huynh, et al. Embracing 3d complexity in leaf carbon–water exchange. *Trends in plant science*, 24(1): 15–24, 2019.

[44] P.V. Ellsworth, P.Z. Ellsworth, N.K. Koteyeva, and A.B. Cousins. Cell wall properties in oryza sativa influence mesophyll co 2 conductance. *New Phytologist*, 219(1):66–76, 2018.

[45] K. Esau et al. Plant anatomy. *Plant Anatomy.*, (2nd Edition), 1965.

[46] C. Éva, M. Oszvald, and L. Tamás. Current and possible approaches for improving photosynthetic efficiency. *Plant Science*, 280:433–440, 2019.

[47] J.R. Evans. Carbon fixation profiles do reflect light absorption profiles in leaves. *Functional Plant Biology*, 22(6):865–873, 1995.

[48] J.R. Evans. Leaf anatomy enables more equal access to light and CO_2 between chloroplasts. *The New Phytologist*, 143(1):93–104, 1999.

[49] J.R. Evans. Mesophyll conductance: walls, membranes and spatial complexity. *New Phytologist*, 229(4):1864–1876, 2021.

[50] J.R. Evans, R. Kaldenhoff, B. Genty, and I. Terashima. Resistances along the CO_2 diffusion pathway inside leaves. *Journal of experimental botany*, 60 (8):2235–2248, 2009.

[51] J. Evans and T.C. Vogelmann. Profiles of 14c fixation through spinach leaves in relation to light absorption and photosynthetic capacity. *Plant, Cell & Environment*, 26(4):547–560, 2003.

[52] G.D. Farquhar, S.v. von Caemmerer, and J.A. Berry. A biochemical model of photosynthetic co 2 assimilation in leaves of c 3 species. *planta*, 149: 78–90, 1980.

[53] G.D. Farquhar, S. Von Caemmerer, and J.A. Berry. Models of photosynthesis. *Plant physiology*, 125(1):42–45, 2001.

[54] A. Fick. Ueber diffusion. *Annalen der Physik*, 170(1):59–86, 1855.

[55] J. Flexas, M. Ribas-Carbo, A. Diaz-Espejo, J. Galmés, and H. Medrano. Mesophyll conductance to CO_2 current knowledge and future prospects. *Plant, cell & environment*, 31(5):602–621, 2008.

[56] J. Flexas, F. Loreto, and H. Medrano. *Terrestrial photosynthesis in a changing environment: a molecular, physiological, and ecological approach*. Cambridge University Press, 2012.

[57] J. Flexas, C. Scoffoni, J. Gago, and L. Sack. Leaf mesophyll conductance and leaf hydraulic conductance: an introduction to their measurement and coordination. *Journal of Experimental Botany*, 64(13):3965–3981, 2013.

[58] J. Flexas, M.J. Clemente-Moreno, J. Bota, T.J. Brodribb, J. Gago, Y. Mizokami, M. Nadal, A.V. Perera-Castro, M. Roig-Oliver, D. Sugiura, et al. Cell wall thickness and composition are involved in photosynthetic limitation. *Journal of Experimental Botany*, 72(11):3971–3986, 2021.

[59] C.H. Foyer, A.V. Ruban, and P.J. Nixon. Photosynthesis solutions to enhance productivity, 2017.

[60] A.G.I. genomeanalysis@ tgr. org genomeanalysis@ gsf. de. Analysis of the genome sequence of the flowering plant arabidopsis thaliana. *nature*, 408 (6814):796–815, 2000.

[61] R. Giuliani, N. Koteyeva, E. Voznesenskaya, M.A. Evans, A.B. Cousins, and G.E. Edwards. Coordination of leaf photosynthesis, transpiration, and structural traits in rice and wild relatives (genus oryza). *Plant physiology*, 162(3):1632–1651, 2013.

[62] R. González-Bayon, E.A. Kinsman, V. Quesada, A. Vera, P. Robles, M.R. Ponce, K.A. Pyke, and J.L. Micol. Mutations in the reticulata gene dramatically alter internal architecture but have little effect on overall organ shape in arabidopsis leaves. *Journal of experimental botany*, 57(12):3019–3031, 2006.

[63] E. Gotoh, N. Suetsugu, T. Higa, T. Matsushita, H. Tsukaya, and M. Wada. Palisade cell shape affects the light-induced chloroplast movements and leaf photosynthesis. *Scientific Reports*, 8(1):1–9, 2018.

[64] E. Grill and H. Ziegler. A plant's dilemma. *Science*, 282(5387):252–253, 1998.

[65] Y. Grunwald, N. Wigoda, N. Sade, A. Yaaran, T. Torne, S.C. Gosa, N. Moran, and M. Moshelion. Arabidopsis leaf hydraulic conductance is regulated by xylem sap ph, controlled, in turn, by a p-type h+-atpase of vascular bundle sheath cells. *The Plant Journal*, 106(2):301–313, 2021.

[66] P.C. Harley and T.D. Sharkey. An improved model of c 3 photosynthesis at high co 2: reversed o 2 sensitivity explained by lack of glycerate reentry into the chloroplast. *Photosynthesis Research*, 27:169–178, 1991.

[67] P.C. Harley, F. Loreto, G. Di Marco, and T.D. Sharkey. Theoretical considerations when estimating the mesophyll conductance to co2 flux by analysis of the response of photosynthesis to co2. *Plant physiology*, 98(4):1429–1436, 1992.

[68] Q.T. Ho, H.N. Berghuijs, R. Watté, P. Verboven, E. Herremans, X. Yin, M.A. Retta, B. Aernouts, W. Saeys, L. Helfen, et al. Three-dimensional microscale modelling of co 2 transport and light propagation in tomato

leaves enlightens photosynthesis. *Plant, cell & environment*, 39(1):50–61, 2016.

[69] B.L. Holland, N.A. Monk, R.H. Clayton, and C.P. Osborne. A theoretical analysis of how plant growth is limited by carbon allocation strategies and respiration. *in silico Plants*, 1(1):diz004, 2019.

[70] L. Hunt and J.E. Gray. The signaling peptide epf2 controls asymmetric cell divisions during stomatal development. *Current Biology*, 19(10):864–869, 2009.

[71] L. Hunt and J.E. Gray. How the stomate got his pore: very long chain fatty acids and a structural cell wall protein sculpt the guard cell outer cuticular ledge. *New Phytologist*, 228(6):1698–1700, 2020.

[72] L. Hunt, S. Amsbury, A. Baillie, M. Movahedi, A. Mitchell, M. Afsharinafar, K. Swarup, T. Denyer, J.K. Hobbs, R. Swarup, et al. Formation of the stomatal outer cuticular ledge requires a guard cell wall proline-rich protein. *Plant Physiology*, 174(2):689–699, 2017.

[73] S. Hussain, Z. Ulhassan, M. Brestic, M. Zivcak, W. Zhou, S.I. Allakhverdiev, X. Yang, M.E. Safdar, W. Yang, and W. Liu. Photosynthesis research under climate change. *Photosynthesis Research*, 150:5–19, 2021.

[74] L. Ivanova and V. P'yankov. Structural adaptation of the leaf mesophyll to shading. *Russian Journal of Plant Physiology*, 49:419–431, 2002.

[75] P. Jain, W. Liu, S. Zhu, C.Y.Y. Chang, J. Melkonian, F.E. Rockwell, D. Pauli, Y. Sun, W.R. Zipfel, N.M. Holbrook, et al. A minimally disruptive method for measuring water potential in planta using hydrogel nanoreporters. *Proceedings of the National Academy of Sciences*, 118(23):e2008276118, 2021.

[76] S.A. James, W.K. Smith, and T.C. Vogelmann. Ontogenetic differences in mesophyll structure and chlorophyll distribution in eucalyptus globulus ssp. globulus (myrtaceae). *American Journal of Botany*, 86(2):198–207, 1999.

[77] P. Jarvis and R. Slatyer. The role of the mesophyll cell wall in leaf transpiration. *Planta*, pages 303–322, 1970.

[78] C. Jeffree, J. Dale, and S. Fry. The genesis of intercellular spaces in developing leaves of phaseolus vulgaris l. *Protoplasma*, 132:90–98, 1986.

[79] W.J. Jeong, Y.I. Park, K. Suh, J.A. Raven, O.J. Yoo, and J.R. Liu. A large population of small chloroplasts in tobacco leaf cells allows more effective chloroplast movement than a few enlarged chloroplasts. *Plant Physiology*, 129(1):112–121, 2002.

[80] K. Jin, G. Chen, Y. Yang, Z. Zhang, and T. Lu. Strategies for manipulating rubisco and creating photorespiratory bypass to boost c3 photosynthesis: Prospects on modern crop improvement. *Plant, Cell & Environment*, 46(2): 363–378, 2023.

[81] G.T. Kim, K. Shoda, T. Tsuge, K.H. Cho, H. Uchimiya, R. Yokoyama, K. Nishitani, and H. Tsukaya. The angustifolia gene of arabidopsis, a plant ctbp gene, regulates leaf-cell expansion, the arrangement of cortical microtubules in leaf cells and expression of a gene involved in cell-wall formation. *The EMBO journal*, 21(6):1267–1279, 2002.

[82] M.U.F. Kirschbaum. *The effects of light, temperature and water stress on photosynthesis in Eucalyptus pauciflora*. The Australian National University (Australia), 1986.

[83] M. Kirschbaum and G. Farquhar. Temperature dependence of whole-leaf photosynthesis in eucalyptus pauciflora sieb. ex spreng. *Functional Plant Biology*, 11(6):519–538, 1984.

[84] J. Knauer, M. Cuntz, J.R. Evans, Ü. Niinemets, T. Tosens, L.L. Veromann-Jürgenson, C. Werner, and S. Zaehle. Contrasting anatomical and biochemical controls on mesophyll conductance across plant functional types. *New Phytologist*, 236(2):357–368, 2022.

[85] B. Kok. On the inhibition of photosynthesis by intense light. *Biochimica et biophysica acta*, 21(2):234–244, 1956.

[86] D.W. Lee, R.A. Bone, S.L. Tarsis, and D. Storch. Correlates of leaf optical properties in tropical forest sun and extreme-shade plants. *American Journal of Botany*, 77(3):370–380, 1990.

[87] C. Lehmeier, R. Pajor, M.R. Lundgren, A. Mathers, J. Sloan, M. Bauch, A. Mitchell, C. Bellasio, A. Green, D. Bouyer, et al. Cell density and airspace patterning in the leaf can be manipulated to increase leaf photosynthetic capacity. *The Plant Journal*, 92(6):981–994, 2017.

[88] J. Li, C. Cai, and Z.H. Li. Knudsen diffusion differs from fickian diffusion. *Physics of Fluids*, 33(4):042009, 2021.

[89] L.J. LI, F. Ren, X.Q. GAO, P.C. WEI, and X.C. WANG. The reorganization of actin filaments is required for vacuolar fusion of guard cells during stomatal opening in arabidopsis. *Plant, cell & environment*, 36(2):484–497, 2013.

[90] I. LI-COR. *LI-6800 Portable Photosynthesis System Instruction Manual, First Edition*. LI-COR, Inc. Lincoln, NE, 2016.

[91] J. Lloyd, J. Syvertsen, P. Kriedemann, and G. Farquhar. Low conductances for CO_2 diffusion from stomata to the sites of carboxylation in leaves of woody species. *Plant, Cell & Environment*, 15(8):873–899, 1992.

[92] S.P. Long and C. Bernacchi. Gas exchange measurements, what can they tell us about the underlying limitations to photosynthesis? procedures and sources of error. *Journal of experimental botany*, 54(392):2393–2401, 2003.

[93] F. Loreto, P.C. Harley, G. Di Marco, and T.D. Sharkey. Estimation of mesophyll conductance to co2 flux by three different methods. *Plant physiology*, 98(4):1437–1443, 1992.

[94] M.R. Lundgren and A.J. Fleming. Cellular perspectives for improving mesophyll conductance. *The Plant Journal*, 101(4):845–857, 2020.

[95] M.R. Lundgren, A. Mathers, A.L. Baillie, J. Dunn, M.J. Wilson, L. Hunt, R. Pajor, M. Fradera-Soler, S. Rolfe, C.P. Osborne, et al. Mesophyll porosity is modulated by the presence of functional stomata. *Nature Communications*, 10(1):2825, 2019.

[96] A. M. Smith, G. Coupland, L. Dolan, N. Harberd, J. Jones, C. Martin, R. Sablowski, and A. Amey. Carbon assimilation: Photosynthesis. In *Plant Biology*, chapter 4, pages 174–175. Garland Science, Taylor & Francis Group, LLC, New York, 2010.

[97] S. Mairhofer, T. Pridmore, J. Johnson, D.M. Wells, M.J. Bennett, S.J. Mooney, and C.J. Sturrock. X-ray computed tomography of crop plant root systems grown in soil. *Current Protocols in Plant Biology*, 2(4):270–286, 2017.

[98] Maplesoft, a division of Waterloo Maple Inc.. Maple. URL `https://hadoop.apache.org`.

[99] D.A. Márquez, H. Stuart-Williams, L.A. Cernusak, and G.D. Farquhar. Assessing the CO_2 concentration at the surface of photosynthetic mesophyll cells. *New Phytologist*, 2023.

[100] S.C. Martins, J. Galmes, P.C. Cavatte, L.F. Pereira, M.C. Ventrella, and F.M. DaMatta. Understanding the low photosynthetic rates of sun and shade coffee leaves: bridging the gap on the relative roles of hydraulic, diffusive and biochemical constraints to photosynthesis. *PLoS One*, 9(4): e95571, 2014.

[101] A.W. Mathers, C. Hepworth, A.L. Baillie, J. Sloan, H. Jones, M. Lundgren, A.J. Fleming, S.J. Mooney, and C.J. Sturrock. Investigating the microstructure of plant leaves in 3d with lab-based x-ray computed tomography. *Plant methods*, 14(1):1–12, 2018.

[102] J. Mathur, N. Mathur, B. Kernebeck, and M. Hulskamp. Mutations in actin-related proteins 2 and 3 affect cell shape development in arabidopsis. *The Plant Cell*, 15(7):1632–1645, 2003.

[103] T.G. Mayerhöfer, S. Pahlow, and J. Popp. The bouguer-beer-lambert law: Shining light on the obscure. *ChemPhysChem*, 21(18):2029–2046, 2020.

[104] D.W. Meinke, J.M. Cherry, C. Dean, S.D. Rounsley, and M. Koornneef. Arabidopsis thaliana: a model plant for genome analysis. *Science*, 282(5389): 662–682, 1998.

[105] M. Momayyezi, A.M. Borsuk, C.R. Brodersen, M.E. Gilbert, G. Théroux-Rancourt, D.A. Kluepfel, and A.J. McElrone. Desiccation of the leaf mesophyll and its implications for co2 diffusion and light processing. *Plant, Cell & Environment*, 45(5):1362–1381, 2022.

[106] G. Mouille, M.C. Ralet, C. Cavelier, C. Eland, D. Effroy, K. Hématy, L. McCartney, H.N. Truong, V. Gaudon, J.F. Thibault, et al. Homogalacturonan synthesis in arabidopsis thaliana requires a golgi-localized protein with a putative methyltransferase domain. *The Plant Journal*, 50(4):605–614, 2007.

[107] C.D. Muir. tealeaves: an r package for modelling leaf temperature using energy budgets. *AoB Plants*, 11(6):plz054, 2019.

[108] A. Nardini and S. Salleo. Water stress-induced modifications of leaf hydraulic architecture in sunflower: co-ordination with gas exchange. *Journal of Experimental Botany*, 56(422):3093–3101, 2005.

[109] P.S. Nobel, L.J. Zaragoza, and W.K. Smith. Relation between mesophyll surface area, photosynthetic rate, and illumination level during development for leaves of plectranthus parviflorus henckel. *Plant Physiology*, 55(6):1067–1070, 1975.

[110] R. Pajor, A. Fleming, C. Osborne, S. Rolfe, C. Sturrock, and S. Mooney. Seeing space: visualization and quantification of plant leaf structure using x-ray micro-computed tomography: View point. *Journal of Experimental Botany*, 64(2):385–390, 2013.

[111] Y.I. Park, W.S. Chow, and J.M. Anderson. Chloroplast movement in the shade plant tradescantia albiflora helps protect photosystem ii against light stress. *Plant physiology*, 111(3):867–875, 1996.

[112] D.F. Parkhurst. Diffusion of CO_2 and other gases inside leaves. *New phytologist*, 126(3):449–479, 1994.

[113] D.F. Parkhurst and K.A. Mott. Intercellular diffusion limits to CO_2 uptake in leaves: studies in air and helox. *Plant physiology*, 94(3):1024–1032, 1990.

[114] D.F. Parkhurst, S.C. Wong, G.D. Farquhar, and I.R. Cowan. Gradients of intercellular CO_2 levels across the leaf mesophyll. *Plant Physiology*, 86(4): 1032–1037, 1988.

[115] W. Peters, I.R. van der Velde, E. Van Schaik, J.B. Miller, P. Ciais, H.F. Duarte, I.T. van der Laan-Luijkx, M.K. van der Molen, M. Scholze, K. Schaefer, et al. Increased water-use efficiency and reduced co2 uptake by plants

during droughts at a continental scale. *Nature geoscience*, 11(10):744–748, 2018.

[116] T.L. Pons, J. Flexas, S. Von Caemmerer, J.R. Evans, B. Genty, M. Ribas-Carbo, and E. Brugnoli. Estimating mesophyll conductance to CO_2 methodology, potential errors, and recommendations. *Journal of Experimental Botany*, 60(8):2217–2234, 2009.

[117] A.R. Portis and M.A. Parry. Discoveries in rubisco (ribulose 1, 5-bisphosphate carboxylase/oxygenase): a historical perspective. *Photosynthesis Research*, 94:121–143, 2007.

[118] D. Pritchard and J. Currie. Diffusion of coefficients of carbon dioxide, nitrous oxide, ethylene and ethane in air and their measurement. *Journal of Soil Science*, 33(2):175–184, 1982.

[119] C.A. Raines. The calvin cycle revisited. *Photosynthesis research*, 75:1–10, 2003.

[120] C.A. Raines. Increasing photosynthetic carbon assimilation in c3 plants to improve crop yield: current and future strategies. *Plant physiology*, 155(1): 36–42, 2011.

[121] R. Rand and J. Cooke. A comprehensive model for c02 assimilation in leaves. *Transactions of the ASAE*, 23(3):601–0607, 1980.

[122] R.H. Rand. Gaseous diffusion in the leaf interior. *Transactions of the ASAE*, 20(4):701–0704, 1977.

[123] K. Raschke. How stomata resolve the dilemma of opposing priorities. *Philosophical Transactions of the Royal Society of London. B, Biological Sciences*, 273(927):551–560, 1976.

[124] T. Ren, S.M. Weraduwage, and T.D. Sharkey. Prospects for enhancing leaf photosynthetic capacity by manipulating mesophyll cell morphology. *Journal of Experimental Botany*, 70(4):1153–1165, 2019.

[125] A.B. Roddy, G. Théroux-Rancourt, T. Abbo, J.W. Benedetti, C.R. Brodersen, M. Castro, S. Castro, A.B. Gilbride, B. Jensen, G.F. Jiang, et al. The scaling of genome size and cell size limits maximum rates of photosynthesis

with implications for ecological strategies. *International Journal of Plant Sciences*, 181(1):75–87, 2020.

[126] L. Sack and N.M. Holbrook. Leaf hydraulics. *Annu. Rev. Plant Biol.*, 57: 361–381, 2006.

[127] L. Sack and C. Scoffoni. Measurement of leaf hydraulic conductance and stomatal conductance and their responses to irradiance and dehydration using the evaporative flux method (efm). *JoVE (Journal of Visualized Experiments)*, (70):e4179, 2012.

[128] L. Sack, M.T. Tyree, and N.M. Holbrook. Leaf hydraulic architecture correlates with regeneration irradiance in tropical rainforest trees. *New Phytologist*, 167(2):403–413, 2005.

[129] J. Schindelin, I. Arganda-Carreras, E. Frise, V. Kaynig, M. Longair, T. Pietzsch, S. Preibisch, C. Rueden, S. Saalfeld, B. Schmid, et al. Fiji: an open-source platform for biological-image analysis. *Nature methods*, 9(7):676–682, 2012.

[130] J.V. Schneider, R. Rabenstein, J. Wesenberg, K. Wesche, G. Zizka, and J. Habersetzer. Improved non-destructive 2d and 3d x-ray imaging of leaf venation. *Plant methods*, 14(1):1–15, 2018.

[131] C. Scoffoni, C. Albuquerque, C.R. Brodersen, S.V. Townes, G.P. John, M.K. Bartlett, T.N. Buckley, A.J. McElrone, and L. Sack. Outside-xylem vulnerability, not xylem embolism, controls leaf hydraulic decline during dehydration. *Plant physiology*, 173(2):1197–1210, 2017.

[132] C. Scoffoni, C. Albuquerque, C.R. Brodersen, S.V. Townes, G.P. John, H. Cochard, T.N. Buckley, A.J. McElrone, and L. Sack. Leaf vein xylem conduit diameter influences susceptibility to embolism and hydraulic decline. *New Phytologist*, 213(3):1076–1092, 2017.

[133] T.D. Sharkey. Estimating the rate of photorespiration in leaves. *Physiologia Plantarum*, 73(1):147–152, 1988.

[134] T.D. Sharkey. What gas exchange data can tell us about photosynthesis. *Plant, Cell & Environment*, 39(6):1161–1163, 2015.

[135] T.D. Sharkey, C.J. Bernacchi, G.D. Farquhar, and E.L. Singsaas. Fitting photosynthetic carbon dioxide response curves for c3 leaves. *Plant, cell & environment*, 30(9):1035–1040, 2007.

[136] H. Sifton. Air-space tissue in plants. *The Botanical Review*, 11(2):108–143, 1945.

[137] H. Sifton. Air-space tissue in plants. ii. *Botanical Review*, 23(5):303–312, 1957.

[138] K.A. Simonin, E. Burns, B. Choat, M.M. Barbour, T.E. Dawson, and P.J. Franks. Increasing leaf hydraulic conductance with transpiration rate minimizes the water potential drawdown from stem to leaf. *Journal of Experimental Botany*, 66(5):1303–1315, 2015.

[139] A. Singhal, J.C. Grande, and Y. Zhou. Micro/nano-ct for visualization of internal structures. *Microscopy Today*, 21(2):16–22, 2013.

[140] S. Sivanandam, S. Deepa, S. Sivanandam, and S. Deepa. *Genetic algorithms*. Springer, 2008.

[141] J.M. Skotheim and L. Mahadevan. Physical limits and design principles for plant and fungal movements. *Science*, 308(5726):1308–1310, 2005.

[142] W.K. Smith, T.C. Vogelmann, E.H. DeLucia, D.T. Bell, and K.A. Shepherd. Leaf form and photosynthesis. *BioScience*, 47(11):785–793, 1997.

[143] R.J. Spreitzer and M.E. Salvucci. Rubisco: structure, regulatory interactions, and possibilities for a better enzyme. *Annual review of plant biology*, 53(1): 449–475, 2002.

[144] M. Stauber and R. Müller. Micro-computed tomography: a method for the non-destructive evaluation of the three-dimensional structure of biological specimens. *Osteoporosis: methods and protocols*, pages 273–292, 2008.

[145] W. Summerhays. A determination of the coefficient of diffusion of water vapour. *Proceedings of the Physical Society*, 42(3):218, 1930.

[146] A.A. Temme, J.C. Liu, J. van Hal, W.K. Cornwell, J.H.H. Cornelissen, and R. Aerts. Increases in CO_2 from past low to future high levels result in

"slower" strategies on the leaf economic spectrum. *Perspectives in plant ecology, evolution and systematics*, 29:41–50, 2017.

[147] I. Terashima, S.I. Miyazawa, and Y.T. Hanba. Why are sun leaves thicker than shade leaves?—consideration based on analyses of co 2 diffusion in the leaf. *Journal of plant research*, 114:93–105, 2001.

[148] I. Terashima, Y.T. Hanba, D. Tholen, and Ü. Niinemets. Leaf functional anatomy in relation to photosynthesis. *Plant physiology*, 155(1):108–116, 2011.

[149] G. Théroux-Rancourt, J.M. Earles, M.E. Gilbert, M.A. Zwieniecki, C.K. Boyce, A.J. McElrone, and C.R. Brodersen. The bias of a two-dimensional view: comparing two-dimensional and three-dimensional mesophyll surface area estimates using noninvasive imaging. *New Phytologist*, 215(4):1609–1622, 2017.

[150] G. Théroux-Rancourt, A.B. Roddy, J.M. Earles, M.E. Gilbert, M.A. Zwieniecki, C.K. Boyce, D. Tholen, A.J. McElrone, K.A. Simonin, and C.R. Brodersen. Maximum CO_2 diffusion inside leaves is limited by the scaling of cell size and genome size. *Proceedings of the Royal Society B*, 288(1945): 20203145, 2021.

[151] D. Tholen and X.G. Zhu. The mechanistic basis of internal conductance: a theoretical analysis of mesophyll cell photosynthesis and CO_2 diffusion. *Plant physiology*, 156(1):90–105, 2011.

[152] T. Tosens, U. Niinemets, V. Vislap, H. Eichelmann, and P. Castro Diez. Developmental changes in mesophyll diffusion conductance and photosynthetic capacity under different light and water availabilities in populus tremula: how structure constrains function. *Plant, cell & environment*, 35(5):839–856, 2012.

[153] H. Tsukaya. Re-examination of the role of endoreduplication on cell-size control in leaves. *Journal of plant research*, 132(5):571–580, 2019.

[154] P. Verboven, G. Kerckhofs, H.K. Mebatsion, Q.T. Ho, K. Temst, M. Wevers, P. Cloetens, and B.M. Nicolaï. Three-dimensional gas exchange pathways in

pome fruit characterized by synchrotron x-ray computed tomography. *Plant physiology*, 147(2):518–527, 2008.

[155] P. Verboven, E. Herremans, L. Helfen, Q.T. Ho, M. Abera, T. Baumbach, M. Wevers, and B.M. Nicolaï. Synchrotron x-ray computed laminography of the three-dimensional anatomy of tomato leaves. *The plant journal*, 81(1): 169–182, 2015.

[156] A. Verkest, C.L.d.O. Manes, S. Vercruysse, S. Maes, E. Van Der Schueren, T. Beeckman, P. Genschik, M. Kuiper, D. Inze, and L. De Veylder. The cyclin-dependent kinase inhibitor krp2 controls the onset of the endoreduplication cycle during arabidopsis leaf development through inhibition of mitotic cdka; 1 kinase complexes. *The Plant Cell*, 17(6):1723–1736, 2005.

[157] A. Verkest, C. Weinl, D. Inzé, L. De Veylder, and A. Schnittger. Switching the cell cycle. kip-related proteins in plant cell cycle control. *Plant physiology*, 139(3):1099–1106, 2005.

[158] L.L. Veromann-Jürgenson, T. Tosens, L. Laanisto, and Ü. Niinemets. Extremely thick cell walls and low mesophyll conductance: welcome to the world of ancient living! *Journal of Experimental Botany*, 68(7):1639–1653, 2017.

[159] L.L. Veromann-Jürgenson, T.J. Brodribb, Ü. Niinemets, and T. Tosens. Variability in the chloroplast area lining the intercellular airspace and cell walls drives mesophyll conductance in gymnosperms. *Journal of Experimental Botany*, 71(16):4958–4971, 2020.

[160] S.R. Vialet-Chabrand, J.S. Matthews, L. McAusland, M.R. Blatt, H. Griffiths, and T. Lawson. Temporal dynamics of stomatal behavior: modeling and implications for photosynthesis and water use. *Plant physiology*, 174 (2):603–613, 2017.

[161] H.D. Voe. *9.2: Partial Molar Quantities*, page 229. Prentice Hall, 2nd edition, 2020.

[162] T.C. Vogelmann and J. Evans. Profiles of light absorption and chlorophyll within spinach leaves from chlorophyll fluorescence. *Plant, Cell & Environment*, 25(10):1313–1323, 2002.

[163] T.C. Vogelmann and G. Martin. The functional significance of palisade tissue: penetration of directional versus diffuse light. *Plant, Cell & Environment*, 16(1):65–72, 1993.

[164] S. von Caemmerer. Rubisco carboxylase/oxygenase: from the enzyme to the globe: a gas exchange perspective. *Journal of Plant Physiology*, 252: 153240, 2020.

[165] S. von Caemmerer and J.R. Evans. Enhancing c3 photosynthesis. *Plant Physiology*, 154(2):589–592, 2010.

[166] R. Watté, B. Aernouts, R. Van Beers, E. Herremans, Q.T. Ho, P. Verboven, B. Nicolaï, and W. Saeys. Modeling the propagation of light in realistic tissue structures with mmc-fpf: a meshed monte carlo method with free phase function. *Optics express*, 23(13):17467–17486, 2015.

[167] S.E. Weise, D.J. Carr, A.M. Bourke, D.T. Hanson, D. Swarthout, and T.D. Sharkey. The arc mutants of arabidopsis with fewer large chloroplasts have a lower mesophyll conductance. *Photosynthesis Research*, 124:117–126, 2015.

[168] C. Whitewoods. Let's stick together: A pectin biosynthetic mutant reveals the interconnectedness of plant cell walls, 2020.

[169] C.D. Whitewoods. Riddled with holes: Understanding air space formation in plant leaves. *PLoS Biology*, 19(12):e3001475, 2021.

[170] C. Willmer and M. Fricker. *Stomata*, volume 2. Springer Science & Business Media, 1996.

[171] S.C. Wong, M.J. Canny, M. Holloway-Phillips, H. Stuart-Williams, L.A. Cernusak, D.A. Márquez, and G.D. Farquhar. Humidity gradients in the air spaces of leaves. *Nature Plants*, 8(8):971–978, 2022.

[172] F.I. Woodward, T.M. Smith, and W.R. Emanuel. A global land primary productivity and phytogeography model. *Global biogeochemical cycles*, 9 (4):471–490, 1995.

[173] N. Wuyts, J.C. Palauqui, G. Conejero, J.L. Verdeil, C. Granier, and C. Massonnet. High-contrast three-dimensional imaging of the arabidopsis leaf en-

ables the analysis of cell dimensions in the epidermis and mesophyll. *Plant Methods*, 6(1):1–14, 2010.

[174] Y. Xiao and X.G. Zhu. Components of mesophyll resistance and their environmental responses: a theoretical modelling analysis. *Plant, Cell & Environment*, 40(11):2729–2742, 2017.

[175] Y. Xiao, D. Tholen, and X.G. Zhu. The influence of leaf anatomy on the internal light environment and photosynthetic electron transport rate: exploration with a new leaf ray tracing model. *Journal of experimental botany*, 67(21):6021–6035, 2016.

[176] Y. Xiao, J. Sloan, C. Hepworth, C.P. Osborne, A.J. Fleming, X. Chen, and X.G. Zhu. Estimating uncertainty: A bayesian approach to modelling photosynthesis in c3 leaves. *Plant, Cell & Environment*, 44(5):1436–1450, 2021.

[177] Y. Xiao, J. Sloan, C. Hepworth, M. Fradera-Soler, A. Mathers, R. Thorley, A. Baillie, H. Jones, T. Chang, X. Chen, et al. Defining the scope for altering rice leaf anatomy to improve photosynthesis: a modelling approach. *New Phytologist*, 237(2):441–453, 2023.

[178] D. Xiong. Leaf anatomy does not explain the large variability of mesophyll conductance across c3 crop species. *The Plant Journal*, 2023.

[179] D. Xiong, J. Flexas, T. Yu, S. Peng, and J. Huang. Leaf anatomy mediates coordination of leaf hydraulic conductance and mesophyll conductance to co 2 in oryza. *New Phytologist*, 213(2):572–583, 2017.

[180] J.T. Yang, A.L. Preiser, Z. Li, S.E. Weise, and T.D. Sharkey. Triose phosphate use limitation of photosynthesis: short-term and long-term effects. *Planta*, 243:687–698, 2016.

[181] M. Zamil and A. Geitmann. The middle lamella—more than a glue. *Physical Biology*, 14(1):015004, 2017.

[182] E. Zeiger, G.D. Farquhar, and I. Cowan. *Stomatal function*. Stanford University Press, 1987.

[183] X. Zheng, G. Shen, C. Wang, Y. Li, D. Dunphy, T. Hasan, C.J. Brinker, and B.L. Su. Bio-inspired murray materials for mass transfer and activity. *Nature Communications*, 8(1):14921, 2017.

[184] G. Zhu, X. Li, Y. Su, and C. Huang. Parameterization of a coupled co 2 and h 2 o gas exchange model at the leaf scale of populus euphratica. *Hydrology and Earth System Sciences*, 14(3):419–431, 2010.

[185] N. Zoulias, E.L. Harrison, S.A. Casson, and J.E. Gray. Molecular control of stomatal development. *Biochemical Journal*, 475(2):441–454, 2018.

[186] J. Zurzycki. The destructive effect of intense light on the photosynthetic apparatus [działanie destrukcyjne silnego światła na aparat fotosyntetyczny]. *Acta societatis botanicorum Poloniae*, 26(1):157–175, 1957.